Physics and Chemistry of Advanced Nanoscale Materials: Experiment, Simulation, and Theory

Thesis by
Ching-Hwa Kiang

In Partial Fulfillment of the Requirements
for the Degree of
Doctor of Philosophy

California Institute of Technology
Pasadena, California

1995

(Submitted March 9, 1995)

Acknowledgements

First, I would like to thank my advisor, William A. Goddard III, for his support and guidance. His interest in science and quest for an understanding of nature has been truly inspirational. The encouragement and support he provided was crucial to my development during graduate school.

I am grateful to Henry Weinberg for introducing me to the people at IBM research and to Daniel Auerbach for agreeing to support me in the Science and Technology Department. I would like to thank Heinrich Hunziker for his research support and for many helpful scientific discussions. I also want to express my appreciation to my thesis committee, who recommanded that the Caltech Chemistry Department allow me to carry out experimental work at IBM.

The many scientists at IBM Almaden Research Center have been of great help in my research on carbon. Donald Bethune, in particular, graciously allowed me to join his group and has been instrumental to my research on fullerenes and carbon nanotubes. Robby Beyers generously offerered very helpful guidance on electron microscopy. I also benefited from numerous discussions with Charlie Rettner, Jesse Salem, Ad Nazzal, Paul van Loosdrecht, Nino Yannoni, Bob Johnson, and Craig Hawker. I also thank Rich Rafey for graphics support and Darrell Dobbertin for

technical support on electron microscopy.

I enjoyed the friendly environment in the Goddard group. I appreciate the many scientific discussions with Naoki Karasawa, Changmoon Park, Xinlei Hua, Bao-Liang Tsai, and K.-T. Lim. Advice from Wen-Ching Wang and I-Jy Chang were also helpful. Several people I met during scientific meetings, Sumio Iijima, Millie Dresselhaus, Gene Dresselhaus, Bernard Seraphin, Morinobu Endo, Katsumi Tanigaki, and Thomas Ebbesen among others, have been very generous in providing advice and suggestions.

I benifited greatly from the scientific freedom offered by an IBM student fellowship and the continuing support by Heinrich Hunziker and Owen Melroy. The efficiency of Errol Smedley on dealing with issues between two institutions made it possible for me to do research without interruption. Mike Ross enthusiastically announced our discoveries to media ranging from scientific news to The New York Times, making research more exciting.

Special thanks go to Father Downey, for persistently encouraging me to do my best and to get my Ph.D. Karate practice has helped me in learning to overcome difficulties. I appreciate the dedication of the instructors in the LA and the Bay Area, particularly the encouragement from Tsutomu Ohshima. The support from my mother and my sisters has been important. Finally, I want to thank Mike Deem, who has been patient and supportive throughout my graduate studies.

Abstract

Physics and Chemistry of Advanced Nanoscale Materials:
Experiment, Simulation, and Theory
by
Ching-Hwa Kiang
Doctor of Philosophy in Chemistry
California Institute of Technology
Professor William A. Goddard, III

This thesis discusses simulation and theory of lattice dynamics as well as experiments on novel forms of carbon.

A new crystalline AgBr interaction potential was constructed by fitting literature experimental data. The shell model was successfully used to account for the polarizabilities of the ions. This approach overcame difficulties previous investigators faced in determining the AgBr potential.

The very useful shell model was generalized to allow, for the first time, its use in dynamical simulations. The rapid shell dynamics, simulating the electron polarization, were integrated out in a generalized Born-Oppenheimer-like approach. The effective Hamiltonians were derived for both quantum and classical descriptions of the shells.

The first crystallization and characterization of a metallofullerene were performed. Endohedral metallofullerenes were synthesized and characterized. Metals such as Sc,

Y, and Er that formed stable compounds in fullerene cages were synthesized and products purified. The crystal structure of Sc_2C_{84} was determined by transmission electron microscopy study.

Experimental studies on fullerenes and related materials lead to the first example of a catalytically-grown, fullerene-like material. We discovered that single-layer carbon nanotubes can be produced by vaporizing cobalt and carbon with an electric arc in a helium atmosphere. Catalyst promoters such as sulfur, bismuth, and lead were found not only to enhance the yield of single-layer nanotubes but also to produce tubes in a diameter range not accessible with cobalt alone. Sulfur, bismuth, and tungsten were found to catalyze the formation of cobalt crystals encapsulated in graphitic polyhedra. Various carbon structures were also produced concurrently, *e.g.* multilayer nanotubes, strings of carbon nanocompartments, carbon nanofibers, and metal-filled nanomaterials. Nanotubes were observed to undergo real-time structural changes under electron beam heating.

A growth model of single-layer nanotube was formulated based on the experimental results. The carbon ring is regarded as the nanotube precursor, and cobalt carbide is regarded as the catalytic species that efficiently supplies carbon clusters to the open end of tube. The catalyst promoter assists the reaction by keeping the growing end open.

Contents

List of Figures

List of Tables

Chapter 1

Background and Motivation

In this thesis we discuss simulation and theory of lattice dynamics as well as experiments on novel forms of carbon. This introductory chapter provides background and motivation for the studies described in later chapters.

1.1 Theoretical Studies of Lattice Dynamics

1.1.1 Polarization Effects in the AgBr Interaction Potential

Interest in the photographic processes and ionic transport properties in silver halides has prompted much speculation about the crystal dynamics of these systems [1], and the anomalous physical properties of AgBr and AgCl have been investigated extensively. Unlike the theoretical calculations of the lattice vibrations of alkali halides, which often agree with experimental neutron scattering data [2, 3], calculations on silver bromide crystals of the rock salt crystal structure suggest that they possess several physical properties that are unusual for a normal ionic crystal [4, 5, 6]. Indeed, fitting of force fields to experimental data such as dielectric constant, phonon dispersion frequencies, elastic constants, and cohesive energy density, has often lead

to unphysical parameters [3, 7, 8]. The development of an adequate force field that can successfully represent the crystal potential is essential if simulations are to lead to an understanding of the peculiar properties of silver halides.

In Chapter 2 we discuss a new interaction potential that is simple enough to be efficiently included in classical atomic simulations. The crystalline AgBr interaction potential was constructed by fitting literature experimental data, such as the lattice constant, phonon frequencies at Γ and X points, dielectric constant, cohesive energy, and elastic constants, to a pairwise additive form. The properties predicted by this potential results compare favorably with experimentally measured values. A modified shell model was incorporated to account for the polarizabilities of the ions. The influence of polarization effects on the various physical properties of the crystal is discussed.

1.1.2 A Dynamical Shell Model

In molecular mechanics and molecular dynamics simulations, one usually finds it necessary to modify the rigid-ion model to take into account the polarizability [2, 9, 10]. One particularly successful model of atomic polarizability is the shell model, used in Chapter 2 and used extensively in the past to simulate the weak bonding of the outermost electrons to the core [2, 9, 10]. Such a model is adequate for calculation of various static crystal properties and, in the harmonic approximation for the motion of both shells and cores, for calculation of the phonon dispersion curves. Such a shell model has been difficult to incorporate directly into a classical molecular dynamics simulation due to the very high frequency of the shell motion. Furthermore, no attempt to quantize the shell motion and, thus, to incorporate the quantum effects of the shell motion in a molecular dynamics simulation seems to have been undertaken.

In Chapter 3 we discuss an analytic treatment of the shell model that renders it

suitable for Monte Carlo and molecular dynamics simulations at any temperature.[1] Our first observation is that the cores are much more massive than the shells and thus, can be considered fixed during shell vibrations. The shells can then be expected to equilibrate to the cores according to statistical mechanical theory. We found the effective core Hamiltonian by "integrating out" the shell fluctuations with the help of classical or quantum statistical mechanical theory. This approach may be described as a statistical Born-Oppenheimer approximation. The effective Hamiltonian has two components. The first represents the energy due to the shells adopting the minimum energy position for any given core configuration. The second accounts for fluctuations, zero-point as well as excited-state motion in the quantum case and thermal fluctuations in the classical case. The fluctuations of the shell positions account for the London dispersion interaction. The resulting equations likely have applications to other systems containing motions with disparate time scales.

1.2 Novel Forms of Carbon

Carbon possesses an exceptional ability to form diverse stable structures in the vapor phase. In an inert atmosphere it self-assembles to form hollow spheroidal fullerenes [11]. These molecules can be produced in bulk, and many are chemically stable [12, 13]. As the carbon vapor self-assembles to form fullerenes in the gas phase, the carbon deposited on the hot cathode tip builds fine graphitic tubules and polyhedral particles with nanometer dimensions [14, 15, 16, 17]. Electron beam heating of these nanotubes and nanoparticles transforms them into nearly spherical nested particles [18]. Figure 1.1 depicts examples of interesting carbon structures.

New species form when reactive elements are added to the carbon vapor. Va-

[1] C.-H. Kiang and W. A. Goddard III, J. Chem. Phys. **98**, 1451 (1993).

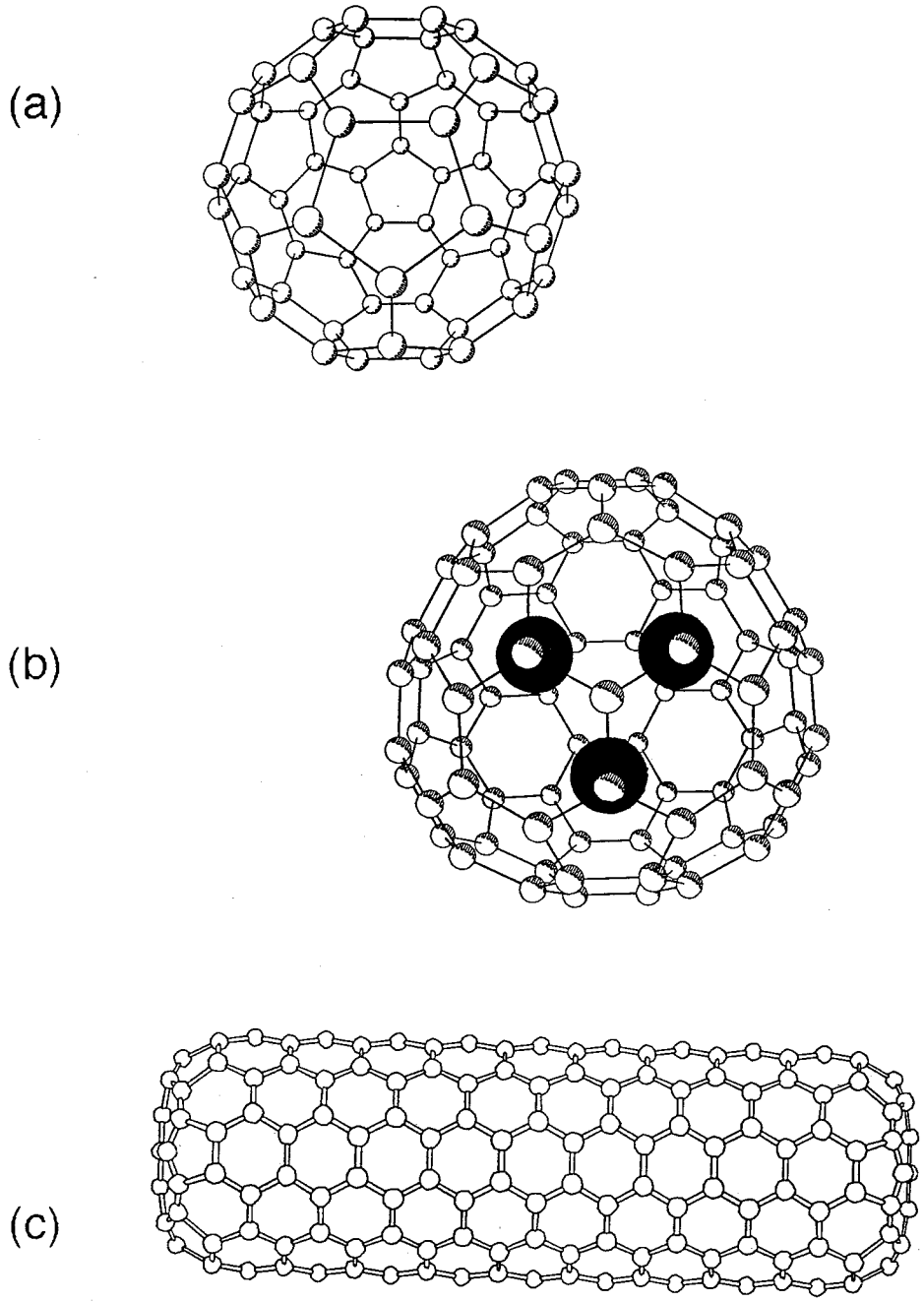

Figure 1.1: Various carbon structures formed by self-assembly: (a) Fullerene C_{60}, (b) Endohedral Metallofullerene $Sc_3@C_{82}$, and (c) carbon nanotube with an armchair structure (from Ref. [19]).

porizing metals with carbon can produce endohedral metallofullerenes in the gas phase [20, 21, 22, 23, 24], and metal carbide nanocrystals encased in multilayer graphitic polyhedra form in the material that deposits on the cathode [25, 26]. Carbon fibers grown in the vapor phase exhibit superior mechanical and electrical properties [27, 28, 29]. Graphite whisker-like filaments, 1 to 5 micrometers in diameter and several centimeters in length, form in an arc run in high pressure of argon [30]. Hydrocarbon decomposition on transition metal catalysts, on the other hand, produces large quantities of carbon fibers at temperatures between 500 ° C and 1200 ° C [27, 28, 29].

1.2.1 Metallofullerenes

The term *fullerene* was established to denote a molecule that is composed of only sp^2 bonded carbons that form a cage-like structure. The prediction that atoms can be trapped inside the cage was initially demonstrated by laser vaporization of graphite target with a lanthanum salt [20]. A notation X@C_n was introduced to denote the species X located inside the C_n cage [21]. This carbon cage provides a new class of host where an individual atom, ion, or cluster can be isolated on a molecular scale. Metals trapped inside spherical carbon cages (*e.g.* C_{76}, C_{82}, and C_{84}) to form stable molecules called endohedral metallofullerene have recently been synthesized [24, 31, 32].

Spectroscopic characterization and theoretical calculations have shed light on the geometric and electronic structure of metallofullerenes [33, 34, 35]. Indirect data such as EPR electronic property studies and STM images suggest that the metals are inside [32, 34]. Direct proof from structural characterizations based on crystallographic data are now feasible due to the recent advances in separation and purification techniques

In Chapter 4 we discuss the synthesis, purification, and characterization of several

metallofullerenes. The metals Sc, Y, and Er were encapsulated in carbon cages to form stable endohedral metallofullerenes. These species were successfully purified by HPLC.[2] The Sc species was crystallized and characterized by using high-resolution TEM imaging and electron diffraction.[3] This is the first example of a metallofullerene structure determination.

1.2.2 Carbon Nanotubes and Nanoparticles

The term *carbon nanotube* generally refers to carbon with a cylindrical graphene structure. Multilayer carbon nanotubes are typically produced on the cathode tip in an electric arc. These nanotubes are composed of 2 to 50 layers of cylindrical shells, with tube diameters ranging from 1 to 50 nm. Each layer has the structure of a rolled up graphene sheet, with the sp^2 carbons forming a honeycomb structure.

Theoretical studies of nanotubes have predicted that they have unusual mechanical, electrical, and magnetic properties of fundamental scientific and possibly technological interest [19, 36]. Potential applications for such one-dimensional conductors [36], super-strong crystals [37], and sorption materials for gases such as hydrogen [38] have been suggested. These predictions are, however, based on single-layer carbon nanotubes as model systems.

Single-layer carbon nanotubes can be produced with or without a catalyst. Carbon can self-assemble into tubes without a catalyst by either hydrocarbon decomposition [39] or carbon vapor condensation on a substrate surface [40]. The yield is low and the nanotubes produced usually have more than one layer. Methods to synthesize

[2]S. Stevenson, H. C. Dorn, P. Burbank, K. Harich, J. Haynes, C.-H. Kiang, J. R. Salem, M. S. de Vries, P. H. M. van Loosdrecht, R. D. Johnson, C. S. Yannoni, and D. S. Bethune, Anal. Chem. **66**, 2675 (1994); S. Stevenson, H. C. Dorn, P. Burbank, K. Harich, Z. Sun, C.-H. Kiang, J. R. Salem, M. S. de Vries, P. H. M. van Loosdrecht, R. D. Johnson, C. S. Yannoni, and D. S. Bethune, Anal. Chem. **66**, 2680 (1994).

[3]R. Beyers, C.-H. Kiang, R. D. Johnson, J. R. Salem, M. S. de Vries, C. S. Yannoni, D. S. Bethune, H. C. Dorn, P. Burbank, K. Harich, and S. Stevenson, *Nature* **370**, 196 (1994).

single-layer nanotubes were first discovered in 1993, when Iijima's group and our group independently found ways to produce them in macroscopic quantities [41, 42]. These methods both involved co-vaporizing carbon with a transition metal catalyst. Iijima's group produced single-layer nanotubes by vaporizing graphite and Fe in an Ar/CH_4 atmosphere [41], and our group vaporized Co and graphite under helium buffer gas [42]. Subsequently Ni was found to have similar catalytic property [43, 44].

Catalytic synthesis of carbon nanotubes produces nanotubes with exclusively single layers and in high yields. The nanotubes produced have a very high aspect ratio (length to diameter ratio), and they are 1 to 2 nanometers in diameter and micrometers in length. Figure 1.2 is a transmission electron micrograph of the single-layer carbon nanotubes produced by Co catalyst [45], and Fig. 1.3 depicts the detailed atomic arrangement of nanotubes.

Metals such as Gd and Y have also been shown to catalyze nanotube growth [46, 47]. These tubes, however, are rooted on a metal carbide (or metal oxide) crystal, and have diameters ranging from 1 to 2 nm and lengths from 10 to 200 nm. We focus on the single-layer carbon nanotubes produced using Co catalyst, and the effects of certain catalyst promoters on the nanotube growth.

In Chapter 5 we describe the catalytic synthesis of single-layer carbon nanotubes.[4] We discuss the finding that, when used with cobalt in an electric arc, sulfur, bismuth, and lead increase the yield of nanotubes, forming tubes with diameters lying outside the range produced with cobalt alone.[5] Sulfur, bismuth, and tungsten also catalyze the formation of cobalt encapsulated graphitic polyhedra.[6] The results suggest that

[4]D. S. Bethune, C.-H. Kiang, M. S. de Vries, G. Gorman, R. Savoy, J. Vazquez, and R. Beyers, Nature **363**, 605 (1993).

[5]C.-H. Kiang, W. A. Goddard III, R. Beyers, J. R. Salem, and D. S. Bethune, J. Phys. Chem. **98**, 6612 (1994); C.-H. Kiang, P. H. M. van Loosdrecht, R. Beyers, J. R. Salem, D. S. Bethune, W. A. Goddard III, H. C. Dorn, P. Burbank, and S. Stevenson, to appear in Surf. Rev. Lett.

[6]C.-H. Kiang, W. A. Goddard III, R. Beyers, J. R. Salem, and D. S. Bethune, to appear in Carbon; C.-H. Kiang, W. A. Goddard III, R. Beyers, J. R. Salem, and D. S. Bethune, to appear in

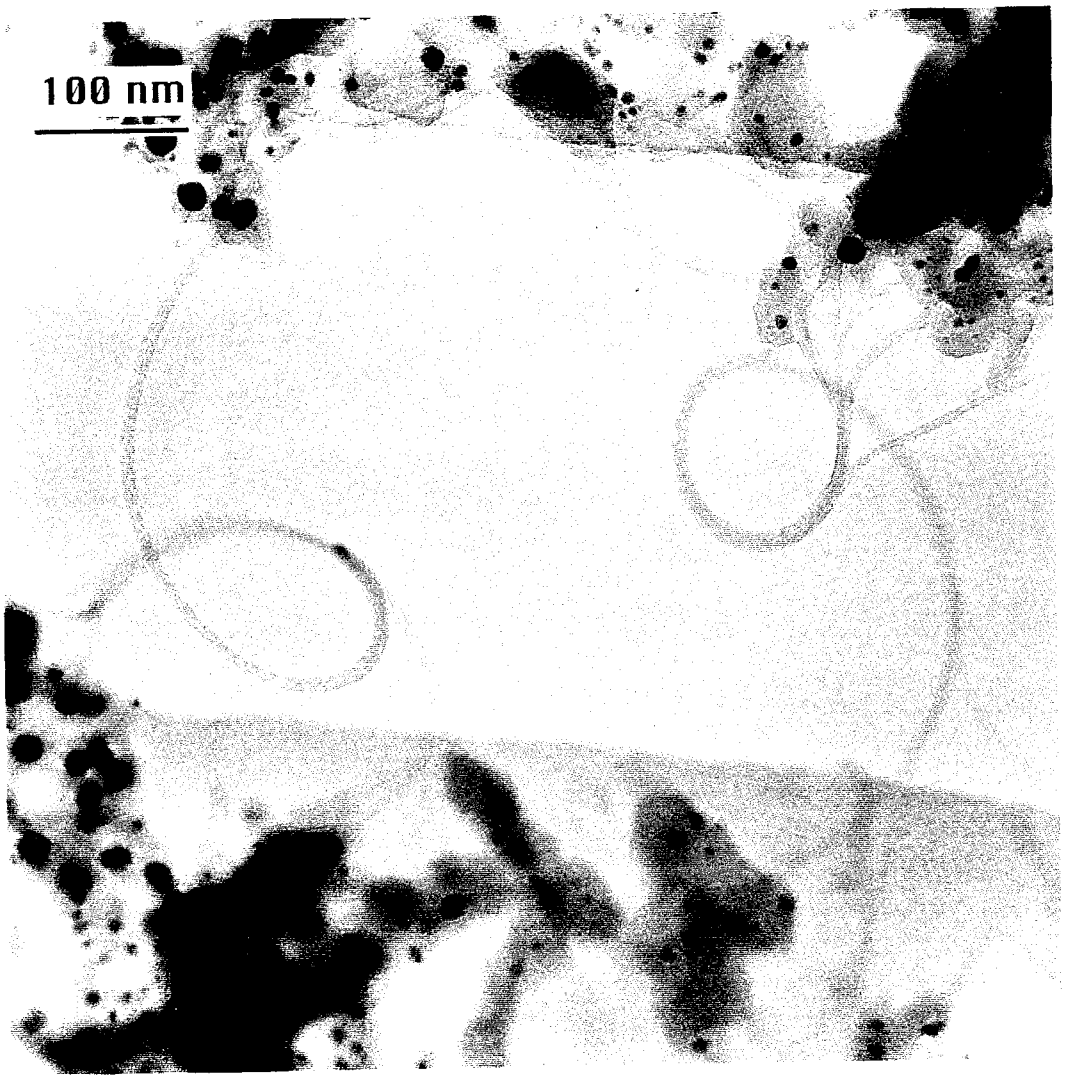

Figure 1.2: Transmission electron micrograph of single-layer carbon nanotubes produced by cobalt catalyst.

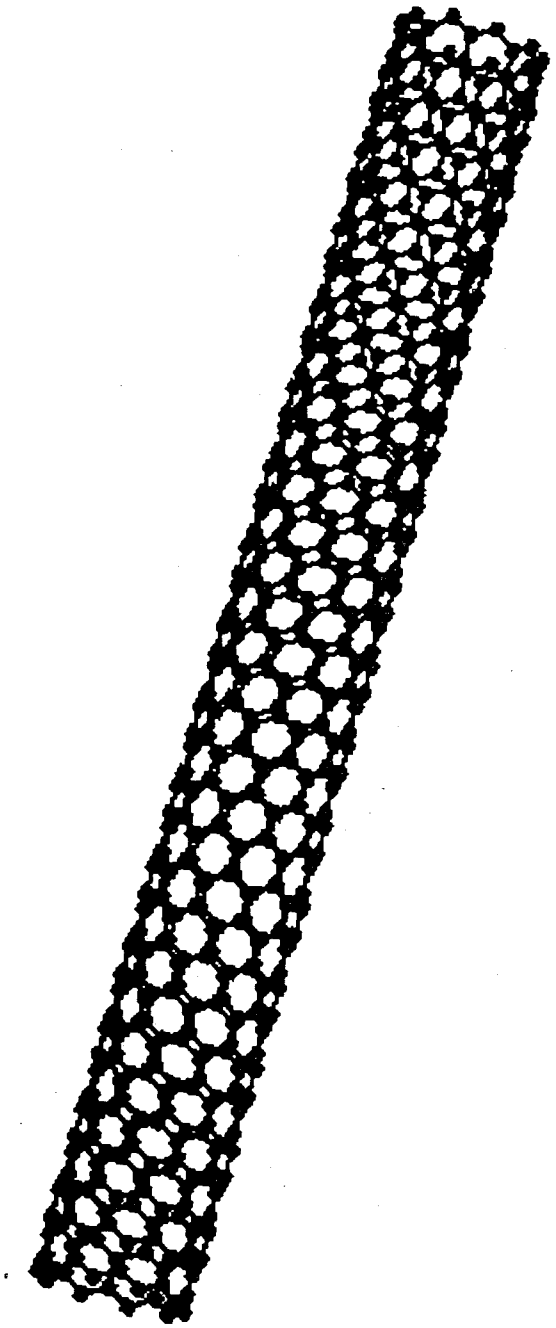

Figure 1.3: Molecular model of carbon nanotubes. The honeycomb structure of nanotubes was confirmed by transmission electron microscopy studies.

the single-layer carbon nanotubes do not nucleate from the cobalt crystals, in contrast to the classical growth model of vapor phase grown carbon fibers.

In Chapter 6 we discuss the many structures that occur under the reaction conditions described in Chapter 5. Various deformations to perfect nanotubes are detailed. Destruction and reconstruction reactions due to electron beam heating are discussed. A variety of carbonaceous nanotubule structures are exhibited. The metal particles produced in this process are also discussed in some detail.

Study of the growth mechanism is essential for further synthetic progress as well as for gaining an understanding of the gas-phase self-assembly of this novel carbon molecule. In Chapter 7 we propose a growth model for single-layer carbon nanotubes. Single-layer carbon nanotubes grown by the Co catalyst have unique features that are distinct from those of the vapor grown carbon fibers and the multilayer nanotubes formed on the cathode tip. For example, they are almost exclusively single-layered and often have a structured diameter distribution. These observations strongly suggest that a distinct growth mechanism is responsible for the single-layer nanotube growth. Our model was formulated based on the experimental results. The nanotubes build from a carbon ring, with the cobalt carbide catalytic species efficiently supplying carbons to the open end of tube. The catalyst promoter assists the reaction by stabilizing the carbon dangling bonds at the open end to prevent it from forming pentagons that would terminate the tube growth.

Science and Technology of Fullerene Materials, MRS Proc., edited by P. Bernier, T. W. Ebbesen, D. S. Bethune, R. M. Metzger, L. Y. Chiang, and J. W. Mintmire, (Materials Research Society, Pittsburgh, 1994).

References

[1] For a review, see J. F. Hamilton, Adv. Phys. **37**, 359 (1988).

[2] A. D. B. Woods, W. Cochran, and B. N. Brockhouse, Phys. Rev. **119**, 980 (1960).

[3] R. A. Cowley, W. Cochran, B. N. Brockhouse, and A. D. B. Woods, Phys. Rev. **131**, 1030 (1963).

[4] W. von der Osten, *The Physics of Latent Image Formation in Silver Halides*, International Symposium, Trieste, edited by A. Baldereschi, W. Czaja, E. Tosatti, and M. Tosi., (World Scientific, Singapore, 1983), p. 1.

[5] W. Bührer, Phys. Stat. Sol. (b) **68**, 739 (1975).

[6] R. J. Friauf, J. Phys. (Paris) **20**, 705 (1987).

[7] Y. Fujii, S. Hoshino, S. Sakuragi, and H. Kanzaki, Phys. Rev. B **15**, 358 (1977).

[8] P. R. Vijayaraghavan, R. M. Nicklow, H. G. Smith, and M. K. Wilkinson, Phys. Rev. B **1**, 4819 (1970).

[9] B. G. Dick, Jr. and A. W. Overhauser, Phys. Rev. **112**, 90 (1958).

[10] W. Cochran, R. A. Cowley, G. Dolling, and M. M. Elcombe, Proc. Roy. Soc. (London) **293A**, 433 (1966).

[11] H. W. Kroto, J. R. Heath, S. C. O'Brien, R. F. Curl, and R. E. Smalley, Nature **318**, 162 (1985).

[12] W. Krätschmer, K. Fostiropoulos, and D. R. Huffman, Chem. Phys. Lett. **170**, 167 (1990).

[13] W. Krätschmer, L. D. Lamb, K. Fostiropoulos, and D. R. Huffman, Nature **347**, 354 (1990).

[14] S. Iijima, Nature **354**, 56 (1991).

[15] S. Iijima, T. Ichihashi, and Y. Ando, Nature **356**, 776 (1992).

[16] T. W. Ebbesen and P. M. Ajayan, Nature **358**, 220 (1992).

[17] Y . Saito, T. Yoshikawa, M. Inagaki, M. Tomita, and T. Hayashi, Chem. Phys. Lett. **204**, 277 (1993).

[18] D. Ugarte, Nature **359**, 707 (1992).

[19] R. Saito, M. Fujita, G. Dresselhaus and M. S. Dresselhaus, Mater. Sci. Eng. **B 19**, 185 (1993).

[20] J. R. Heath, S. C. O'Brien, Q. Zhang, Y. Liu, R. F. Curl, H. W. Kroto, Q. Zhang, F. K. Tittel, and R. E. Smalley, J. Am. Chem. Soc. **107**, 7779 (1985).

[21] Y. Chai, T. Guo, C. Jin, R.E. Haufler, L.P.F. Chibante, J. Fure, L. Wang, J.M. Alford, and R.E. Smalley, J. Phys. Chem. **95**, 7564 (1991).

[22] R. D. Johnson, M. S. de Vries, J. R. Salem, D. S. Bethune, and C. S. Yannoni, Nature **355**, 239 (1992).

[23] C. S. Yannoni, M. Hoinkis, M. S. de Vries, D. S. Bethune, J. R. Salem, M. S. Crowder, and R. D. Johnson, Science **256**, 1191 (1992).

[24] H. Shinohara, H. Sato, M. Ohkohchi, Y. Ando, T. Kodama, T. Shida, T. Kato, and Y. Saito, Nature **357**, 52 (1992).

[25] R.S. Ruoff, D.C. Lorents, B. Chan, R. Malhotra, and S. Subramoney, Science **259**, 346 (1993).

[26] Y. Saito, T. Yoshikawa, M. Okuda, M. Ohkohchi, M. Inagaki, Y. Ando, A. Kasuya, and Y. Nishina, Chem. Phys. Lett. **209**, 72 (1993).

[27] G. G. Tibbetts, J. Cryst. Growth **73**, 431 (1985).

[28] M. Endo, Chemtech **18**, 568 (1988).

[29] R. T. K. Baker, Carbon **27**, 315 (1989).

[30] R. Bacon, J. Appl. Phys. **31**, 283 (1960).

[31] S. Suzuki, S. Kawata, H. Shiromaru, K. Yamauchi, K. Kikuchi, T. Kato, and Y. Achiba, J. Phys. Chem. **96**, 7159 (1992).

[32] C. S. Yannoni, M. Hoinkis, M. S. de Vries, D. S. Bethune, J. R. Salem, M. S. Crowder, and R. D. Johnson, Science **256**, 1191 (1992).

[33] H. Shinohara, H. Yamaguchi, N. Hayashi, H. Sato, M. Ohkohchi, Y. Ando, and Y. Saito, J. Phys. Chem. **97**, 4259 (1993).

[34] X.-D. Wang, Q. K. Xue, T. Hashizume, H. Shinohara, Y. Nishina, and T. Sakurai, Phys. Rev. **B 48**, 15492 (1993).

[35] K. Laasonen, W Andreoni, and M. Parrinello, Science **258**, 1916 (1992).

[36] N. Hamada, S.-I. Sawada and A. Oshiyama, Phys. Rev. Lett. **68**, 1579 (1992).

[37] J. Tersoff and R. S. Ruoff, Phys. Rev. Lett. **73**, 676 (1994).

[38] T. A. Bekkedahl and M. J. Hebben (private communication).

[39] M. Endo, K. Takeuchi, S. Igarashi, K. Kobori, M. Shiraishi, and H. W. Kroto, J. Phys. Chem. Solids **54**, 1841 (1993).

[40] M. Ge and K. Sattler, Science **260**, 515 (1993).

[41] S. Iijima and T. Ichihashi, Nature **363**, 603–605 (1993).

[42] D. S. Bethune, C.-H. Kiang, M. S. de Vries, G. Gorman, R. Savoy, J. Vazquez, and R. Beyers, Nature **363**, 605 (1993).

[43] Y. Saito, T. Yoshikawa, M. Okuda, N. Fujimoto, K. Sumiyama, K. Suzuki, A. Kasuya, and Y. Nishina, J. Phys. Chem. Solids **54**, 1849 (1993).

[44] S. Seraphin and D. Zhou, Appl. Phys. Lett. **64**, 2087 (1994).

[45] For a review, see C.-H. Kiang, W. A. Goddard III, R. Beyers, J. R. Salem, and D. S. Bethune, to appear in Carbon.

[46] S. Subramoney, R. S. Ruoff, D. C. Lorents, and R. Malhotra, Nature **366**, 637 (1994).

[47] S. Seraphin, in *Recent Advances in the Chemistry and Physics of Fullerenes and Related Materials*, edited by K. M. Kadish and R. S. Ruoff (The Electrochemical Society, Pennington, NJ, 1994).

Chapter 2

Polarization Effects in the AgBr Interaction Potential

2.1 Introduction

Silver halides have long been a subject of study from both a theoretical and a practical point of view [1]. In particular, interest in the photographic processes and ionic transport properties in silver halides has prompted much speculation about the crystal dynamics of these systems, and the anomalous physical properties of AgBr and AgCl have been investigated extensively. The unusual electron energy band [2], peculiar lattice dynamics [3, 4], and exceptionally high mobility of the interstitial silver ions [5, 6] make these crystalline systems distinct from other isostructural alkali halides [7]. Practical theoretical work on AgBr and AgCl requires construction of an interionic potential model that can describe the uncommon behavior of silver halides. The development of an adequate force field that can successfully represent the crystal potentials is essential if simulations are to lead to an understanding of the peculiar properties of silver halides [8].

The first interaction potentials of silver halides were proposed by Mayer [9]. This potential characterizes the system with strong short-range repulsion and van der Waals attractions. There have been recent attempts at constructing the interaction potentials of silver halides as well [10, 11]. The potentials have been formed from pairwise interactions, such as electrostatic, van der Waals attractions, and short-range repulsions as well as some 3-body terms. The undetermined coefficients in the potentials were fit so as to reproduce experimentally measured properties, *e.g.* lattice constant, cohesive energy, phonon dispersion curves, dielectric constants, and elastic constants. While some of the calculated properties (such as the elastic constant, dielectric constant, and cohesive energy) from the potentials agree with some of the experimental results, the agreement between the experimentally observed and the theoretically calculated phonon dispersion curves is still not satisfying.

Since an adequate potential for AgBr is essential for simulating the static as well as dynamic crystal properties, we present here a new interaction potential that is simple enough for classical atomic simulations. We investigated polarization effects via the shell model, which has previously been applied to the simulations of the lattice dynamics of silver halides with great success [3, 12]. It accounts for many of the various properties that have been observed experimentally, such as the dielectric constant and phonon dispersion curves.

2.2 Method

We constrain the potential to be pairwise, with a long-range Coulomb potential, a short-range interaction potential, and an energy due to the polarization of the particles in the crystal.

$$U = U_{\text{Coulomb}} + U_{\text{short-range}} + U_{\text{spring}} \,. \tag{2.1}$$

Periodic boundary conditions are assumed in this formulation. The long-range Coulomb interaction between two ions is

$$U_{\text{Coulomb}} = \sum_{i,j}{}' \frac{q_i q_j}{R_{ij}} \ , \tag{2.2}$$

where q_i, q_j are charges of the ions, cores, and shells, and R_{ij} is the distance between positions i and j. The electrostatic interaction between a core and shell connected by a spring is excluded when using the shell model. The prime indicates exclusion of the $i = j$ term and the core-shell terms. The Coulomb potential is the dominant interaction in ionic crystals. The short-range potential function contains an attractive term of the London dispersion type as well as a repulsive term due to the Pauli exclusion principle. We adopt either the two-parameter Lennard-Jones potential [13]

$$U_{\text{LJ}} = D_0 \left\{ \left(\frac{R_0}{R} \right)^{12} - 2 \left(\frac{R_0}{R} \right)^{6} \right\} \tag{2.3}$$

or the three-parameter exponential-6 function

$$U_{\text{exp-6}} = D_0 \left\{ \left[\left(\frac{6}{\gamma - 6} \right) e^{\gamma \left(1 - \frac{R}{R_0} \right)} \right] - \left[\left(\frac{\gamma}{\gamma - 6} \right) \left(\frac{R_0}{R} \right)^{6} \right] \right\} \ . \tag{2.4}$$

The last term in Eq. (2.1), U_{spring}, is the sum of spring energies introduced by the shell model [14]

$$U_{\text{spring}} = \frac{1}{2} \sum_i k_i \delta r_i^2 \ , \tag{2.5}$$

where δr_i represents the shell displacement from the core. The shell model is included to account for the polarizabilities of Ag^+ and Br^- ions. In this simple approximation, the polarizable valence electrons are represented by a spherical shell connected to the core via a harmonic spring. The shell charge Y and the spring constant k are

adjustable parameters, and they are related to the polarizability by the relation

$$\alpha_i = \frac{Y_i^2}{k_i} \ , \tag{2.6}$$

where α_i is the atomic polarizability, $i = Ag^+$, Br^-. The shells are charged, and this electrostatic energy is included in the Coulomb sum, Eq. (2.2). The β value (the ratio of the shell velocity v to the speed of light c) associated with this model is less than 0.01, so that relativistic effects can be ignored, with only the electrostatic energy included.

The convergence with distance of the sum of Eq. (2.1), especially the conditionally convergent Coulomb term, requires special attention. We defined $\mathbf{r}_i$ as a position in a unit cell and $\mathbf{l}$ as the origin of that particular unit cell. The position of atom i is, therefore, $\mathbf{r}_i + \mathbf{l}$. The Coulomb potential and the London dispersion energy were evaluated with the Ewald method [15]. The Coulomb sum is

$$\begin{aligned} S_{\text{Coulomb}} &= \frac{1}{2} \lim_{L\to\infty} {\sum_{i,j,\mathbf{l}}}' \frac{q_i q_j}{r_{i,j,\mathbf{l}}} \\ &= \frac{1}{2} {\sum_{i,j,\mathbf{l}}}' q_i q_j \frac{\operatorname{erfc}(\pi^{1/2} K r_{i,j,\mathbf{l}})}{r_{i,j,\mathbf{l}}} + \frac{1}{2\pi\Omega} \sum_{\mathbf{h}\neq\mathbf{0}} |F(\mathrm{h})|^2 \frac{e^{-\pi h^2/K^2}}{h^2} - K \sum_i q_i^2 \\ &\quad + \frac{1}{2\Omega} \int_{\partial V(L)} \frac{\mathbf{d}\cdot\mathbf{r}\ \mathbf{d}\cdot\mathbf{n}}{r^3} dS \end{aligned} \tag{2.7}$$

where $\mathbf{h}$ is the reciprocal lattice vector, Ω is the unit cell volume, and $r_{i,j,\mathbf{l}} = |\mathbf{r}_i - (\mathbf{r}_j + \mathbf{l})|$, and the other symbols are defined in Ref. [16]. The last term in Eq. (2.7) is ignored because it is nonzero only for non-centrosymmetric crystal structures and represents a surface charge [17]. The unit cells are charge neutral in our case. The London dispersion energy sum is [17]

$$S_{\text{London}} = \frac{1}{2} {\sum_{i,j,\mathbf{l}}}' \frac{C_{ij}}{r_{i,j,\mathbf{l}}^6}$$

$$
\begin{aligned}
= & \frac{1}{2}\sum_{i,j,\mathbf{l}}{}' \frac{q_i q_j}{r_{i,j,\mathbf{l}}^6}\left(1+a^2+a^4/2\right)e^{-a^2} \\
& + \frac{\pi^{9/2}}{3\Omega}\sum_{\mathbf{h}\neq\mathbf{0}} |F(\mathbf{h})|^2 h^3 \left[\pi^{1/2}\mathrm{erfc}(b) + \left(\frac{1}{2b^3}-\frac{1}{b}\right)e^{-b^2}\right] \\
& + \frac{\pi^3 K^3}{6\Omega}\left(\sum_i q_i\right)^2 - \frac{1}{12}\pi^3 K^6 \left(\sum_i q_i^2\right)^2 , \qquad (2.8)
\end{aligned}
$$

where new symbols are defined in Ref. [15] The short-range repulsion are summed over all interactions within 8Å. This ensures accuracy to within 0.01 kcal/mol.

We now proceed by systematic investigation to decouple the different parameters that are involved in the potentials. First, a potential with just van der Waals attractions plus short-range repulsions due to Pauli repulsion, *i.e.* a exp-6 function or a Lennard-Jones potential, is examined. Then shells are added to the Br^- ions to take into account the Br^- ion polarizability, since it is greater than that of Ag^+ polarizability. And finally shells are included with the Ag^+ ions to model the crystal dielectric constant with greater accuracy. The potential is constructed by summing over all the interactions described above. For each model, parameters are fit to experimental data available at approximately 0K (*i.e.* lattice constant [18], phonon frequencies at Γ and X points of the Brillouin zone [19], dielectric constant [20], lattice energy [21], and elastic constants [19]). Defining the Hessian (second derivative) matrix D

$$
D_{ia,jb} = \frac{\partial^2 U}{\partial \mathbf{r}_{ia}\partial \mathbf{r}_{jb}} , \qquad (2.9)
$$

where r_{ia} is the a component (a, b = x,y, or z) of the ith center. The phonon modes are evaluated by assigning the shells small but finite masses then diagonalizing the Hessian. The static dielectric tensor is calculated by [22, 23]

$$
\epsilon_{0_{ab}} = \delta_{ab} + \frac{4\pi}{\Omega}\sum_{i,j} q_i q_j D^{-1}_{ia,jb} . \qquad (2.10)
$$

The high frequency dielectric constants were calculated by the Lyddane-Sachs-Teller relation [14]

$$\omega_L^2 = \frac{\epsilon_0}{\epsilon_\infty}\omega_T^2 \ , \tag{2.11}$$

where ω_L and ω_T are the longitudinal and transverse optical-mode frequencies, and ϵ_∞ and ϵ_0 are the high-frequency dielectric constant and the static dielectric constant. Note that only shell vibrations contribute to the high frequency dielectric constant ϵ_∞. Also note that literature data obey this relation only to within 10%, perhaps due to experimental uncertainty of the phonon frequencies.

We examined different shell charges and ionic charges. The absolute ionic charge determines the major part of the cohesive energy. The phonon curves can be fit by adjusting other parameters, such as shell charges and spring constants. We found that, setting the ionic charge to $q = 1$ predicts the lattice energy reasonably well. Hence we fixed the ionic charge at $q = 1$ so that the calculated lattice energy can be fit to the experimental cohesive energy. To reduce the number of parameters in the fitting procedures, we postulated different shell charges and then optimized the spring constants and short-range interactions. The best result has been found at $Y_{Br^-} = -4.0$ for models with only the Br^- ion polarizable and $Y_{Ag^+} = -8.0$ and $Y_{Br^-} = -5.0$ for models with both ions polarizable. We, therefore, set the shell charges at these values and vary only the spring constants and short-range interaction parameters when exploring different models.

The shell masses were treated as parameters. We found that the effects of different shell masses (within the order of an electron mass) on the various properties simulated to be negligible. Therefore we set the shell mass to 0.001 amu in the simulation.

2.3 Results

Figures 2.1 to 2.6 illustrate the fits of different models to the wave-vector-dependent phonon dispersion curves obtained by neutron scattering at 4.4 K [19].

The parameters determined for the various models are tabulated in Table 2.1. Table 2.2 lists the properties calculated from the various models. For the nonbonding potential functions, we used either Lonnard-Jones or exp-6 potentials on both the one-shell model and the two-shell model. The exp-6 term was found more appropriate than the Lennard-Jones potential in this system. We could not find a suitable force field using Lennard-Jones potentials, which agrees with the common wisdom that the Lennard-Jones potential is preferable for liquids whereas exp-6 is preferable for solids. An examination of the exp-6 potential reveals that the equilibrium distance R_0 between Ag^+ and Br^- is about 4.2Å, whereas the Ag^+-Br^- distance in AgBr crystal is around 3Å. That is, the ions are in the repulsive part of the potential. Quantum mechanical calculations have suggested that the repulsive potential is not the inverse-power function, as in the Lennard-Jones potential. It is, to a finer approximation, an exponential function of the distance R. Hence the exp-6 potential is generally expected to have a superior representation of the repulsive part than will the Lennard-Jones potential, and our results are consistent with this expectation. The fits with the Lennard-Jones potential are of low quality, and these results are not shown. We therefore proceed with exp-6 potential in all different models, and the parameters are optimized independently by fitting with the available experimental data by singular value decomposition method.

Model I is a rigid ion model. The potential contains only Coulomb and exp-6 interactions, with the ionic polarizabilities ignored. As noted in previous studies of AgCl [24] and AgBr [3], good agreement between computed and experimentally observed properties can not be achieved without including the polarization effect. Figure

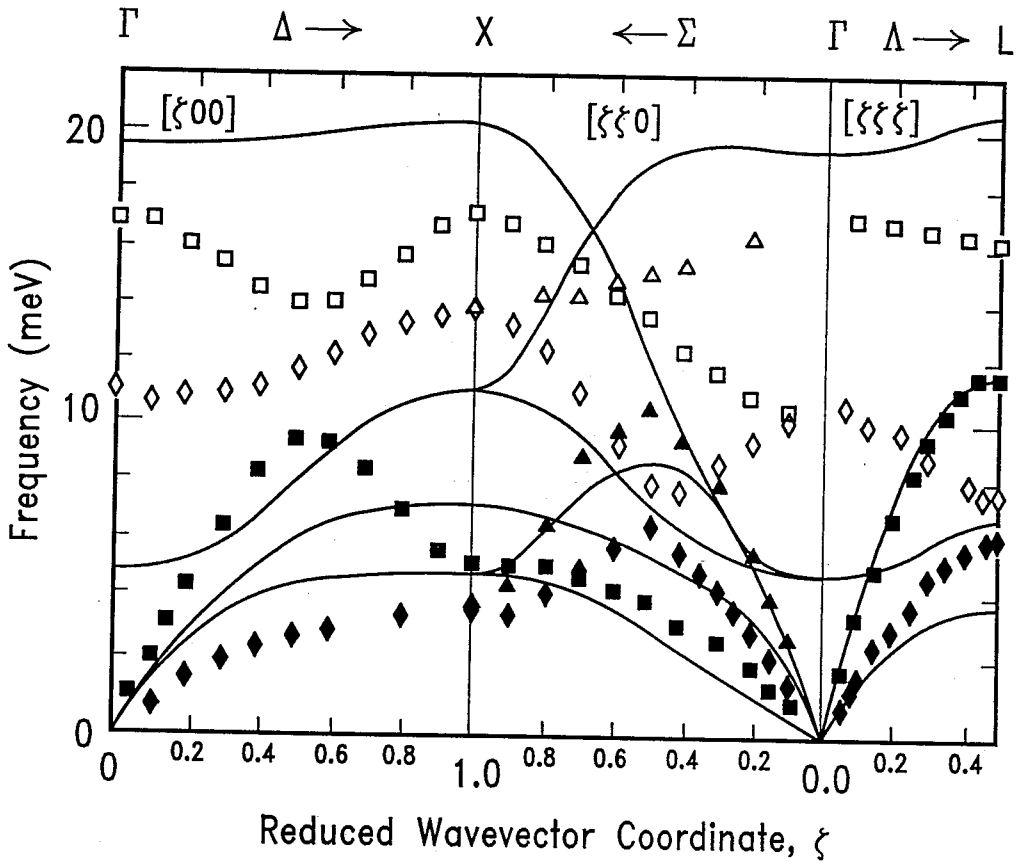

Figure 2.1: The phonon dispersion curves along [ζ,0,0], [ζ,ζ,0], and [ζ,ζ,ζ] directions in AgBr at 4.4K (Ref. [19]). Solid curves are from Model I and the symbols are experimental values.

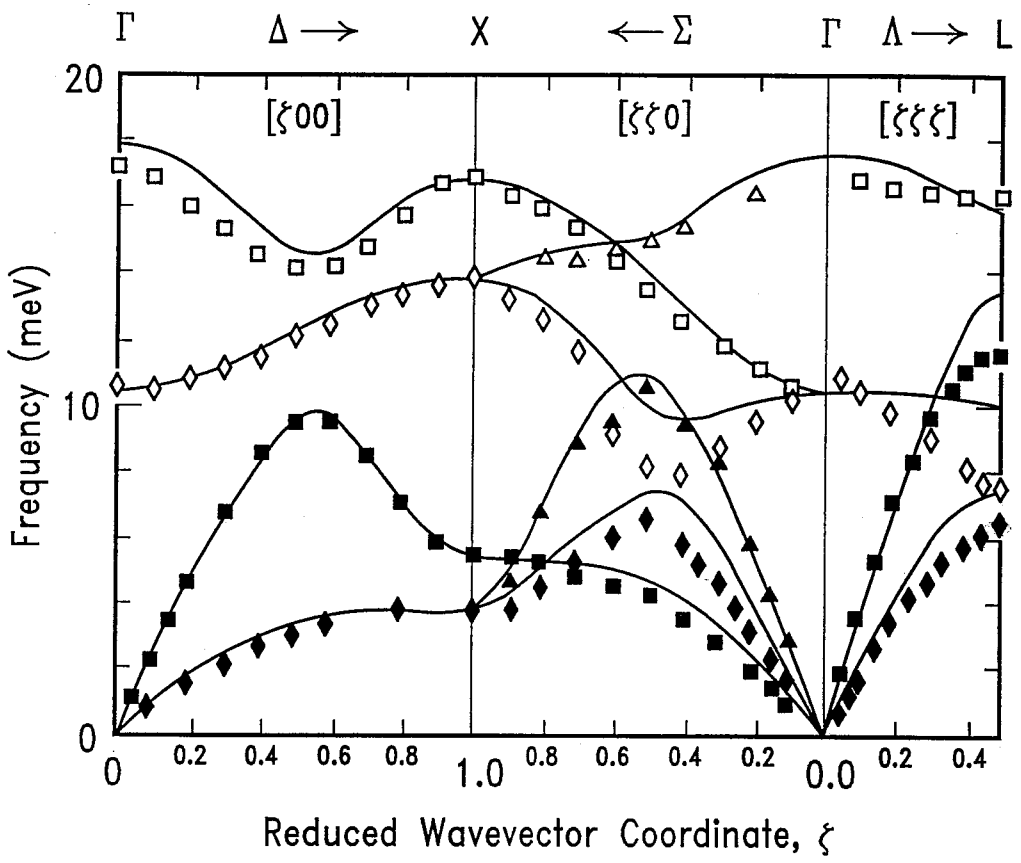

Figure 2.2: The phonon dispersion curves along [ζ,0,0], [ζ,ζ,0], and [ζ,ζ,ζ] directions in AgBr at 4.4K (Ref. [19]). Solid curves are from Model II and the symbols are experimental values.

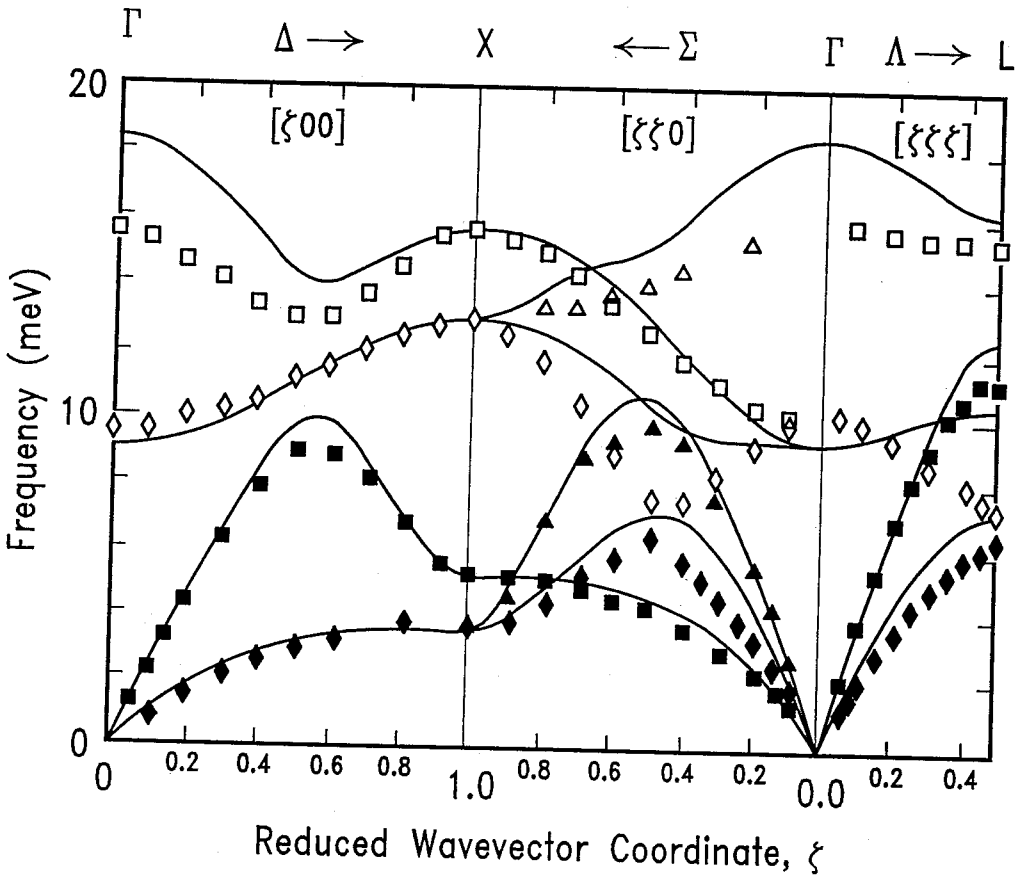

Figure 2.3: The phonon dispersion curves along [ζ,0,0], [ζ,ζ,0], and [ζ,ζ,ζ] directions in AgBr at 4.4K (Ref. [19]). Solid curves are from Model III and the symbols are experimental values.

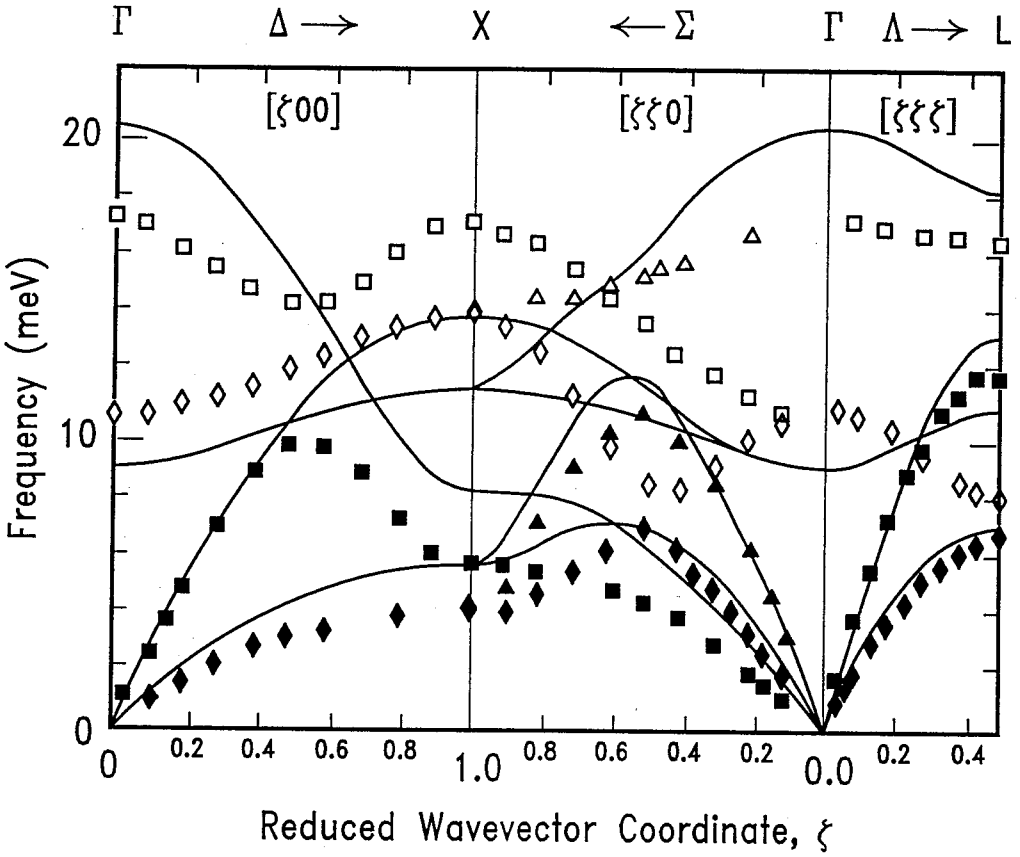

Figure 2.4: The phonon dispersion curves along [ζ,0,0], [ζ,ζ,0], and [ζ,ζ,ζ] directions in AgBr at 4.4K (Ref. [19]). Solid curves are from Model IV and the symbols are experimental values.

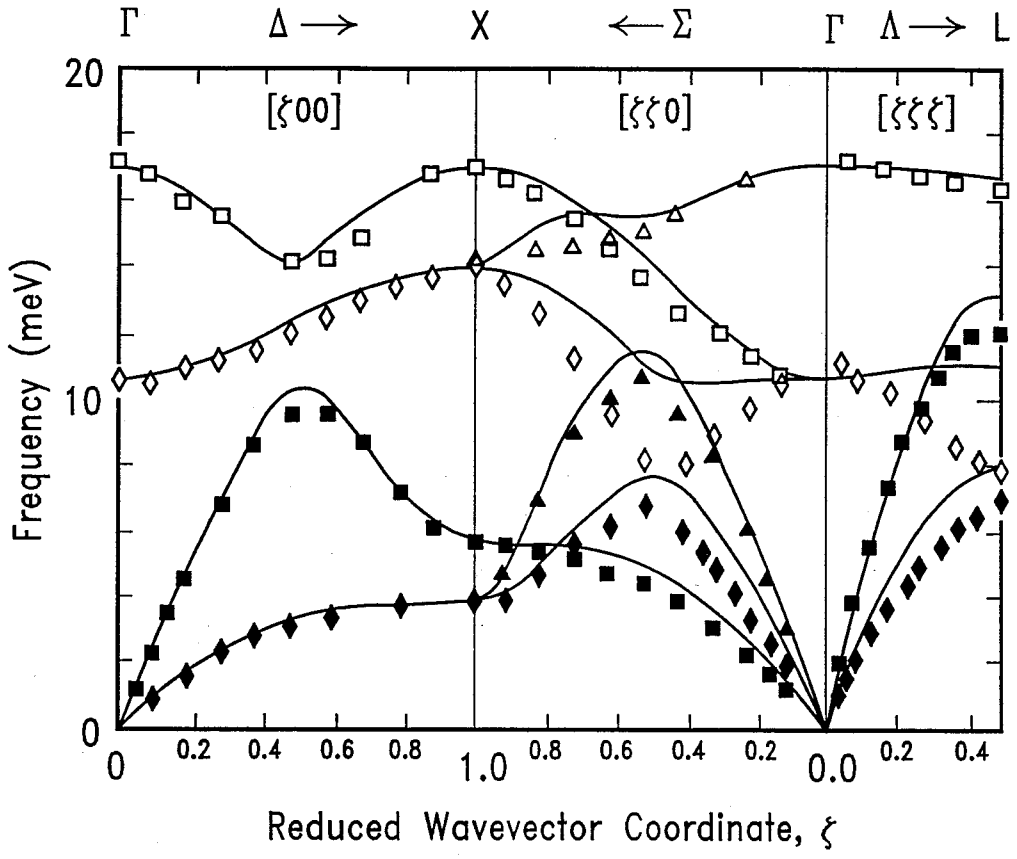

Figure 2.5: The phonon dispersion curves along [ζ,0,0], [ζ,ζ,0], and [ζ,ζ,ζ] directions in AgBr at 4.4K (Ref. [19]). Solid curves are from Model V and the symbols are experimental values.

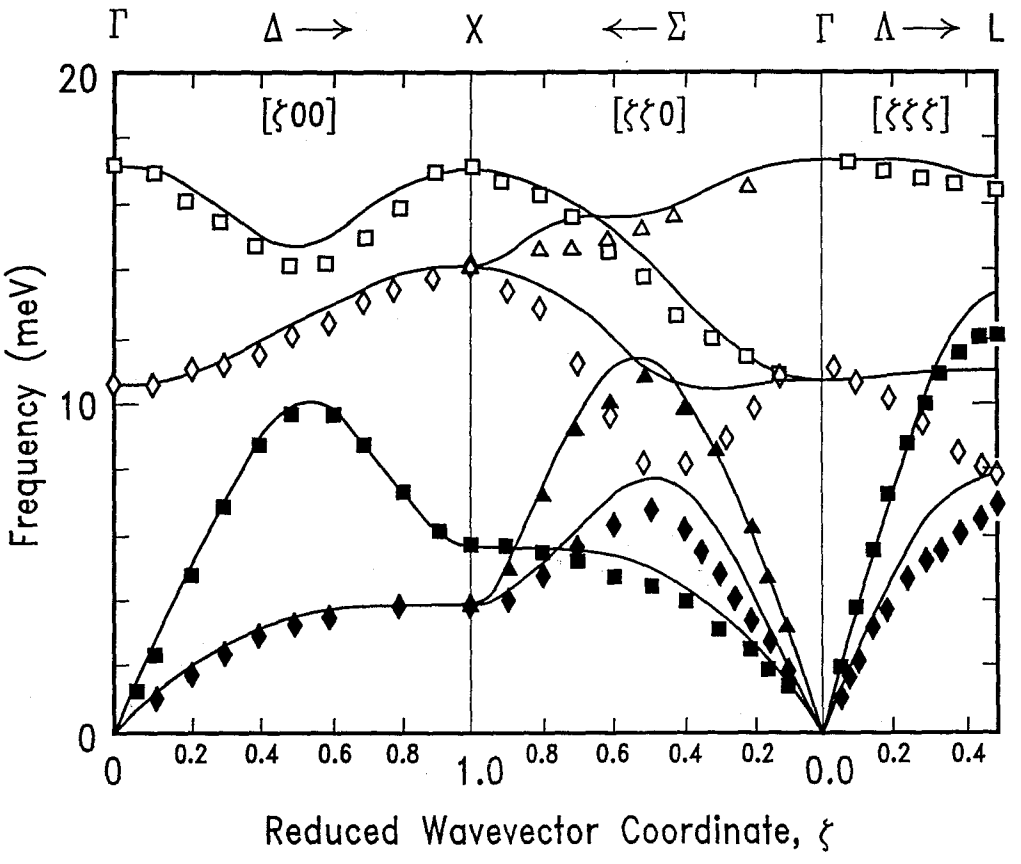

Figure 2.6: The phonon dispersion curves along [ζ,0,0], [ζ,ζ,0], and [ζ,ζ,ζ] directions in AgBr at 4.4K (Ref. [19]). Solid curves are from Model VI and the symbols are experimental values.

Table 2.1: Model parameters for AgBr. R_0, D_0, and γ are defined in Eq. (2.4).[a]

		Model					
		I	II	III	IV	V	VI
exp-6 parameters							
Ag_c-Ag_c	R_0	3.179	0.915	2.908	-	-	3.293
	D_0	0.192	0.143	0.159	-	-	0.172
	γ	12.411	6.694	11.865	-	-	11.878
Br_c-Br_c	R_0	6.836	-	3.734	-	-	3.858
	D_0	0.023	-	11.034	-	-	4.088
	γ	13.233	-	15.215	-	-	18.468
Ag_s-Ag_s	R_0	-	-	-	2.961	-	-
	D_0	-	-	-	0.124	-	-
	γ	-	-	-	12.950	-	-
Br_s-Br_s	R_0	-	-	-	3.739	-	-
	D_0	-	-	-	7.259	-	-
	γ	-	-	-	10.205	-	-
Ag_s-Ag_c	R_0	-	-	-	-	3.228	-
	D_0	-	-	-	-	0.175	-
	γ	-	-	-	-	12.053	-
Br_s-Br_c	R_0	-	3.829	-	-	3.831	-
	D_0	-	2.292	-	-	3.165	-
	γ	-	9.900	-	-	9.495	-
Ag_s-Br_c	R_0	-	-	-	-	4.162	4.078
	D_0	-	-	-	-	0.385	0.356
	γ	-	-	-	-	7.962	7.778
Br_s-Ag_c	R_0	-	4.217	-	-	4.309	4.093
	D_0	-	0.604	-	-	0.405	0.377
	γ	-	9.960	-	-	10.997	11.291
Ag_c-Br_c	R_0	3.000	-	6.072	-	-	3.836
	D_0	0.525	-	0.035	-	-	0.359
	γ	20.198	-	12.125	-	-	8.653
Ag_s-Br_s	R_0	-	-	-	5.590	-	3.932
	D_0	-	-	-	0.036	-	0.365
	γ	-	-	-	12.280	-	9.026
Variable shell parameters							
k_{Ag}		-	-	24742	57948	11951	18427
k_{Br}		-	1257	4555	2409	2001	1931
Fixed shell parameters							
Y_{Ag}		-	-	8.0	8.0	8.0	8.0
Y_{Br}		-	4.0	5.0	5.0	5.0	5.0

[a]The subscript c and s indicate the core and the shell, respectively. The shell charges are fixed parameters. R_0 is in units of Å, D_0 is in unit of Kcal/mol, γ is dimensionless, the spring constant k is in Kcal/mol-Å^2, and the charge Y is in atomic units.

Table 2.2: Elastic and optical constants of AgBr at 0K.[a]

	Units	Model I	II	III	IV	V	VI	Experimental
Γ_{TO}		43.6	85.4	79.8	76.5	86.1	85.5	86.1
Γ_{LO}		150.7	138.7	163.1	149.4	138.8	139.0	138.8
X_{TA}		43.0	31.5	31.7	31.6	31.2	31.4	31.1
X_{LA}	cm^{-1}	62.3	44.7	45.0	42.8	45.6	45.3	45.6
X_{TO}		92.5	113.7	114.1	106.8	114.0	114.4	114.0
X_{LO}		164.8	144.8	138.1	130.4	138.5	137.9	138.5
RMS[b]		22.3	1.4	5.6	6.3	0.0	0.4	-
ϵ_0		12.96	7.63	8.09	10.42	10.60	9.58	10.60
ϵ_∞		1.08	2.89	1.94	2.73	4.08	3.62	4.68
C_{11}		34.1	63.7	81.6	66.7	72.1	73.0	71.2
C_{12}	GPa	29.2	11.9	12.2	13.0	11.3	11.2	35.5
C_{44}		30.1	11.9	12.2	13.0	11.3	11.2	8.5
U	eV	8.12	8.90	8.58	8.42	9.34	9.01	9.33

[a]The phonons were fit to the Γ and X points.
[b]RMS is the root-mean-square deviation of frequencies.

2.1 shows the calculated and the experimental [19] phonon dispersion curves. The phonon dispersion frequencies, especially the optical phonons, are in poor agreement with the literature values. The lattice energy, listed is Table 2.2, is clearly too low and the elastic constants are not reproduced with reasonable accuracy. The parameters obtained for this model are fairly arbitrary, since any potential that represents the various properties of AgBr without polarization is unphysical.

Model II assumes that only the Br^- ion is polarizable. Early work on AgBr lattice dynamics [3, 12] demonstrates that with shells on the more polarizable Br^- ion a reasonable fit can be obtained. We first simulated the system with shells on Br^- only, to reveal the effect of the Br^- polarization in the crystal. Figure 2.2 shows the calculated and experimental phonon dispersion curves. Model II contains Ag^+ core - Ag^+ core, Br^- core - Br^- shell, and Ag^+ core - Br^- shell exp-6 interaction. The calculated phonon dispersion curves are in excellent agreement with experimental

values with only Br^- polarizable.

The calculated static dielectric constant is lower than the literature data. The result is to be expected given that the polarizability is also predicted to be too low. The static dielectric ϵ_0 is related to the crystal polarizability by Eq. (2.10), or more symbolically by

$$\epsilon_0 = 1 + \frac{4\pi}{\Omega}\alpha^{\text{crystal}} . \tag{2.12}$$

The crystal polarizability α^{crystal} is, to a first approximation, the sum of the atomic polarizabilities and the displacement polarizability [14]

$$\alpha^{\text{crystal}} = (\alpha^+ + \alpha^-) + \alpha^{\text{dis}} , \tag{2.13}$$

where α^+ is the atomic polarizability of the positive ion, α^- is the atomic polarizability of the negative ion, and α^{dis} is the displacement polarizability. From Eq. (2.13), we do not expect the dielectric constant to be accurately predicted, since the Ag^+ ion polarizability was not included. Table 2.2 confirms this expectation.

Models III–VI contain a Ag^+ shell as well as a Br^- shell. In Model III, only Coulomb interaction and core-core exp-6 are included. Model IV replaces the core-core exp-6 term in Model III with shell-shell exp-6 interactions. In Model V, there are only core-shell interactions. Model VI contains core-core exp-6 for like ions (Ag^+-Ag^+ and Br^--Br^-) and core-core, shell-shell, and shell-core exp-6 for different ions (Ag^+-Br^-). The calculated phonon dispersion curves for Model III (with exp-6 on cores only) and Model IV, V, and VI (with exp-6 on shells only) are shown in Figs. 2.3–2.6. We found that Model V provides the best fit among the various models (Table 2.2, Fig. 2.6).

Model II contains the fewest adjustable parameters among the various models and predicts phonon dispersion curves reasonably well. The one phonon density of states calculated for Model II at 0K is shown in Fig. 2.7. The distributions are

similar to those obtained from lattice dynamics [3]. The calculated specific heat versus temperature for Model II is shown in Fig. 2.8.

2.4 Discussion

The excellent agreement with the experimental data suggests that a pairwise potential can be applied with some confidence to the simulation of crystal properties. The model produced phonon dispersion curves in excellent agreement with the experimental data, especially the anomalous optical phonon curves unique to AgBr crystal. It also exhibits the characteristic inversion of the TA and TO modes in the phonon dispersion curves at the L point. The calculated dielectric constant and the lattice energy are also in accord with the measured values. The shell model has played an important role in modeling polarization effects in the ionic system. While the shell model has not been considered applicable to molecular dynamics simulations [25], in Chapter 3 we discuss the development of a new theoretical approach to dealing with shell motions. This approach renders the shell model usable in dynamical simulations.

The elastic constant C_{12} was not fit because the strong Cauchy violation, which requires many-body potentials such as three-body van der Waals interaction or bonding terms, cannot be simulated by our simple pairwise potential. This macroscopic parameter, however, should have little effect on microscopic details such as defect energies and ionic diffusion coefficients.

Practical calculations of the properties or the AgBr crystal have focused on point defects, because of their relevance to the photographic processes. For example, defect formation enthalpy and entropy as well as diffusion are of interest. The bond-angle bending terms introduced by Baetzold *et al.* [10], will hinder the calculation of defect properties, since a consistent treatment of the absence of the bonding at defect sites is not apparent. Therefore, we restrict our potential to a simple pairwise form that

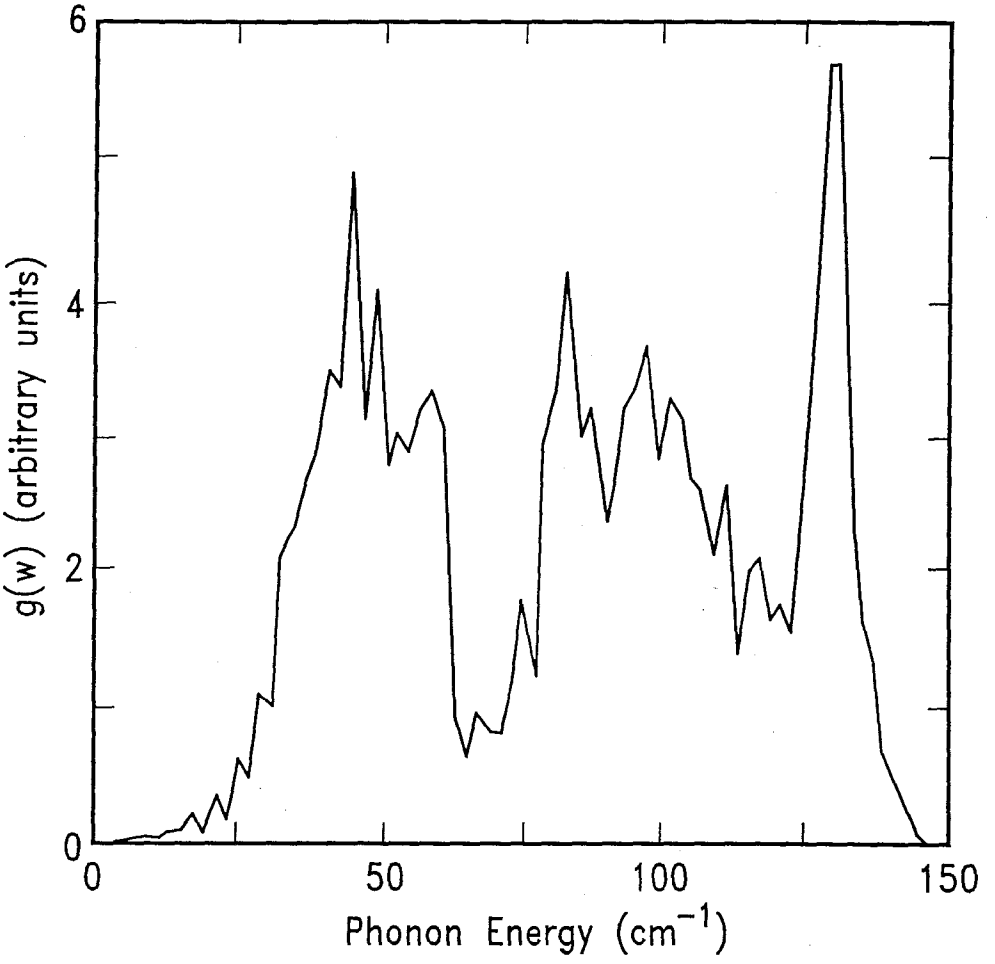

Figure 2.7: The one phonon density of states at 0K calculated for Model II.

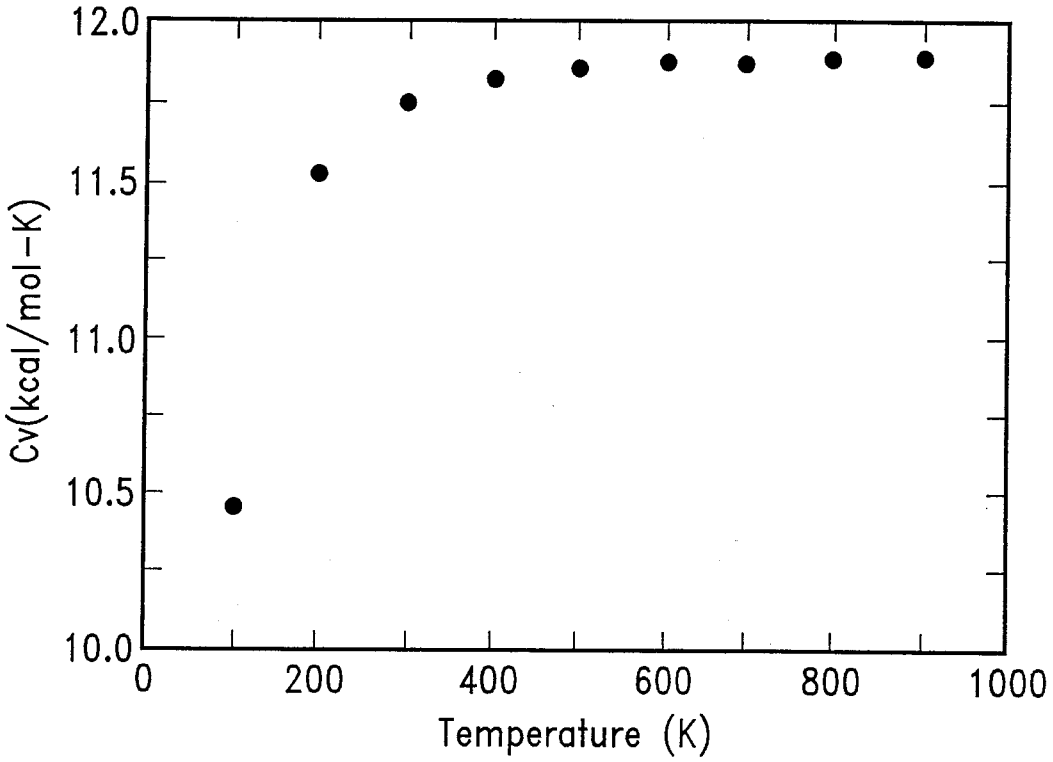

Figure 2.8: The specific heat versus temperature calculated for Model II.

still represent the characteristic properties of AgBr crystal.

Strikingly, Model II (only Br^- ion polarizable) predicts phonon dispersion curves that are essentially identical to those from the model with both ions polarizable. This indicates that the strong van der Waal forces and the high Br^- polarizability are responsible for the phonon dispersion curves that are unique to AgBr crystals. This outcome is consistent with the single crystal X-ray diffraction data on the electron density distribution map [26]. The radial distribution function of the bromine $4p$ electrons in the crystal is far more different from the free ion state than is the radial distribution function of the silver $4d$ electrons. We conclude, therefore, that the deformation of the outmost p-electrons of halogen ion, not the deformation of silver ions, in the crystal field is crucial to the understanding of the distinctive properties of silver halides.

In this simulation, the shell mass is set to approximately an electron mass (0.001 amu). We examined the effect of the shell mass by increasing it to 0.1 amu (*i.e.* factor of 100). The changes in physical properties are minimal (for example, the phonon frequencies shift by less than 1 cm^{-1}). The result is to be expected due to the disparate frequencies of shell and core vibrations. That is, the fast and the slow motions are separable (*i.e.* they do not affect each other). Our present treatment of the shell model differs from the commonly adopted shell model by Dick and Overhauser [27], in that there is a nonzero shell mass. The classical treatment of the shell motions ignores the zero-point motions. The magnitude of the zero-point energy of the cores are on the order of 0.1 eV, which is negligible compared to the lattice energy. On the other hand, the electron shell zero-point motions are about 5 to 10 eV, which is comparable to the lattice energy, and this quantum effect should be incorporated to fully illustrate the lattice dynamics. The assignment of a finite mass to the shell is vital, for it leads to an approximately correct quantum mechanical treatment of the shell model. A more detailed treatment of the shell model is presented in Chapter 3.

Table 2.3: Electronic polarizabilities of ions (in $\AA^3$).

Ion	TKS [27]	WC [28]	DBV [3]	GDM [29]	MB [30]	Model V
Ag^+	2.4	-	2.00	2.00	1.67	1.72
Br^-	4.16	4.023-4.606	5.03	4.28	4.55	4.02

Model V gave the best fit among these models. The model contains shell - core exp-6 interactions and also contains Coulomb interactions and harmonic springs. Model VI, though it contains more adjustable parameters, is not an improvement over Model V for simulating the crystal properties. Model V successfully predicted the overall trend of the phonon dispersion curves as well as the inversion of TA and TO phonon modes at L point without introducing any term that accounts for the quadrupolar deformation of Ag^+ ion. The phonon modes at the Γ and X points, the static dielectric constant ϵ_0, and the cohesive energy were fit to within 0.1% of the literature data (Table 2.2). The atomic polarizabilities obtained by this model were $\alpha_{Ag^+} = 1.72$ $\AA^3$ and $\alpha_{Br^-} = 4.02$ $\AA^3$. As illustrated in Table 2.3, the atomic polarizabilities determined by this model are plausible when compared to values determined by different methods [2, 28, 29, 30, 31].

2.5 Comparison with other Authors

The interaction potentials obtained by Bucher [11] and Baetzold *et al.* [10], though they contain three-body terms to take into account the Cauchy violation, were unable to predict the phonon dispersion curves. In Ref. [10], the phonon dispersion curves (especially the optical phonons), calculated from their 17 parameter model, are in poor agreement with experimental data. The authors concluded that quadrupolar deformation of the Ag^+ was needed to produce the optical phonon modes. Our

simple pairwise potential indicates that the strong van der Waals interactions and the polarization effects are important in understanding the phonon dispersion curves unique to AgBr crystal. We note that, if the number of parameters exceeds the data to be fit, unphysical parameters can result because there are multiple local minima on the surface to be minimized. In our simple pairwise potential, most of the crystal properties (*e.g.* dielectric constant and phonon dispersion curves) can be simulated. Since the potential contains only two-body interactions and does not have bonding terms, it can be easily applied to simulations of defect properties.

2.6 Conclusions

We have successfully produced a pairwise potential for AgBr, and the predicted properties agree fairly well with experimental values. This potential can be used in calculating properties involving defects. We have also shown that the Br^- polarizability and van der Waals interactions are important in the AgBr crystal field. The shell model provided a useful tool for examining the effect of polarization on the crystal properties, especially phonon dispersion frequencies and dielectric constants.

References

[1] J. F. Hamilton, Adv. Phys. **37**, 359 (1988).

[2] W. von der Osten, *The Physics of Latent Image Formation in Silver Halides*, International Symposium, Trieste, edited by A. Baldereschi, W. Czaja, E. Tosatti, and M. Tosi., (World Scientific, Singapore, 1983), p. 1.

[3] B. Dorner, W. von der Osten, and W Bührer, J. Phys. C. **9**, 723 (1976).

[4] W. Bührer, Phys. Stat. Sol. (b) **68**, 739 (1975).

[5] R. J. Friauf, J. Phys. (Paris) **20**, 705 (1987).

[6] B. A. Devlin and J. Corish, J. Phys. C. **20**, 705 (1987).

[7] R. A. Cowley, W. Cochran, B. N. Brockhouse, and A. D. B. Woods, Phys. Rev. **131**, 1030 (1963).

[8] L. Slifkin, Phil. Mag. A **64**, 1035 (1991).

[9] J. E. Mayer, J. Chem. Phys. **1**, 327 (1933).

[10] R. C. Baetzold, C. R. A. Catlow, J. Corish, F. M. Healy, P. W. M. Jacobs, M. Leslie, and Y. T. Tan, J. Phys. Chem. Solids **50**, 791 (1989).

[11] M. Bucher, Phys. Rev. B **30**, 947 (1984).

[12] K. Fischer, H. Bilz, R. Haberkorn, and W. Weber, Phys. Stat. Sol. **54**, 285 (1972).

[13] J. M. Prausnitz, R. N. Lichtenthaler, and E. G. de Azevedo, Molecular Thermodynamics of Fluid-Phase Equilibria, 2nd ed., (Prentice-Hall, New Jersey, 1986), Chapter 5.

[14] N. W. Ashcroft and N. D. Mermin, Solid State Physics, W. B. (Saunders Company, Philadelphia, 1976), Chapter 27.

[15] N. Karasawa and W. A. Goddard III, J. Phys. Chem. **93**, 7320 (1989).

[16] D. E. Williams, Acta Crystallogr. A **27**, 452 (1971).

[17] M. W. Deem, J. M. Newsam, and S. K. Sinha, J. Phys. Chem. **94**, 8356 (1990).

[18] B. R. Lawn, Acta Cryst. **16**, 1163 (1963).

[19] Y. Fujii, S. Hoshino, S. Sakuragi, and H. Kanzaki, J. W. Lynn, and G. Shirane, Phys. Rev. B **15**, 358 (1977).

[20] R. P. Lowndes and D. H. Martin, Proc. Roy. Soc. A **308**, 473 (1969).

[21] C. D. Thurmond, J. Am. Chem. Soc. **75**, 3929 (1953).

[22] M. Born and K. Huang, Dynamical Theory of Crystal Lattices, (Oxford University Press, Oxford, 1954).

[23] N. Karasawa and W. A. Goddard III, Macromolecules **25**, 7268 (1992).

[24] P. R. Vijayaraghavan, R. M. Nicklow, H. G. Smith, and M. K. Wilkinson, Phys. Rev. B **1**, 4819 (1970).

[25] J. Moscinski and P. W. M. Jacobs, Proc. R. Soc. Lond. A **398**, 141-171 (1985).

[26] H. Takahashi, S. Tamaki, and S. Sato, J. Phys. Soc. Jpn. **56**, 3583 (1987).

[27] B. G. Dick and A. W. Overhauser, Phys. Rev. **112**, 90 (1958).

[28] J. R. Tessman, A. H. Kahn, and W. Shockley, Phys. Rev. **15**, 890 (1953).

[29] J. N. Wilson and R. M. Curtis, J. Chem. Phys. **74**, 187 (1970).

[30] G. D. Mahan, Solid State Ionics **1**, 29 (1980).

[31] M. Bucher, Solid State Ionics **14**, 7 (1984).

Chapter 3

Effective Hamiltonians for Systems with Disparate Time Scales: The Quantum Shell Model and the Classical Statistical Shell Model

3.1 Introduction

In molecular dynamics and molecular mechanics simulations one usually replaces the electrons by springs, atomic charges, and van der Waals interactions, with the parameters chosen to fit some selection of properties [1]. Despite many successes, it is clear that such rigid-ion descriptions do not describe the response to external electric fields, such as polarizability, dielectric relaxation, piezoelectricity [2], hyperpolarizabilities, and dynamic polarization effects arising from the high electric fields present in the

crystal. Such difficulties with the rigid-ion model are manifest in the lattice dynamics of ionic systems. For example, the splitting of the longitudinal and transverse optical modes in alkali halides is incorrect [3, 4, 5, 6].

A simple model for including polarization effects in molecular mechanics is the isotropic shell model [3, 4, 5], based on the classical Drude Model [7, 8], where each atom is described in terms of two components: the core and the shell. The shell is connected to its core by an isotropic harmonic spring,

$$\delta E = \frac{1}{2}k(\delta R)^2 \tag{3.1}$$

$$k = \frac{s^2}{\alpha}, \tag{3.2}$$

where δR is the displacement of the shell from its core, α is the atomic polarizability, s is the shell charge in atomic units, and k is the spring constant. The shell then interacts with its core via the spring and with all other species via electrostatic interactions [3, 4, 5, 6, 7, 8, 9, 10]. The shell model has proved adequate for static crystal properties, including calculation of phonon dispersion curves [9, 10, 11, 12, 13], dielectric susceptibility, and piezoelectric tensors [2]. Fitting such a model to experimental data, however, often leads to unphysical parameters [6, 12, 13].

For dynamical simulations there are two choices for how to handle the shell coordinates. One is to assign zero mass to the shell. In this case the shell positions change adiabatically with motions of the cores but, kinetic energy effects are ignored. The other approach is to use finite mass. Adjusting the mass so that the shell vibrations correspond to typical (plasmon) excitation energies (5–20 eV) leads to very high frequencies for the shell motion and a concomitant decrease in the time step for dynamical simulations by factors of 10 [3] or more. Moreover, the shell motion should be quantized since the masses are similar to those of the electron.

Here we develop an analytic treatment of the shell model that renders it suit-

able for Monte Carlo and molecular dynamics simulations at any temperature. Our approach is based on the Drude model [7, 8], which treats the atoms as isotropic, three-dimensional harmonic oscillators. This model was adapted by London [14], with only minor modifications, to describe quantum mechanical dispersion forces.

Since the cores are $10^3 - 10^5$ times more massive than the shells, we consider them fixed during shell vibrations, *i.e.* we separate the shell and core motions. The shells equilibrate to the instantaneous positions of the cores according to statistical mechanical theory. The application of statistical mechanics is appropriate, since the nonlinear coupling between shell modes leads to energy flow and a statistical distribution of states. We then find the effective core Hamiltonian by "integrating out" the shell fluctuations with the help of classical or quantum statistical mechanical theory. The resulting effective Hamiltonian has two components. The first represents the energy due to the shells adopting the minimum energy position for any given core configuration. The second accounts for fluctuations, zero-point and excited-state motion in the quantum case and thermal fluctuations in the classical case.

3.2 Theory

We assume the shells are in thermal equilibrium with a bath at the average temperature of the cores and perform our calculations for the constant N, V, and T canonical ensemble. We then write the effective core Hamiltonian as the core kinetic energy K_{core} plus the canonical shell Helmholtz free energy,

$$H_{eff} = K_{core} + A = K_{core} - \frac{\ln Q_s}{\beta} , \tag{3.3}$$

where $\beta = 1/k_B T$. This effective Hamiltonian depends only on core positions, since the shell positions are integrated out in the calculation of Q_s.

Basically, we assume that the shells move much more rapidly than the cores, so that they can re-equilibrate instantaneously as the cores move. In the low temperature quantum case, the shell modes are generally in their ground states (excitation energies are $\sim$ 10 eV). This effective core Hamiltonian is then used in classical Monte Carlo or molecular dynamics simulations of the core motion, where the shell can be treated by either classical or quantum mechanics.

We start with a quadratic expansion of the shell Hamiltonian about the core positions. That is, we treat the shells as coupled, statistical harmonic oscillators. This assumption is usually valid since the core-shell interaction is much larger than the electrostatic couplings and the shell displacements are small. The resulting effective Hamiltonian for the cores is not quadratic and clearly contains many-body effects.

3.2.1 The Shell Hamiltonian

The first step in integrating out the shell coordinates $\{\mathbf{r}_j; j = 1, ..., N\}$ is to expand the total energy of the system $E(\{\mathbf{R}_i\}; \{\mathbf{r}_j\})$, about the core coordinates $\{\mathbf{R}_i; i = 1, ..., N\}$ to quadratic order,

$$E(\{\mathbf{R}_i\}; \{\mathbf{r}_j\}) = E_0(\{\mathbf{R}_i\}) + \sum_{i=1}^{N} d\mathbf{r}_i \left(\frac{\partial E}{\partial \mathbf{r}_i}\right)_{\mathbf{r}_i=\mathbf{R}_i} + \frac{1}{2}\sum_{i,j=1}^{N} d\mathbf{r}_i d\mathbf{r}_j \left(\frac{\partial^2 E}{\partial \mathbf{r}_i \partial \mathbf{r}_j}\right)_{\mathbf{r}_i=\mathbf{R}_i} , \quad (3.4)$$

where $\mathbf{dr}_i = \mathbf{r}_i - \mathbf{R}_i$, *i.e.* a small displacement of the shell from the position of the core, E_0 is the ion energy (including all interactions independent of $\mathbf{dr}_i$), and $E(\{\mathbf{R}_i\}; \{\mathbf{r}_j\})$ is the total energy of the system. We assume that $< \mathbf{r}_i > \approx \mathbf{R}_i$, so that $||d\mathbf{r}_i||$ is small.

Rewriting Eq. (3.4) in tensor notation, again ignoring higher order terms, leads to

$$E(\{\mathbf{R}_i\}; \{\mathbf{r}_j\}) = E_0 + \widetilde{\mathbf{dr}}\ \mathbf{E}' + \frac{1}{2}\widetilde{\mathbf{dr}}\ \mathbf{E}''\ \mathbf{dr} , \quad (3.5)$$

where $\mathbf{E}' \equiv \nabla_{\mathbf{r}}\mathbf{E}$, $\mathbf{E}'' \equiv \nabla_r \nabla_r \mathbf{E}$, $\mathbf{dr}$ is the 3N vector of differential shell coordinates,

and $\widetilde{\mathbf{dr}}$ is the transpose of $\mathbf{dr}$. From Eq. (3.5) the condition for equilibrium is

$$\mathbf{E}' + \mathbf{E}'' \cdot \mathbf{dr}_e = 0 \tag{3.6}$$

or

$$\mathbf{dr}_e = -(\mathbf{E}'')^{-1}\mathbf{E}' \ . \tag{3.7}$$

To eliminate the linear term in Eq. (3.5), we define $\mathbf{y} = \mathbf{dr} - \mathbf{dr}_e$ as the displacement from equilibrium, leading to

$$E(\{\mathbf{R}_i\};\{\mathbf{y}_j\}) = E_e + \frac{1}{2}\tilde{\mathbf{y}}\mathbf{E}''\mathbf{y} \ , \tag{3.8}$$

where

$$E_e = E_0 - \frac{1}{2}\tilde{\mathbf{E}}'(\mathbf{E}'')^{-1}\mathbf{E}' \tag{3.9}$$

is the energy with all shells at equilibrium ($\mathbf{y} = 0$). Therefore the shell Hamiltonian is

$$H_s = \sum_{i=1}^{N} \frac{\mathbf{p}_i^2}{2m_i} + E\left(\{\mathbf{R}_i\};\{\mathbf{r}_j\}\right) \ , \tag{3.10}$$

where $\mathbf{p}_i$ and m_i are the momentum and the mass of the shell, i=1,...N.

3.2.2 The Core Effective Hamiltonians

The Classical Statistical Shell Model

We now proceed to use classical statistical mechanics to integrate out the shell coordinates. This leads to an effective Hamiltonian of the form Eq. (3.3), depending only on $\mathbf{R}_i$.

The classical partition function for the shell coordinates is

$$\begin{aligned} Q_c(\{\mathbf{R}_i\}) &= \frac{1}{h^{3N}} \int e^{-\beta H_s(\{\mathbf{R}_i\};\{\mathbf{r}_j\})} d\mathbf{p}_1 ... d\mathbf{p}_N d\mathbf{r}_1 ... d\mathbf{r}_N \\ &= \frac{1}{h^{3N}} \int e^{-\beta(E_e + \frac{1}{2}\tilde{\mathbf{y}}\mathbf{E}''\mathbf{y} + \sum_{i=1}^{N} \frac{\mathbf{p}_i^2}{2m_i})} \prod_{i=1}^{N} d\mathbf{p}_i d\mathbf{r}_i \, . \end{aligned} \tag{3.11}$$

We simplify the integrand by diagonalizing the Hessian matrix $\mathbf{E}''$

$$\mathbf{E}''\mathbf{X} = \mathbf{X}\mathbf{\Lambda} \tag{3.12}$$

where $\mathbf{\Lambda}$ is the matrix of eigenvalues of $\mathbf{E}''$ and $\mathbf{X}$ is the matrix of eigenvectors. Thus Eq. (3.8) reduces to

$$E\left(\{\mathbf{R}_i\};\{\mathbf{r}_j\}\right) = E_e + \frac{1}{2}\tilde{\mathbf{y}}\mathbf{E}''\mathbf{y} = E_e + \frac{1}{2}\tilde{\mathbf{X}}\mathbf{\Lambda}\mathbf{X} \, . \tag{3.13}$$

Substituting Eq. (3.13) into Eq. (3.11), we obtain

$$Q_c(\{\mathbf{R}_i\}) = \frac{1}{h^{3N}} \left[\prod_{i=1}^{N} \left(\frac{2\pi m_i}{\beta} \right)^{\frac{3}{2}} \right] e^{-\beta E_e} \int e^{-\frac{\beta}{2}\tilde{\mathbf{X}}\mathbf{\Lambda}\mathbf{X}} \prod_{i=1}^{N} d\mathbf{X}_i \, . \tag{3.14}$$

The integrand in Eq. (3.14) is

$$\int e^{-\frac{\beta}{2}\tilde{\mathbf{X}}\mathbf{\Lambda}\mathbf{X}} \prod_{i=1}^{3N} d\mathbf{X}_i = \prod_{i=1}^{3N} \left(\frac{2\pi}{\beta\lambda_i} \right)^{1/2} = \left(\frac{2\pi}{\beta} \right)^{3N/2} (\det \mathbf{E}'')^{-1/2} \, , \tag{3.15}$$

including the determinant of $\mathbf{E}''$. This leads to

$$\ln Q_c = \gamma_c - \beta E_e - \frac{1}{2} \ln(\det \mathbf{E}'') \, , \tag{3.16}$$

where

$$\gamma_c = -3N \ln h + \frac{3}{2}\sum_{i=1}^{N} \ln\left(\frac{2\pi m_i}{\beta}\right) + \frac{3N}{2}\ln\left(\frac{2\pi}{\beta}\right) \tag{3.17}$$

represents all the factors in Eq. (3.16) independent of the core configuration. Thus, the effective Hamiltonian, H_{eff}, for motion of the cores, Eq. (3.3), becomes

$$\begin{aligned} H_{eff} &= K_{core} + A(\{\mathbf{R}_i\};\{\mathbf{P}_i\}) = \sum_{i=1}^{N} \frac{\mathbf{P}_i^2}{2M_i} - \frac{1}{\beta}\ln Q_c \\ &= \sum_{i=1}^{N} \frac{\mathbf{P}_i^2}{2M_i} + E_e + \frac{1}{2\beta}\ln(\det \mathbf{E}'') \,, \end{aligned} \tag{3.18}$$

where M_i is the core mass and the dependence on the shell coordinates has been successfully removed. For clarity we have omitted in Eq. (3.18) the factor γ_c since it is independent of the core configuration. The result is a core effective Hamiltonian that depends only on core positions $\mathbf{R}_i$ and momenta $\mathbf{P}_i$. We refer to this as the Classical Statistical Shell Model or CSSM.

As the temperature goes to zero, the CSSM Hamiltonian Eq. (3.18) reduces to the usual assumption that the shells remain in their minimum energy configuration. The last term in Eq. (3.18) is the entropy term of classical statistical mechanics. It is proportional to temperature, a classical effect, and is related to the Hessian matrix (second derivatives) of the energy with respect to shell positions. Note that the effective Hamiltonian contains many-body terms introduced by the determinant of the Hessian. That is, statistical averaging of a manifestly pairwise potential has produced many-body effects.

The Quantum Shell Model

The vibration frequencies from oscillations of the shell coordinates correspond to the frequencies of collective modes for the electrons. This will typically be in the range of 5–20 eV. With typical shell-core force constants this leads to a shell mass near

that of a free electron. Thus the shell motions should be quantized. If the shells are in equilibrium with a reservoir at temperature T, the average core temperature, the partition function from quantum statistical mechanics is

$$Q_q = Tr(e^{-\beta H_s}) \ . \tag{3.19}$$

Diagonalizing the mass weighted Hessian $\mathbf{E}''_m = \mathbf{M}^{-\frac{1}{2}}\mathbf{E}''\mathbf{M}^{-\frac{1}{2}}$ leads to

$$E(\{\mathbf{R}_i\};\{\mathbf{r}_j\}) = E_e + \frac{1}{2}\tilde{\mathbf{X}}_m\mathbf{\Lambda}_m\mathbf{X}_m \ , \tag{3.20}$$

where $\mathbf{M}$ is the diagonal matrix of the shell masses, $\mathbf{M}_{ij} = \delta_{ij}m_i$ and $\mathbf{X}_m = \sqrt{\mathbf{M}}\mathbf{X}$. All symbols are defined as in the classical case, with subscript m indicating mass weighted coordinates. The eigenvalue is $\lambda_{m_i} = (2\pi\nu_i)^2$, where ν_i is the vibration frequency of the normal mode.

Using Eq. (3.20) in Eq. (3.10), the quantum shell Hamiltonian becomes

$$H_s = \frac{1}{2}\sum_{i=1}^{3N}\left(\mathbf{X}^2_{m_i}\lambda_{m_i} + \dot{\mathbf{X}}^2_{m_i}\right) \tag{3.21}$$

with 3N harmonic oscillators. Substituting Eq. (3.21) into (3.19) and letting H_i be the Hamiltonian of oscillator i. The partition function Q becomes [15]

$$Q_q = e^{-\beta E_e}\prod_{i=1}^{3N} Tr e^{-\beta H_i} = e^{-\beta E_e}\sum_{n\geq 0} e^{-\beta E_n} \ , \tag{3.22}$$

where $E_n = \sum_{i=1}^{3N}(n+\frac{1}{2})h\nu_i$. Substituting E_n into (3.22), we obtain

$$Q_q = e^{-\beta E_e}\prod_{i=1}^{3N}\frac{e^{-\frac{1}{2}\beta h\nu_i}}{1-e^{-\beta h\nu_i}} \ . \tag{3.23}$$

Thus the effective Hamiltonian for motion of the cores is

$$H_{eff}^{core} = K_{core} + A(\{\mathbf{R}_i\}) = K_{core} - \frac{1}{\beta}\ln Q_q \tag{3.24}$$

$$= \sum_{i=1}^{N}\frac{\mathbf{P}_i^2}{2M_i} + E_e + \sum_{i=1}^{3N}\left[\left(\frac{h\nu_i}{2}\right) + \frac{1}{\beta}\ln\left(1-e^{-\beta h\nu_i}\right)\right] \tag{3.25}$$

$$\sim \sum_{i=1}^{N}\frac{\mathbf{P}_i^2}{2M_i} + E_e + \sum_{i=1}^{3N}\left(\frac{h\nu_i}{2}\right) \tag{3.26}$$

$$= \sum_{i=1}^{N}\frac{\mathbf{P}_i^2}{2M_i} + E_e + \frac{h}{4\pi}\sum_{i=1}^{3N}\sqrt{\lambda_{m_i}}\ . \tag{3.27}$$

The λ_{m_i} in Eq. (3.27) is related to the vibration frequency of the shell modes which depends on the core coordinates. The core effective Hamiltonian, Eq. (3.25) or Eq. (3.27), is independent of shell coordinates. We refer to this as the quantum shell model or QSM.

In the step from Eq. (3.25) to Eq. (3.26), we neglect the last term since the shell frequency $h\nu_i$ is generally 5–20 eV while $1/\beta = 0.025$ eV at room temperature. Thus equation Eq. (3.26) or Eq. (3.27) describes the shells as remaining in the ground quantum state during motions of the cores and represents the zero-point vibration of the shells. This is clearly a quantum effect and, unlike the classical case, does not depend on temperature. In the classical limit, h $\rightarrow$ 0 or $T \rightarrow \infty$, equation Eq. (3.25) reduces to the classical limit Eq. (3.18).

3.3 Classical Molecular Dynamics Simulations

The effective Hamiltonian [Eq. (3.27) for QSM or Eq. (3.18) for CSSM] is used for classical molecular dynamics simulations of the core motions. This requires taking derivatives of H_{eff} with respect to core coordinates to obtain forces. The presence of the shell Hessian or its eigenvalues in the effective Hamiltonian complicates the

equations since the derivatives of these quantities must be updated at every time step. There are a number of approaches to making this practical, some of which we mention below.

The Hessian for shell motions is dominated by large diagonal components due to the shell-core interactions; hence, it is expected that the remainder of the Hessian (which depends on various dipole-dipole interactions) could be treated as a perturbation and evaluated less frequently than every time step.

For CSSM the E'' matrix appears in the log of the determinant in Eq. (3.18). Using chain rules,

$$\frac{\partial H_{eff}}{\partial \mathbf{R}_k} = \frac{\partial E_0}{\partial \mathbf{R}_k} + \frac{\partial H_{eff}}{\partial \mathbf{E}'_i}\frac{\partial \mathbf{E}'_i}{\partial \mathbf{R}_k} + \frac{\partial H_{eff}}{\partial \mathbf{E}''_{ij}}\frac{\partial \mathbf{E}''_{ij}}{\partial \mathbf{R}_k} , \tag{3.28}$$

where the relation

$$\frac{\partial\ \ln(\det \mathbf{E}'')}{\partial \mathbf{E}''_{ij}} = (\mathbf{E}''^{-1})_{ij} \tag{3.29}$$

will be required, and the subscripts in the partial derivatives are summed over 3N coordinates. Thus we obtain an analytic form for the forces on the cores. This requires evaluating the first derivative of the core effective Hamiltonian (third derivatives of the energy) which must be updated at each time step of the dynamics. To avoid evaluating matrix inversions at every time step, a geometric series can be used to update the numerical value of $(\mathbf{E}'')^{-1}$.

$$(\mathbf{E}''+\epsilon)^{-1} = \left\{\mathbf{E}''[1+(\mathbf{E}'')^{-1}\epsilon]\right\}^{-1} = \left\{1-(\mathbf{E}'')^{-1}\epsilon+[(\mathbf{E}'')^{-1}\epsilon]^2-...\right\}(\mathbf{E}'')^{-1} , \tag{3.30}$$

where ϵ is a small increment, $\| \epsilon \| \ll 1$. In practical applications of Eq. (3.30):

$$\epsilon = \mathbf{E}''(t+\Delta t) - \mathbf{E}''(t) . \tag{3.31}$$

After iterative updating for several steps, one would invert the matrix $\mathbf{E}''$ explicitly to recover the exact $(\mathbf{E}'')^{-1}$. The time for full diagonalization and matrix inversion is proportional to N^3 while matrix multiplication required in Eq. (3.30) is also $O(N^3)$, but we expect the coefficient for the later process to be smaller.

For QSM we also use the chain rule to obtain the first derivative of the effective Hamiltonian.

$$\frac{\partial H_{eff}}{\partial \mathbf{R}_k} = \frac{\partial E_0}{\partial \mathbf{R}_k} + \frac{\partial H_{eff}}{\partial \mathbf{E}'_{m_i}} \frac{\partial \mathbf{E}'_{m_i}}{\partial \mathbf{R}_k} + \frac{\partial H_{eff}}{\partial \mathbf{E}''_{m_{ij}}} \frac{\partial \mathbf{E}''_{m_{ij}}}{\partial \mathbf{R}_k} + \frac{\partial H_{eff}}{\partial \lambda_{m_l}} \frac{\partial \lambda_{m_l}}{\partial \mathbf{E}''_{m_{ij}}} \frac{\partial \mathbf{E}''_{m_{ij}}}{\partial \mathbf{R}_k} \ . \tag{3.32}$$

Here the derivative of λ_{m_i} can be written as

$$\frac{\partial \lambda_{m_l}}{\partial \mathbf{E}''_{m_{kj}}} = \mathbf{X}_{m_{kl}} \mathbf{X}_{m_{jl}} = \frac{\partial \lambda_{m_l}}{\partial \mathbf{E}''_{m_{jk}}} \ , \tag{3.33}$$

where $\mathbf{X}_{m_{kl}}$ is the kth element of mass weighted eigenvector l. Eq. (3.33) involves diagonalization of the Hessian matrix $\mathbf{E}''_m$. Explicit diagonalization at every time step might be avoided using perturbation theory. Thus if $\mathbf{E}''_m$ is nondegenerate, the perturbation theory for $\mathbf{E}''_m = \mathbf{M}_0 + \mathbf{M}_1$ takes the form [16],

$$\begin{aligned}
\lambda_{m_i} &= \lambda^0_{m_i} + < \mathbf{x}^0_{m_i} | \mathbf{M}_1 | \mathbf{x}^0_{m_i} > + \sum_{j \neq i} \frac{| < \mathbf{x}^0_{m_j} | \mathbf{M}_1 | \mathbf{x}^0_{m_i} > |^2}{\lambda^0_{m_i} - \lambda^0_{m_j}}, \\
\mathbf{x}_{m_i} &= \mathbf{x}^0_{m_i} + \sum_{k \neq i} \mathbf{x}^0_k \left[\frac{< \mathbf{x}^0_{m_k} | \mathbf{M}_1 | \mathbf{x}^0_{m_i} >}{\lambda^0_{m_i} - \lambda^0_{m_k}} \left(1 - \frac{< \mathbf{x}^0_{m_i} | \mathbf{M}_1 | \mathbf{x}^0_{m_i} >}{\lambda^0_{m_i} - \lambda^0_{m_k}} \right) \right. \\
&\quad \left. + \sum_{j \neq i} \frac{< \mathbf{x}^0_{m_k} | \mathbf{M}_1 | \mathbf{x}^0_{m_j} >< \mathbf{x}^0_{m_j} | \mathbf{M}_1 | \mathbf{x}^0_{m_i} >}{\left(\lambda^0_{m_i} - \lambda^0_{m_k} \right) \left(\lambda^0_{m_i} - \lambda^0_{m_j} \right)} \right] ,
\end{aligned} \tag{3.34}$$

where $\lambda^0_{m_i}$ and $\mathbf{x}^0_{m_i}$ are the ith element of the $0th$ order eigenvalue and eigenvector of $\mathbf{E}''$, respectively. The $\mathbf{x}_{m_i}$ should be normalized to unity at each step.

In analogy with Eq. (3.30), perturbation theory can be used to update the eigenvalues and eigenvectors. This allows λ_{m_i} and $\mathbf{x}_{m_i}$ to be updated iteratively without

having to diagonalize the matrix. Again, the matrix should be diagonalized after several steps to recover the exact eigenvalues and eigenvectors.

3.4 Discussion

3.4.1 Quantum Shell Model

In order to characterize the polarization of atoms in materials (an effect that originates from electron motions), the shell model is introduced into the potential. The shell vibration states should be quantized, and we expect the outcome from classical mechanics descriptions to be in considerable error. The Quantum Shell Model allows molecular dynamics and Monte Carlo simulations (for those materials where the simple shell model description of forces is valid).

A bonus with QSM is that the zero-point motion of the shells in Eq. (3.27) includes the fluctuating dipoles responsible for the London dispersion or van der Waals attractions ($-C/R^6$). This is a fluctuation-induced force resulting from instantaneous dipole-dipole interactions. To illustrate this, consider the general Eq. (3.27), for two spherical neutral particles a and b. The interaction potential becomes

$$E = \frac{s_a s_b}{|\mathbf{R}|} + \frac{s_a s_b}{|\mathbf{r}_b - \mathbf{r}_a|} - \frac{s_a s_b}{|\mathbf{R} - \mathbf{r}_a|} - \frac{s_a s_b}{|\mathbf{r}_b|} + \frac{1}{2} k_a \mathbf{r}_a^2 + \frac{1}{2} k_b (\mathbf{r}_b - \mathbf{R})^2 \qquad (3.35)$$

where $\mathbf{0}$, $\mathbf{R}$, $\mathbf{r}_a$, and $\mathbf{r}_b$ are the position vectors for the core_a, core_b, shell_a, and shell_b with respect to core_a. k_a is the spring constant and $-s_a$ is the shell charge. Thus the

Hessian matrix takes the form

$$\mathbf{E}'' = \begin{bmatrix} k_a & 0 & 0 & \frac{s_a s_b}{R^3} & 0 & 0 \\ 0 & k_a & 0 & 0 & \frac{s_a s_b}{R^3} & 0 \\ 0 & 0 & k_a & 0 & 0 & -\frac{2 s_a s_b}{R^3} \\ \frac{s_a s_b}{R^3} & 0 & 0 & k_b & 0 & 0 \\ 0 & \frac{s_a s_b}{R^3} & 0 & 0 & k_b & 0 \\ 0 & 0 & -\frac{2 s_a s_b}{R^3} & 0 & 0 & k_b \end{bmatrix} . \tag{3.36}$$

The eigenvalues can be found analytically, with the last term in H_{eff}, Eq. (3.22), becoming

$$(3\nu_a + 3\nu_b) - \frac{3h}{2}\left(\frac{\nu_a \nu_b}{\nu_a + \nu_b}\right)\alpha_a \alpha_b \left(\frac{1}{R^6}\right) + O\left(\frac{1}{R^{12}}\right) , \tag{3.37}$$

where $\nu_a = \frac{1}{2\pi}\sqrt{\frac{k_a}{m_a}}$, $\nu_b = \frac{1}{2\pi}\sqrt{\frac{k_b}{m_b}}$, and α is defined in Eq. (3.2). The dispersion energy is the difference between the zero-point energy of the isolated particles and that of the interacting particle. The result is consistent with the dispersion energy derived from the Drude model for two particles, each harmonically and isotropically bound to its individual equilibrium position [7, 8].

For two identical atoms the London dispersion energy from Eq. (3.37) is

$$E_{disp}(R) \sim -C_6 \left(\frac{1}{R^6}\right) , \tag{3.38}$$

where

$$C_6 = \frac{3}{4}\frac{s\alpha^{3/2}}{m^{1/2}} \qquad \text{(in atomic units)} . \tag{3.39}$$

With three spherical neutral particles, the quantum formula Eq. (3.27) leads to a sum of pair terms as in Eq. (3.38) plus the Axilrod-Teller correction [17],

$$\delta E_{A-T}(R) = C_{A-T}\,\frac{(1 + 3cos\theta_i cos\theta_j cos\theta_k)}{(R_{ij} R_{jk} R_{ki})^3} , \tag{3.40}$$

where

$$C_{A-T} = \frac{9}{16}\frac{s\alpha^{5/2}}{m^{1/2}} \qquad \text{(in atomic units)} . \tag{3.41}$$

Here θ_i, θ_j, θ_k are the three angles of the triangle with sides R_{ij}, R_{jk}, and R_{ki}. This corresponds to the first-order correction for 3-body potentials. These results demonstrate that, for the simplest cases of two or three particles at moderate separation, equation Eq. (3.27) predicts the familiar $1/R^6$ and Axilrod-Teller terms [14, 17].

These results [Eq. (3.38) and Eq. (3.40)] from Eq. (3.27) are limiting cases, presented here to reveal the validity of this formalism. Unlike the Drude model, which constructs the potential with sets of pairwise interactions, the effective Hamiltonian obtained via the statistical mechanical approach clearly contains the many-body interactions. Although analytic derivation of the formulas for the higher order interactions (*e.g.* four or five body interactions) is rather complex and sometimes impractical, the numerical calculations are straightforward. The number of particles to be included in the simulations can be thousands, depending on the system of interest. Furthermore, the derivation of the effective Hamiltonian puts no restrictions on the distance range where the formula applies. Thus the interaction potential can be evaluated numerically at intermediate separations. Our Hamiltonians, however, do not take into account the overlap of the electron clouds or the exchange interactions (Pauli principle).

For molecular systems the shell parameters [s and α in Eq. (3.2)] can be determined by fitting to molecular polarizabilities. Kim and Gordon [18] investigated the resulting London dispersion interactions for closed-shell atoms, ions, and molecules and compared with C_6 values measured from gas-phase scattering experiments. The "effective number of electrons" responsible for the dispersion force was determined by fitting with experimental C_6 data. This oscillator approach describes reasonably well the various charge-dipole and dipole-dipole interactions. The ν_i for Ar deter-

mined by $\nu_i = \frac{4}{3}\left(\frac{c_6}{\alpha^2}\right)$ is about 19eV, which shows the necessity for quantization of the shell model. Kim and Gordon chose the shell mass as sm_e (where m_e is the electron mass) so that the shell charge could be uniquely determined from Eq. (3.39) (given the C_6 coefficient and the polarizability). The shell mass, however, can be treated as an extra parameter since the oscillating electron model does not enforce the exact mechanism of individual electron motion. We suggest choosing it to fit the strongly allowed electronic transitions or plasmon modes.

The shell model, proposed by Dick and Overhauser [3] and used extensively thereafter, does not take into account the kinetic energy of the shells. Thus, it ignores the high frequency zero-point motion of the shells. Generally the shell mass is assigned to zero, which implies no force exerted on the shells when solving Newton's equations of motion in atomic simulations. This may account for the nonphysical parameters [6, 12, 13] obtained with this model. Naive inclusion of the shell mass into standard MD simulations would not only require time steps 10^3 shorter (light mass) but would also lead to incorrect results, since quantum effects are not included.

Since the London dispersions are already included in the quantum formula, classical dynamics simulations using Eq. (3.27) should *not* include these terms in the explicit nonbonded potential [(E_0 of Eq. (3.4)]. Thus only the short-range repulsions (Pauli exclusion) and electrostatic interactions would be included. Since the short range repulsions can be calculated easily from quantum mechanical wavefunctions (*e.g.* Hartree Fock) that *do not* include London dispersion, this might simplify the derivation of the potentials.

The effective Hamiltonians developed here are not restricted to the simple isotropic harmonic shell model in Eq. (3.1). They could be used with more general shell formulations involving shells at bond midpoints or other interstitial position [19] or a non-isotropic force constant matrix.

With either the QSM or the CSSM formula, the second-order corrections for two

neutral particles leads to terms of the order of $1/R^{12}$. This differs from the usual result at large R where [8]

$$E_{London} = -\frac{C_6}{R^6} - \frac{C_8}{R^8} - \frac{C_{10}}{R^{10}} \tag{3.42}$$

(for neutral spherical particles). The origin of this discrepancy is the harmonic expansion in Eq. (3.4), which neglects multipole interactions higher than dipole-dipole. For example, the $1/R^8$ term comes from a dipole-quadrupole interaction that contributes in second order perturbation theory. The appropriate perturbation is cubic in $d\mathbf{r}_i$ which is not present in Eq. (3.4). For most of the systems of interests, however, the harmonic description is appropriate.

3.4.2 Classical Statistical Shell Model

Using the classical formula Eq. (3.18) to consider the interactions of three atoms, the last term in the effective Hamiltonian Eq. (3.18) leads asymptotically to a sum of $1/R^6$ attractions (as in Eq. (3.38)), plus a 3-body term similar to Eq. (3.40)

$$\begin{aligned} E(R) \quad \sim \quad & const - 4\left(\frac{3}{4}\frac{\alpha^2}{\beta}\right)\left[\left(\frac{1}{R_{ij}^6}\right) + \left(\frac{1}{R_{jk}^6}\right) + \left(\frac{1}{R_{ki}^6}\right)\right] \\ & + \frac{16}{3}\left(\frac{9}{16}\frac{\alpha^3}{\beta}\right)\frac{(1 + 3cos\theta_i cos\theta_j cos\theta_k)}{(R_{ij}R_{jk}R_{ki})^3} \ . \end{aligned} \tag{3.43}$$

For CSSM, however, the presence of β leads to a linear dependence on temperature. This temperature dependence is a well-known classical result [20] whereas London dispersion is a quantum effect [14]. This suggests that in using Eq. (3.18), the β in the last terms must be fixed in some way so as to approximate the quantum result. An additional problem with CSSM is that the coefficients of the 2-body and 3-body corrections in Eq. (3.43) have different proportions than in the quantum case. This

is to be expected since the $\ln(\det \mathbf{E}'')$ in Eq. (3.18) is not proportional to the sum of the square roots of the eigenvalues of $\mathbf{E}''_m$ involved in Eq. (3.27). Even so, Eq. (3.18) may be useful when the zero-point energy of the faster motion to be integrated out is insignificant compared to the average energy. In this case many of the higher modes will be activated and the system should exhibit a statistical population of states. At high temperature when the classical limit is valid, (*e.g.* motions in polymer chains) Eq. (3.18) might provide an efficient way to implement statistical averaging. It might also be a useful approximation when the evaluation of eigenvalues from quantum case (which involves diagonalization of the Hessian matrix) is not practical.

3.4.3 Application to Other Systems

The quantum H_{eff} in (3.27), and the classical statistical H_{eff} in (3.18), can be used for other systems containing light particles interacting with much heavier particles. For example, in the molecular dynamics of molecules or solids, particularly of organic polymers and biopolymers, the modes involving hydrogen have frequencies large compared to thermal energies. Thus they should be described in the zero quantum state, with a spatial distribution independent of temperature, and would not contribute to the specific heat. Classical dynamics, however, leads to temperature dependent motions and a full contribution to the specific heat. The quantum or classical effective Hamiltonians (3.27) or (3.18) could be used to eliminate the H motions from the dynamical description of the heavy atom coordinates. This should be much more accurate than the common approach of implicitly including the hydrogens into the adjacent heavy atoms (united atoms) [21].

For molecules and crystals containing positronium, the quantum equation would allow the positronium motions to be quantized, providing a means for efficiently simulating the dynamics.

In addition, analogous quantum or classical statistical effective Hamiltonians could be derived for other systems containing motions with disparate time scales (*e.g.* torsions of polymer chains, librations in molecular crystals, and diffusion in solids).

3.5 Comparison to Other Methods

Effective Hamiltonians involving an analytic description of *both* shell and core coordinates have previously been derived for shell models of solids [22]. These treatments involve additional simplifying assumptions about the shell-core and core-core interactions and even about the dimensionality of the system. Our approach is distinct from these previous analytic approaches in that we treat only the shells analytically. Thus, we leave the evaluation of the core properties as a numerical task to be handled with standard numerical programs.

The statistical description in shell model should have advantages over analytic integration of a harmonic approximation to the motion of the light particles [23]. For example, pure harmonic approximations do not allow energy flow between oscillators, thereby preventing the system from equilibrating. Moreover, the classical harmonic oscillator without statistical averaging overestimates the position density at the classical turning points, whereas classical and quantum statistical mechanics predict Gaussian position densities [24].

The harmonic shell approximation has been found inadequate for the treatment of oxides and chalcogenides with ferroelectric soft modes (where nonlinear polarization response is important) [25]. It is possible that, with an anisotropic k matrix, the many-body effects implicit in the QSM or CSSM formulations would abrogate these difficulties. This approach, however, remains to be investigated.

3.6 Conclusions

We have provided a formalism for simulating motions with disparate time scales, with the focus on the simulation of polarization effects in molecules and solids. Using statistical mechanical theory, we have obtained analytic effective core Hamiltonians which include the effects of an ensemble of quantized shell coordinates (QSM) or of a classical statistical distribution (CSSM) on the motions of the cores. The QSM approach should provide an accurate description of electron fluctuations. For example, QSM automatically leads to London dispersion interactions.

These methods should also be useful for including the effects of light particles on the motions of heavier atoms, which are treated with classical molecular dynamics. This statistical approach, together with the suggested numerical techniques, should provide a means to efficiently incorporate rapid dynamical position fluctuations.

References

[1] N. Karasawa, S. Dasgupta, and W. A. Goddard III, J. Phys. Chem. **95**, 2260 (1991).

[2] N. Karasawa and W. A. Goddard III, Macromolecules **25**, 7268 (1992).

[3] B. G. Dick and A. W. Overhauser, Phys. Rev. **112**, 90 (1958).

[4] J. R. Tessman, A. H. Kahn, and W. Shockley, Phys. Rev. **92**, 890 (1953).

[5] N. W. Ashcroft and N. D. Mermin, Solid State Physics, W. B. Saunders Company: Philadelphia, Chapter 27 (1976).

[6] P. Brüesch, Phonons: Theory and Experiments, (Springer-Verlag, Berlin, 1982).

[7] P. K. L. Drude, The Theory of Opitcs, (Longmans Green, London, 1933).

[8] For a simple discussion, see J. O. Hirskhfelder, C. F. Curtiss, and R. B. Bird, Molecular Theory of Gases and Liquids, second corrected printing, (John Wiley & Sons, New York, 1963), Chapter 13.

[9] A. D. B. Woods, W. Cochran, and B. N. Brockhouse, Phys. Rev. **119**, 980 (1960).

[10] R. A. Cowley, W. Cochran, B. N. Brockhouse, and A. D. B. Woods, Phys. Rev. **131**, 1030 (1963).

[11] W. Cochran, R. A. Cowley, G. Dolling, and M. M. Elcombe, Proc. Roy. Soc. (London) **293A**, 433 (1966).

[12] P. R. Vijayraghavan, R. M. Nicklow, H. G. Smith, and M. K. Wilkinson, Phys. Rev. B **1**, 4819 (1970).

[13] Y. Fujii, S. Hoshino, S. Sakuragi, H. Kanzaki, J. W. Lynn, and G. Shirane, Phys. Rev. B **15**, 358 (1977).

[14] F. London, Z. Physik. Chem. **B11**, 222 (1930).

[15] J. E. Mayer and M. G. Mayer, Statistical Mechanics, Second Edition, (John Wiley & Sons, New York, 1977), Chapter 11; D. Chandler, Introduction to Modern Statistical Mechanics, (Oxford University Press, New York, 1987), Chapter 4.

[16] L. I. Schiff, Quantum Mechanics, Third Edition, (McGraw-Hill Publishing Company, New York, 1968), Chapter 8.

[17] B. M. Axilrod and E. Teller, J. Chem. Phys. **11**, 299 (1943).

[18] Y. S. Kim and R. G. Gordon, J. Chem. Phys. **61**, 1 (1974).

[19] M. Li and W. A. Goddard, Phys. Rev. B. **40**, 12155 (1989).

[20] H. Li and M. Kardar, Phys. Rev. Lett. **67**, 3275 (1991).

[21] S. J. Weiner, P. A. Kollman, D. A. Case, U. Chandra Singh, C. Ghio, G. Alagona, S. Profeta and P. Weiner, J. Am. Chem. Soc. **106** 765 (1984); B. R. Brooks, R. E. Bruccoleri, B. D. Olafson, D. J. States, S. Swaminathan and M. Karplus, J. Comput. Chem. **4**, 187 (1983).

[22] A. Dobry and A. Greco, Phys. Rev. B **42**, 6675 (1990).

[23] M. Tuckerman, B. J. Berne, and G. J. Martyna, J. Chem. Phys. **97**, 2635 (1992)

[24] M. W. Deem, J. M. Newsam, and J. A. Creighton, J. Am. Chem. Soc. **114**, 7198 (1992).

[25] H. Bilz, G. Benedek, and A. Bussmann-Holder, Phys. Rev. B **35**, 4840 (1987).

Chapter 4

Fullerenes with Metals Inside

4.1 Introduction

An unexpected peak at 720 amu in a carbon cluster mass spectrum lead to the discovery of the soccer ball shaped molecule now called a fullerene or C_{60}[1]. The shape of the spheroidal hollow cage structure was presaged by the fascinating geodesic dome built by the architect R. Buckminster Fuller (see Ref. [1], and reference therein). *Buckminsterfullerene* was chosen to refer to C_n with closed structures of pentagons and hexagons. This proposed structure was confirmed after macroscopic quantities of C_{60} became available [2]. The term *fullerene* was then established to denote a cage-like molecule that is composed of only sp^2 bonded carbon.

The prediction that atoms can be trapped inside the cage was soon demonstrated by laser vaporization of graphite target with a lanthanum salt [3]. A notation X@C_n was introduced to denote the species X located inside the C_n cage [4]. Fullerenes have continued to inspire fundamental research as well as suggestions for practical applications [5, 6, 7, 8]. The carbon cage provides a new class of host where an individual atom, ion, or cluster can be isolated on a molecular scale [4, 9, 10]. Fullerenes

molecules doped with metal atoms called endohedral metallofullerenes, have recently been synthesized with an electric arc discharge of graphite and metal oxides [7, 11, 12]. Metals such as Sc, Y, La, Er, and Gd can be trapped inside spherical carbon cages (*e.g.* C_{76}, C_{82}, and C_{84}) to form stable molecules called endohedral metallofullerenes [8, 10, 13]. A typical cage structure with metal cluster inside is displayed in Fig. 4.1. Noble gas such as He, Ar, Kr, and Xe have also been successfully introduced into fullerene cages [15, 16, 17]. The resulting stable compounds, such as $^3He@C_{60}$ and $^3He@C_{70}$, have been characterized with NMR [15].

It is possible that appropriate internal dopants can be used to tune the physical and chemical properties of the molecules, giving rise to a family of materials with potential applications as catalysts, nonlinear optical or ferroelectric materials, transport agents for refractory or reactive species, photosensitizers, or electronic materials [5]. Metallofullerenes containing Sc, Y, La, or lanthanide atoms form readily, and they have been characterized by a variety of methods [13, 18, 19, 20, 21]. Detailed characterization and structural studies have been impeded by the difficulty in preparing pure samples. Methods for purifying these species using multiple stages of high performance liquid chromatography (HPLC) have been reported recently [19, 21, 22, 23]. Initial characterization work, including UV-Vis spectroscopy [19, 21], infrared spectroscopy [21], and scanning tunneling microscopy (STM) imaging [20], has been done.

Spectroscopic characterization and theoretical calculations have shed light on the geometric and electronic structure of metallofullerenes [19, 20, 24]. This novel form of carbon is expected to have interesting properties. For example, the conductivity of a solid metallofullerene may be affected by the dopant, possibly leading to superconductivity, as in the case of interstitially doped solid C_{60} crystals [25]. Energy levels of dopants are also predicted to be shifted, leading to novel transitions in optically active metals such as Er [26].

Due to the low yield of metallofullerene and lack of efficient separation techniques,

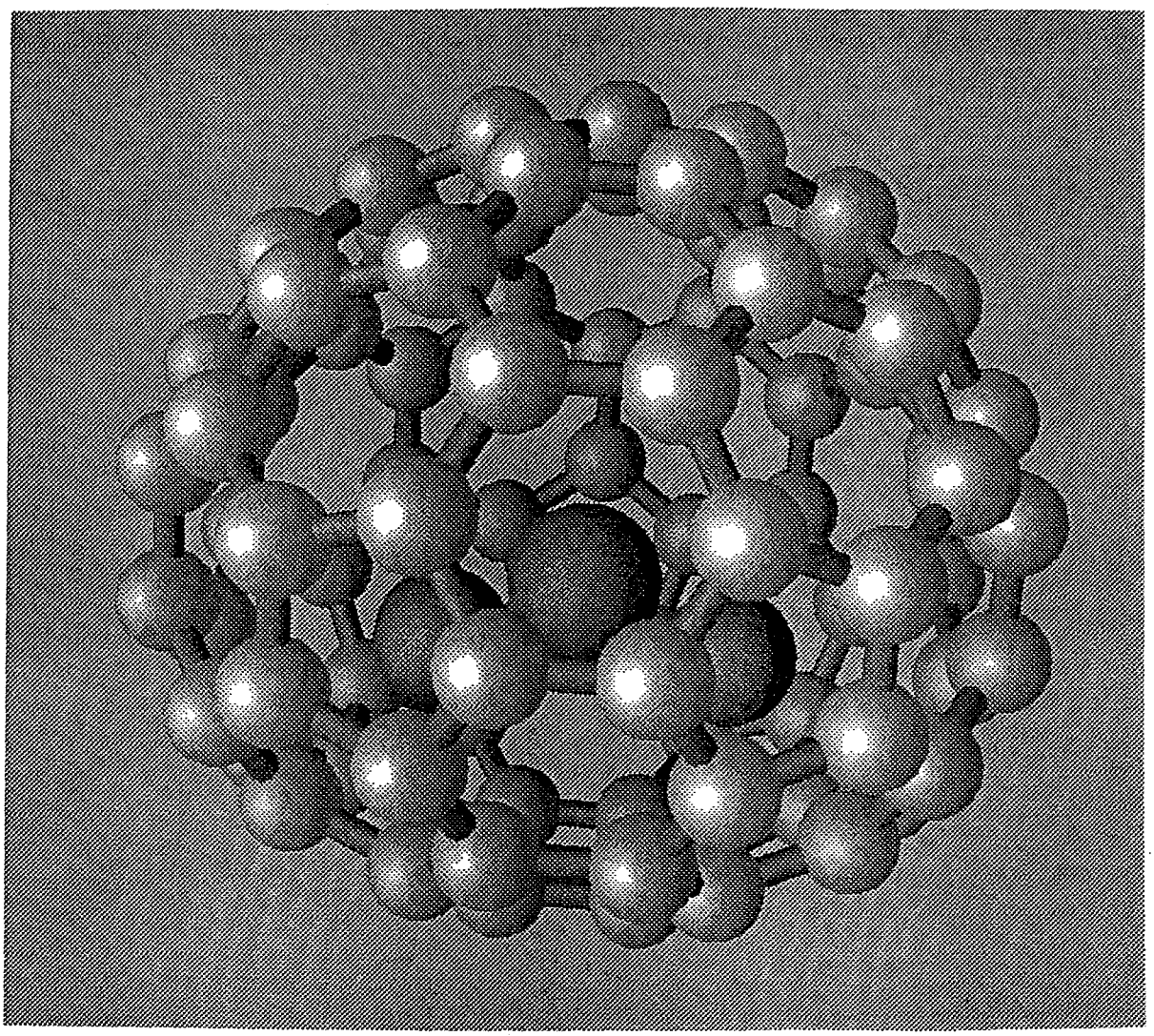

Figure 4.1: Molecular model of $Sc_3@C_{82}$ with C_{3v} symmetry. The structure was constructed assuming that all pentagons are surrounded by hexagons. Among the various possible $Sc_3@C_{82}$ structures that obey the isolated pentagon rule, the structure with C_{3v} symmetry is considered to be the dominate isomer structure [14].

most of the measurements have been done on samples containing a wide variety of fullerenes, which include numerous empty fullerenes as well as various metal clusters in different cages. Techniques used to characterize metallofullerenes have been limited to those which can detect signals from small concentrations (1 to 2%) of metallofullerene in the sample, such as electron paramagnetic resonance (EPR) and mass spectrometry.

Structural information is a key step towards understanding metallofullerenes. It is well accepted that the metallofullerenes which are solvent extractable, such as ScC_{82}, YC_{82}, and LaC_{82}, have metals inside the carbon cage. Indirect data such as EPR electronic property studies and STM images suggest that the metals are inside [7, 20]. Recently, separation and purification techniques for metallofullerenes have been developed by using two stage HPLC [19, 21]. Pure metallofullerenes (> 90%) are now available in milligram quantities. Direct structural characterizations based on crystallographic data, therefore, has become feasible.

In this chapter we discuss the synthesis, purification, and characterization of several metallofullerenes. The metals Sc, Y, La, Gd, and Er were successfully encapsulated in fullerenes. These species were successfully purified by HPLC. The Sc species was crystallized and characterized by high-resolution TEM imaging and electron diffraction.

4.2 Synthesis of Metallofullerenes

We investigated a variety of endohedral metallofullerenes, such as Sc_mC_n, Y_mC_n, La_mC_n, Gd_mC_n, and Er_mC_n. These metallofullerenes were synthesized by vaporizing metal and carbon using an electric arc under a helium atmosphere [2, 10]. The cathode was a graphite rod and the anode was a cored 6 mm diameter polycrystalline graphite rod packed with a mixture of metal or metal oxide and graphite powder. Metal concentrations between 1 and 3 atomic percent (with respect to total carbon)

were used. The arc was generated by a 95 or 105 A DC current kept under 20 to 25 V supply voltage, in a 200 Torr helium. The soot was collected from the chamber walls and was promptly extracted with a CS_2 solvent.

We found that the yield of erbium and gadolinium metallofullerenes was higher than that of scandium and yttrium metallofullerenes. High yield, together with the existence of unfilled *4f* shells in Gd and Er, makes them a good candidate for studies of structural and optical properties.

Purification was accomplished by two stage HPLC [19, 21, 22, 23]. The first stage was a polystyrene column, which provided a coarse separation of the empty fullerenes and metallofullerenes. The second stage used a Buckyclutcher to isolate the different metallofullerenes. The HPLC system was setup to allow automated injection of solution [22, 23] and equipped with both UV and on-line electron paramagnetic resonance (EPR) detection to allow immediate identification of fractions containing EPR active species, *e.g.* MC_n and M_3C_n, where M = Sc or Y [23]. A toluene/decalin (80/20 by volume) mixture with relatively high solubility for fullerenes and metallofullerenes was used as the eluent, allowing large quantities of material (> 10 mg) to be injected into the columns. Coarse separation of metallofullerenes from empty fullerenes was achieved using polystyrene columns. A second HPLC stage using a Buckyclutcher (Regis Chemical Company) column was then used to separate the different metallofullerenes. The dominant scandium metallofullerenes were discandium species with cages of 74, 76, and even numbers of carbons between 80 and 104, with Sc_2C_{84} the most abundant species [22, 23]. Figure 4.2 shows analytical data for the purified Sc_2C_{84}. An HPLC trace for the final fraction containing Sc_2C_{84} is shown in Fig. 4.2a, and the corresponding mass spectrum is shown in Fig. 4.2b. Sc_2C_{84} constitutes $\sim$ 80% of the sample, with Sc_2C_{82} accounting for an additional 10%. The impurity peak near 1110 amu (also $\sim$ 10%) was probably $(Sc_2C)@C_{84}$, $Sc_2C_{84}O$, or ScO_2C_{86}. A number of peaks possibly corresponding to odd-carbon metallofullerenes were found

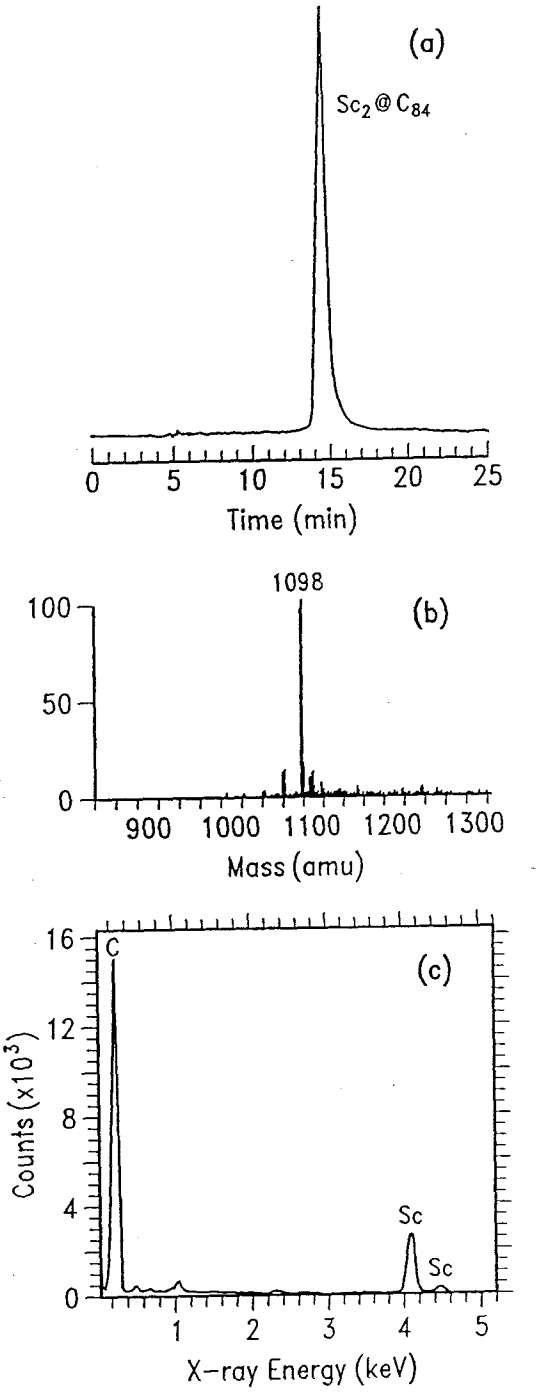

Figure 4.2: (a) HPLC trace for the Sc_2C_{84} fraction obtained using UV detection at 340 nm. (b) Mass spectrum of the Sc_2C_{84} fraction indicating > 80% purity, with roughly 10% each of Sc_2C_{82} and a species tentatively assigned to $Sc_2C@C_{84}$. (c) Energy dispersive spectrum (EDS) taken from a Sc_2C_{84} crystal.

in other HPLC fractions. A second Sc_2C_{84} isomer (confirmed by mass spectrum) was completely resolved by HPLC at a retention time shorter than that for the major Sc_2C_{84} isomer studied here. This second species, together with other species (*e.g.* Sc_3C_{82}), were also purified for further studies.

Various Er metallofullerenes, *e.g.* ErC_{82} and Er_2C_{82}, have been purified in relatively large quantities. Figure 4.3 is the mass spectrum of Er fullerene soot extract. The purity of each Er metallofullerene species is higher than of the Sc, Y, or La metallofullerenes. The optical properties of Er metallofullerenes allow unique experiments not possible with Sc, Y, and La metallofullerenes. A simulated high resolution image and diffraction pattern of Er_2C_{84}, essential to determining the crystal structure, is shown in Fig. 4.3. As more purified endohedral metallofullerenes become available in milligram quantities, serious characterization efforts are feasible.

4.3 Characterization of Metallofullerenes

Crystals were grown by dissolving the Sc_2C_{84} in CS_2 and allowing the solvent to evaporate slowly. These crystals were suspended in ethanol and placed on a holey carbon TEM grid for examination. TEM studies were performed in a Topcon 002B instrument operating at either 100 or 200 KV. The lower voltage was used for high-resolution imaging, since electron beam damage occurred quite rapidly when a 200 KV beam was focussed onto a Sc_2C_{84} crystal. Crystals with sizes ranging from 1 to 20 μm were observed. Elemental analysis of the crystals by energy dispersive X-ray spectroscopy (EDS) showed principally carbon and scandium (Fig. 4.2c). Sulfur (from CS_2) could also be detected in some crystals, but was absent from others ($S/Sc < 0.05$). Electron diffraction patterns from sulfur-free crystals indicate that Sc_2C_{84} crystallized in a *hcp* structure, with lattice parameters $a = 11.2 \pm 0.2$ Å and $c = 18.3 \pm 0.2$ Å, giving a c/a ratio of 1.63.

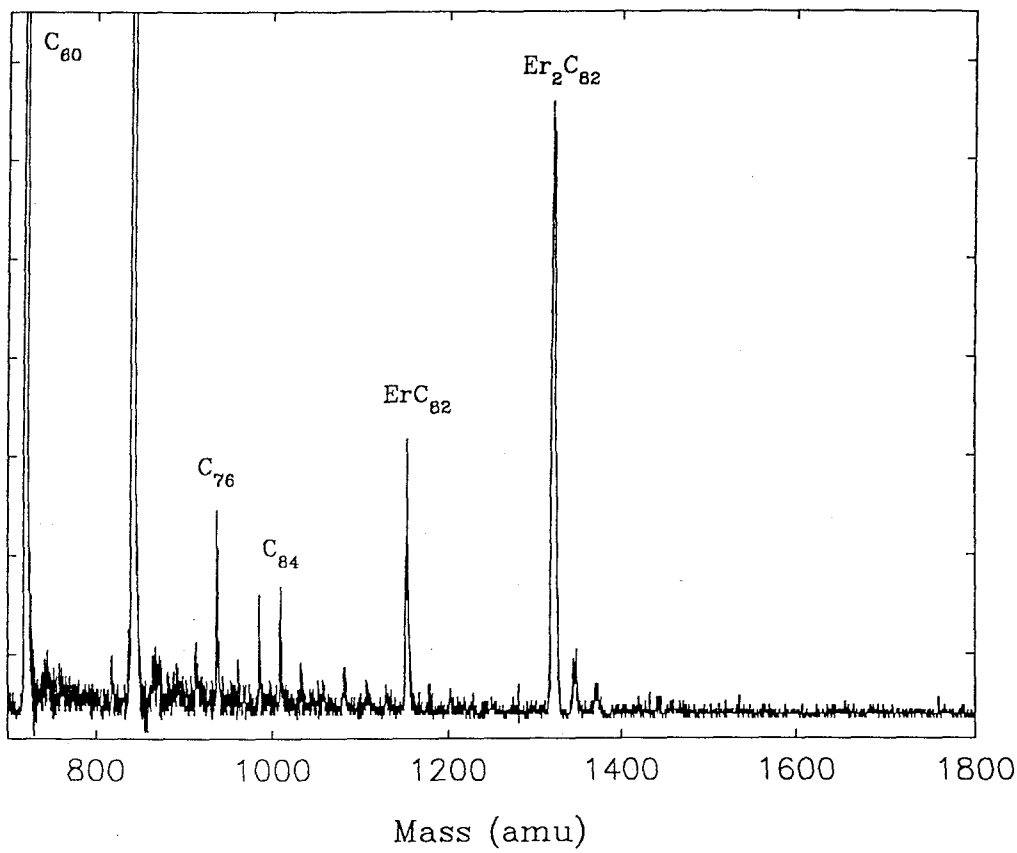

Figure 4.3: Mass spectrum of Er metallofullerene extract.

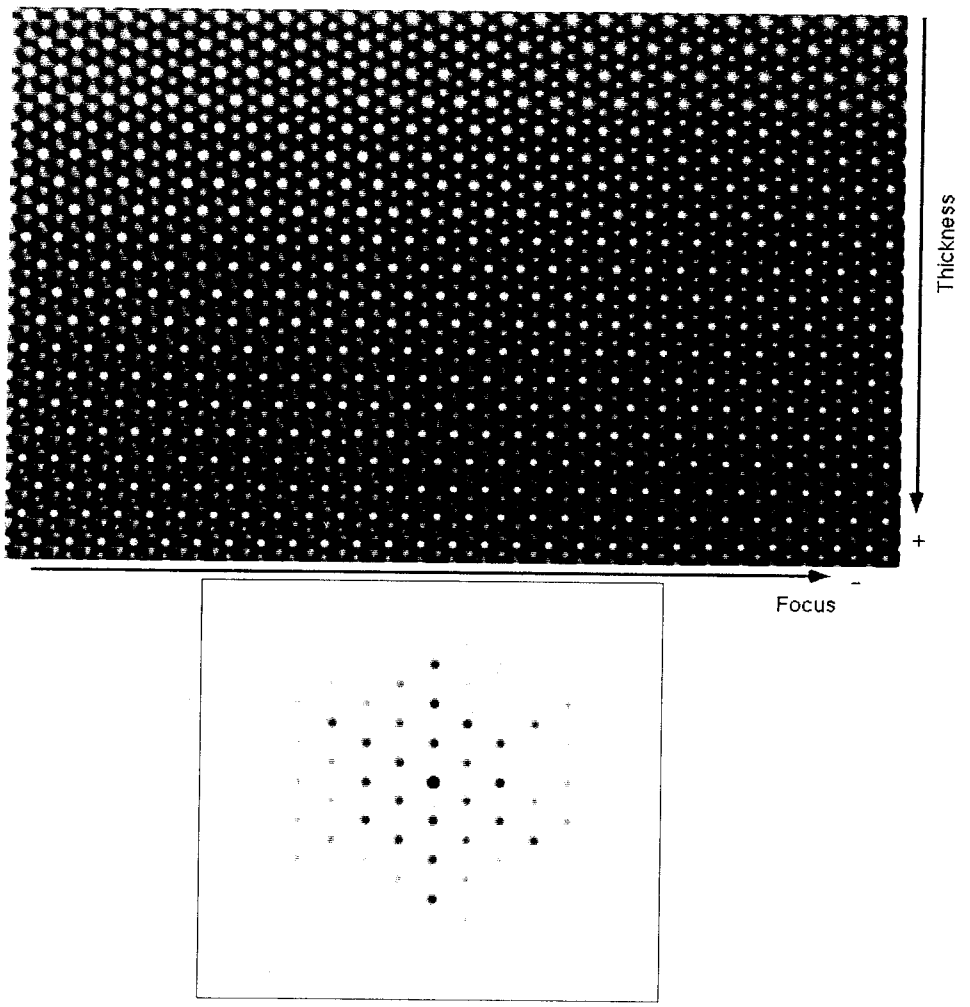

Figure 4.4: Simulated results of a $Er_2@C_{84}$ crystal. Top: Simulated image of a $Er_2@C_{84}$ crystal. The image was simulated under different electron beam focusing condition and on varying thickness of the crystal. Bottom: Simulated diffraction pattern of a $Er_2@C_{84}$ crystal. In both cases, three different orientations of the molecules are superimposed to simulated the orientational disorder present in the crystal at room temperature. The parameters were adopted from the crystal structure of $Sc_2@C_{84}$, as described in the text.

Detailed consideration of high-resolution TEM images and electron diffraction data leads to the conclusion that the scandium atoms in Sc_2C_{84} are inside the carbon cage. The matching intermolecular spacing in Sc_2C_{84} and C_{84} indicates that possible charge transfer to the cage in Sc_2C_{84} does not significantly increase its van der Waals radius. The C_{84} cage diameter (extrapolated from 7.1 Å for C_{60} by assuming equal surface densities of carbon atoms) is estimated to be 8.4 Å. Thus the distance between the carbon cages in crystals of both C_{84} and Sc_2C_{84} is approximately 2.8 Å. This can be compared with the cage spacing of 2.87 Å for C_{60} crystals derived from the ball diameter [27] or the lattice parameter [28] found in earlier studies. The conclusion that the van der Waals radii of Sc_2C_{84} and C_{84} are the same contrasts with the conclusion, drawn from STM studies [20], that $Sc@C_{74}$ and Sc_2C_{74} have larger diameters than would be expected from the diameter of the corresponding empty fullerene cage ($\sim$ 7.9 Å). These authors attributed this anomaly to charge transfer from the metal atoms to the cage.

4.4 Conclusions

Following recent advances in metallofullerene production and purification techniques, metallofullerene crystals can now be made and detailed studies similar to those appearing for the more abundant empty fullerenes are possible. We have synthesized, purified, and characterized several endohedral metallofullerenes. We made Sc_2C_{84} crystals and determined their structure with electron diffraction and high-resolution imaging [29]. Sc_2C_{84} metallofullerenes form an orientationally disordered *hcp* structure with the scandium atoms inside the carbon cages.

References

[1] H. W. Kroto, J. R. Heath, S. C. O'Brien, R. F. Curl, and R. E. Smalley, Nature **318**, 162 (1985).

[2] W. Krätschmer, L. D. Lamb, K. Fostiropolulos, and D. R. Huffman, Nature **347**, 354 (1990).

[3] J. R. Heath, S. C. O'Brien, Q. Zhang, Y. Liu, R. F. Curl, H. W. Kroto, Q. Zhang, F. K. Tittel, and R. E. Smalley, J. Am. Chem. Soc. **107**, 7779 (1985).

[4] Y. Chai, T. Guo, C. Jin, R. E. Haufler, L. P. F. Chibante, J. Fure, J. M. Alford, and R. E. Smalley, J. Phys. Chem. **95**, 7564 (1992).

[5] D. S. Bethune, R. D. Johnson, J. R. Salem, M. S. de Vries, and C. S. Yannoni, Nature **366**, 123 (1993), and references therein.

[6] F. Weiss, J. Elkind, S. O'brien, R. Curl, and R. Smalley, J. Am. Chem. Soc. **110**, 4464 (1988).

[7] C. S. Yannoni, M. Hoinkis, M. S. de Vries, D. S. Bethune, J. R. Salem, M. S. Crowder, and R. D. Johnson, Science **256**, 1191 (1992).

[8] S. Suzuki, S. Kawata, H. Shiromaru, K. Yamauchi, K. Kikuchi, T. Kato, and Y. Achiba, J. Phys. Chem. **96**, 7159 (1992).

[9] J. H. Weaver, Y. Chai, G. H. Kroll, C. Jin, T. R. Ohno, R. E. Haufler, T. Guo, J. M. Alford, J. Conceicao, L. P. F. Chibante, A. Jain, G. Palmer, and R. E. Smalley, Chem. Phys. Lett. **190**, 460 (1992).

[10] R. D. Johnson, M. S. de Vries, J. Salem, D. S. Bethune, and C. S. Yannoni, Nature **355**, 239 (1992).

[11] H. Shinohara, H. Sato, M. Ohkohchi, Y. Ando, T. Kodama, T. Shida, T. Kato, and Y. Saito, Nature **357**, 52 (1992).

[12] S. Bandow, J. Shinohara, Y. Saito, M. Ohkohchi, and Y. Ando, J. Phys. Chem. **97**, 6101 (1993).

[13] S. Hino, H. Takahashi, K. Iwasaki, K. Matsumoto, T. Miyazaki, S. Hasegawa, K. Kikuchi, and Y. Achiba, Phys. Rev. Lett. **71**, 4261 (1993).

[14] J. Shinohara, M. Inakuma, N. Hayashi, H. Sato, Y. Saito, T. Kato, and S. Bandow, J. Phys. Chem. **98**, 8597 (1994).

[15] M. Saunders, H. A. Jiménez-Vázquez, R. J. Cross, S. Mroczkowski, D. I. Freedberg, and F. A. L. Anet, Nature **367**, 256 (1994); M. Saunders, H. A. Jiménez-Vázquez, B. W. Bangerter, R. J. Cross, S. Mroczkowski, D. I. Freedberg, and F. A. L. Anet, J. Am. Chem. Soc. **116**, 3621 (1994).

[16] M. M. Ross and J. H. Callahan, J. Phys. Chem. **95**, 5720 (1991).

[17] T. Weiske and H. Schwarz, Angew. Chem. Int. Ed. Engl. **31**, 605 (1992).

[18] K. Kikuchi, N. Nakahara, R. Wakabayashi, S. Suzuki, H. Shiromaru, Y. Miyake, K. Saito, I. Ikemoto, M. Kainosho, and Y. Achiba, Nature **357**, 142 (1992).

[19] H. Shinohara, H. Yamaguchi, N. Hayashi, H. Sato, M. Ohkohchi, Y. Ando, and Y. Saito, J. Phys. Chem. **97**, 4259 (1993).

[20] X.-D. Wang, Q. K. Xue, T. Hashizume, H. Shinohara, Y. Nishina, and T. Sakurai, Phys. Rev. B **48**, 15492 (1993).

[21] K. Kikuchi, S. Suzuki, Y. Nakao, N. Nakahara, T. Wakabayashi, H. Shiromaru, K. Saito, I. Ikemoto, and Y. Achiba, Chem. Phys. Lett. **216**, 67 (1993).

[22] S. Stevenson, H. C. Dorn, P. Burbank, K. Harich, J. Haynes, C.-H. Kiang, J. R. Salem, M. S. de Vries, P. H. M. van Loosdrecht, R. D. Johnson, C. S. Yannoni, and D. S. Bethune, Anal. Chem. **66**, 2675 (1994);

[23] S. Stevenson, H. C. Dorn, P. Burbank, K. Harich, Z. Sun, C.-H. Kiang, J. R. Salem, M. S. de Vries, P. H. M. van Loosdrecht, R. D. Johnson, C. S. Yannoni, and D. S. Bethune, Anal. Chem. **66**, 2680 (1994).

[24] K. Laasonen, W Andreoni, and M. Parrinello, Science **258**, 1916 (1992).

[25] A. F. Hebard, Nature **350**, 600 (1991).

[26] G. P. Agrawal, *Fiber-Optic Communication Systems*, (John Wiley & Sons, New York, 1993), p. 364; E. Desurvire, Phys. Today **47**, 20 (1994).

[27] C. S. Yannoni, P. P. Bernier, D. S. Bethune, G. Meijer, and J. R. Salem, J. Am. Chem. Soc. **113**, 3190 (1991).

[28] R. M. Fleming, T. Siegrist, P. M. Marsh, B. Hessen, A. R. Kortan, D. W. Murphy, R. C. Haddon, R. Tycko, G. Dabbagh, A. M. Mujsce, M. L. Kaplan, and S. M. Zahurak. Mat. Res. Soc. Proc. **206**, 691 (1991).

[29] R. Beyers, C.-H. Kiang, R. D. Johnson, J. R. Salem, M. S. de Vries, C. S. Yannoni, D. S. Bethune, H. C. Dorn, P. Burbank, K. Harich, and S. Stevenson, *Nature* **370**, 196 (1994).

Chapter 5

Catalytic Synthesis of Carbon Nanotubes and Nanoparticles

5.1 Introduction

The discovery of nested carbon nanotubes by Iijima [1] has stimulated numerous theoretical [2, 3] and experimental studies [4, 5]. We discuss in this chapter one such offshoot, single-shell carbon nanotubes. Our group discovered this material simultaneously with Iijima in 1993 [6, 7]. Our tubes are produced by covaporizing cobalt and graphite powders in a carbon arc under helium [6].

In this chapter, we discuss the effects of varying the production conditions on the synthesis of single-layer nanotubes using a Co catalyst. These studies may provide clues to the growth mechanism and could ultimately help in developing methods for mass-production of nanotubes. We found that nanotubes grew under a wide range of conditions. Nanotubes were produced using various Co sources, Co concentrations, He pressures, and He flow rates.

The growth and properties of single-shell carbon nanotubes under these various

reaction conditions are quantified primarily by electron microscopy (TEM). We produced the nanotubes under a wide range of conditions, with cobalt sources of different chemical character, various percentages of Co in the arc anode, different buffer gas compositions, and various flow rates. The yield of nanotubes is highest with Co concentrations between 2 and 6 atomic percent. The observed nanotubes have diameters ranging from 0.9 to 2.4 nm, with 1.3 nm being the most probable diameter. TEM images show some interesting properties of these nanotubes.

For some applications, such as gas storage and chemical separation, single-layer tubes with diameters larger than 1 nm or with a broad size distribution could be advantageous. We, therefore, discuss the results produced by using various co-catalysts and promoters along with the cobalt catalyst. We found that when sulfur is added as a promoter, nanotubes with diameters ranging from 1 to 6 nm are produced, in contrast to the 1 to 2 nm range obtained using Co alone. We also studied the catalytic properties of bismuth, lead, and tungsten on the synthesis of carbon nanotubes and nanoparticles. We found that when used with cobalt in an electric arc, bismuth and lead increase the yield of nanotubes, forming tubes with diameters lying outside the range produced with cobalt alone. Sulfur, bismuth, and tungsten also catalyze the formation of cobalt encapsulated graphitic polyhedra. The results suggest that the single-layer carbon nanotubes do not nucleate from cobalt crystals, in contrast to the classical growth model of vapor phase grown carbon fibers [8, 9, 10, 11].

Single-layer carbon nanotubes and metal-filled nanoparticles are anticipated to have unique properties that will eventually lead to novel applications [2, 3, 4]. These tubules might be useful, for example, as strengthening fibers in composite materials, casings for metal nanowires, or atomic force microscope tips. Filled with metals or semiconductors, they might provide elements for nanoscale electrical or electronic devices, such as amplifiers, switches, or electrical-mechanical converters. Experimental studies of these materials, however, have been hindered by the lack of samples with

high concentrations of nanotubes and nanoparticles. Metal particles encapsulated in graphitic polyhedra have been produced, but only for certain metals in their carbide form [12, 13] and only in low yields. The catalytic synthesis of nanotubes we discuss in this chapter has the demonstrated potential to control the production of these materials [6, 7].

5.2 Single-Layer Carbon Nanotubes

5.2.1 Cobalt Catalysis

We used an electric arc, similar to that used to generate fullerenes [14], as the vaporization source. Electrodes were prepared by boring 4 mm diameter holes in 6 mm diameter graphite rods and filling them with mixtures of pure powdered metals and graphite. These filled anodes (2 to 4 atomic percent metal) were vaporized with a current of 105 A in 200–500 Torr of He.

When the arc was run with a cobalt containing rod, web-like material formed in the chamber, draping between various surfaces. Figure 5.1 depicts the experimental setup used to produce nanotubes. The soot on the chamber walls had an unusual rubbery character and could be peeled off in long strips (*c.f.* Fig. 5.1), unlike the usually crumbly fullerene soot. The soot and the web material were ferromagnetic. A TEM image of the web-like material (Fig. 5.2a) showed that the web consists of rounded soot particles a few tens of nanometers across, linked together by thin, thread-like fibers. Carbon nanotubes with single-atomic-layer walls and diameters of 1 to 2 nm were ubiquitous within the thread-like carbon fibers. Individual threads could be traced over lengths of micrometers before they were lost. While for the most part the tubules were coated with non-graphitic carbon, bare sections were also evident. A high resolution TEM image (Fig. 5.2b) shows bare sections of nanotube.

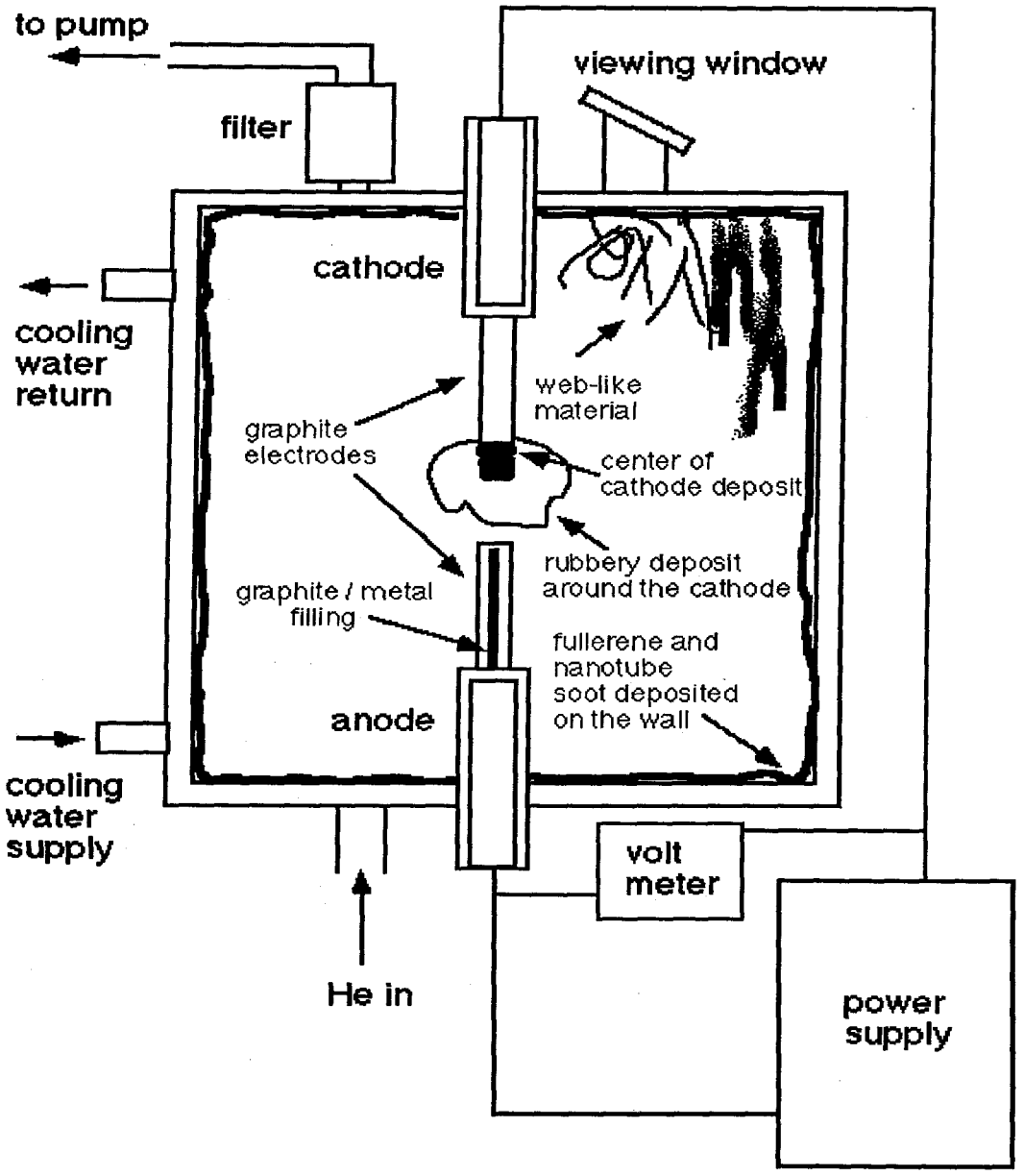

Figure 5.1: A schematic drawing of reaction chamber that was used to produce nanotubes. The soot collected from different parts of the chamber is indicated.

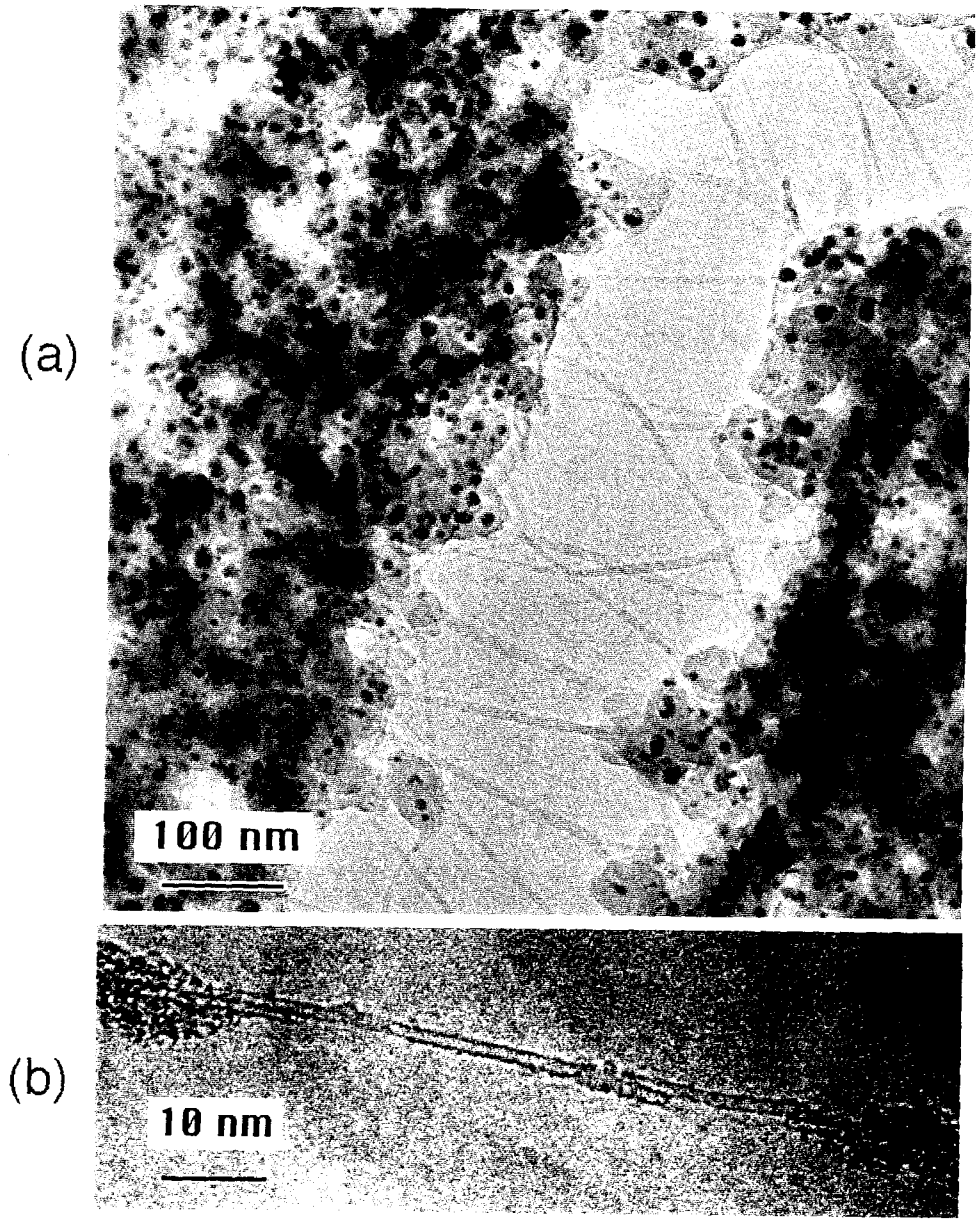

Figure 5.2: (a) Transmission electron micrograph (TEM) of web-like material showing strands of thread-like fibers and cobalt clusters (dark spots) embedded in carbon soot particles. (b) TEM of bare sections of single-layer nanotubes.

The circumference of the nanotubes corresponds to a belt of 15 or 16 edge-sharing hexagons, assuming a 1.42 Å C–C bond length.

In contrast to the multilayered fibers and tubes formed on the cathode tip (see Fig. 5.3), our cobalt catalyzed nanotubes have single-atomic-layer walls and a narrow distribution of diameters (1 to 2 nm). They grow from carbon vapor (with no dissociation of hydrocarbon needed) at He pressures in the range 200–500 Torr. Fullerenes form abundantly at the same time. We believe that cobalt plays an important role in catalyzing the formation of these single-layered tubules, and a specific nucleation process may be responsible for their narrow distribution of diameters.

The nanotubes were found in relatively cold regions of the chamber, co-condensed with fullerene soot. It may be possible to control the amount of carbon that forms on the nanotubes by modifying the growth conditions and the crystallinity of this carbon by post-annealing the coated nanotubes at high temperature. Such measures have been used to modify VGCF [9] and could be important in attempts to use these vapor-grown nanotubes as new types of carbon fibers with superior properties.

5.2.2 Optimizing the Yield

A study of the variation in nanotube yield and physical properties with growth conditions was made both to guide production efforts and to provide data that may help illuminate the mechanism of tube nucleation and growth. Single-layer nanotubes were produced by generating a DC arc (95–115 A at a supply voltage of 20–25 V) between a graphite cathode and an anode containing Co, under a He atmosphere (300–500 Torr with flow rate 0–15 ml/sec). The 6 mm diameter anode was drilled with a 4 mm hole and packed with a mixture of powdered graphite and Co metal or Co compound. The materials produced were examined with a Topcon 002B transmission electron microscope (TEM) operating at 100 or 200 KV with a Gatan Model 679

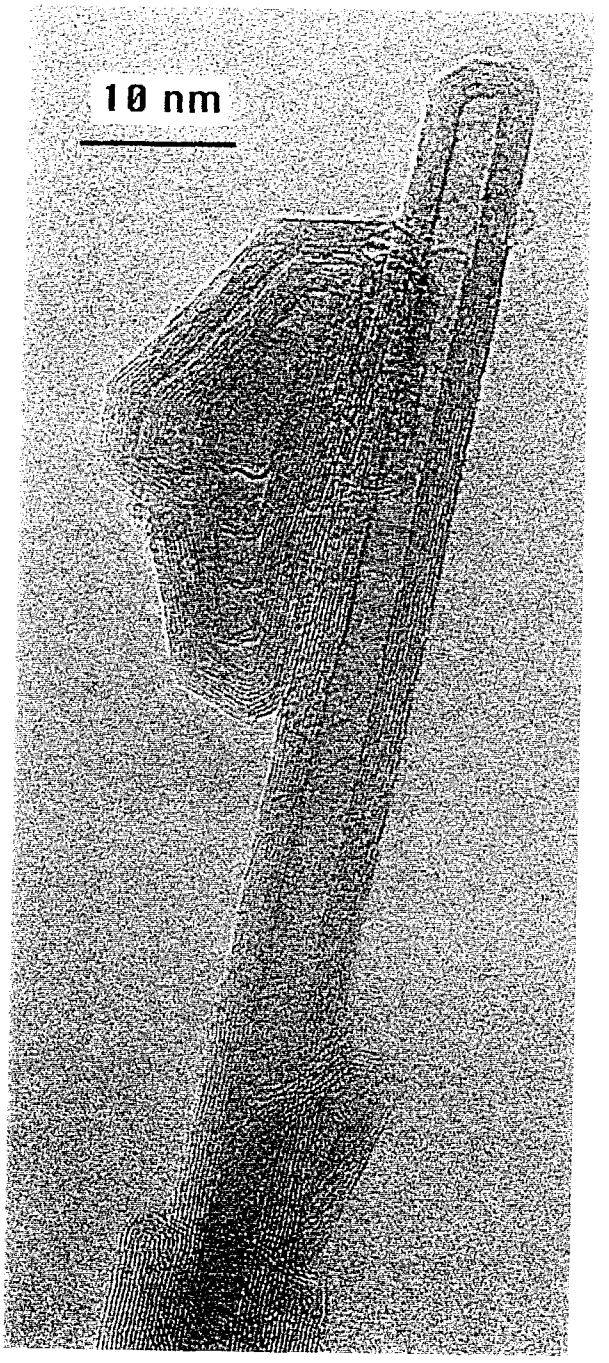

Figure 5.3: TEM of the sample from the central portion of the cathode deposit. Shown in the micrograph is a multilayer carbon nanotube and a graphitic nanopolyhedron. They form on the cathode without using a catalyst.

slow-scan camera. Samples were prepared by sonicating soot in ethyl ether, ethanol, or n-methyl-2-pyrolidinone (NMP) and putting a drop of the suspension onto a holey carbon grid.

We prepared a set of rods containing Co metal in amounts that gave concentrations of 1, 2, 4, 6, 10, and 25 atomic percent (with respect to total carbon, including that in the anode shell). Figures 5.4a to 5.4c illustrate the variation in nanotube production for atomic Co concentrations of 2%, 4%, and 6%. The experiments were carried out under 400 Torr of He with 95 A arc current. Under these conditions, the best production of nanotubes was obtained with a Co concentration of 4% (Fig. 5.4b). The experiments with 1% and 10% Co led to small yields of nanotubes, and very few were observed for 25% Co. Various chemical forms of Co were successfully employed as Co sources, including Co metal and cobalt oxide (CoO, Co_2O_3). For example, using Co_nO_m (99.995%, Aldrich) in the anode (2% Co) and generating the arc under 500 Torr He gave a nanotube yield comparable to that obtained using Co metal under similar conditions. We conclude that metallic crystallites of Co are not required starting materials for the Co species that catalyze tube growth. The small amounts of oxygen introduced by the cobalt oxide does not seem to significantly affect the nanotube production. Production of nanotubes was low for He pressures below 100 Torr, but was abundant for pressures between 200 and 500 Torr (the highest pressure tried). Our observations on the dependence of nanotube production with Co concentration and He pressure are in qualitative agreement with results obtained by Ajayan *et al.* [15]. Tubule production efficiency was not very sensitive to the flow rate of the He buffer gas. Scanning electron microscope (SEM) and TEM observations showed that comparable yields were obtained with a 10 ml/sec flow or with a static fill of He (at 400 Torr with 4% Co anodes).

Since it has been reported that methane was required to produce single-layer nanotubes when using iron as the catalyst [7], a mixture of 20% CH_4 in He at a total

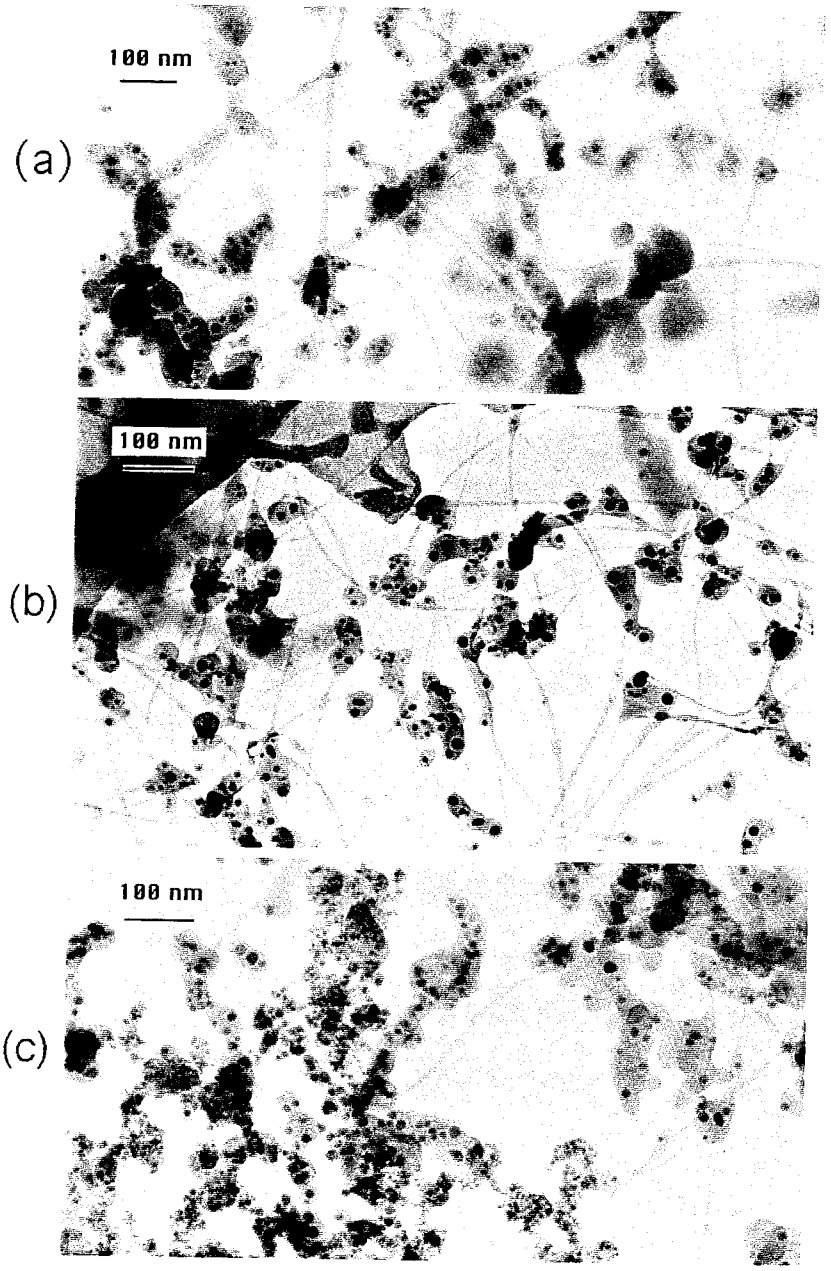

Figure 5.4: TEM image of the soot produced using various concentrations of Co in atomic percentage of (a) 2%, (b) 4%, and (c) 6%. The highest yield under these conditions described in the text is for 4% Co. The threads apparent are individual or bundles of nanotubes. Most of the nanotubes are covered with carbon soot.

pressure of 300 Torr was tried. Under these conditions, most of the carbon reacted to form gaseous products, leaving almost no soot and no nanotubes, in contrast to the earlier work using Fe. No evidence of nanotube formation was found for CH_4 concentrations as low as 5% (in 300 Torr of He). We note that this amount of CH_4, if dissociated, would generate hydrogen at a density comparable to that known to suppress fullerene production [16]. Finally, we note that nanotube production was substantially reduced when Ar was used as the buffer gas rather than He.

Single-layer nanotubes exhibit distinct features not found for multilayer carbon nanotubes. TEM shows that single-layer nanotubes are often severely bent and sometimes form helices or arcs with radii of curvature as small as 20 nm, as shown for example in Fig. 5.5. This image also shows that the nanotubes and nanotube bundles are often coated with non-crystalline carbonaceous material, although bare tubule sections can also be found. They also have a tendency to bundle together. Figure 5.6a shows bundles of nanotubes that bridge a rift introduced after the soot was put onto the TEM grid. The carbon film split, pulling the soot apart but leaving nanotube bridges more than a micrometer long across the gap. This suggests that the single-layer tubes are less fragile than the soot and may possess significant tensile strength. The tubes visible in Fig. 5.6a are also generally covered with carbon and fullerene soot. At higher magnification it was found that there are individual clean nanotubes spanning the gap as well. Figure 5.6b is a high resolution image of a nanotube with 2.4 nm diameter that apparently contains amorphous material inside the tube.

The measured diameter distributions of the nanotubes are roughly the same for all samples produced under the different sets of conditions described above. The histograms of the diameter distributions of nanotubes made using 4% Co from metal and 2% Co from the oxide are shown in Fig. 5.7. The distributions are similar, with peaks around 1.3 nm. These distributions are distinctly different from those reported

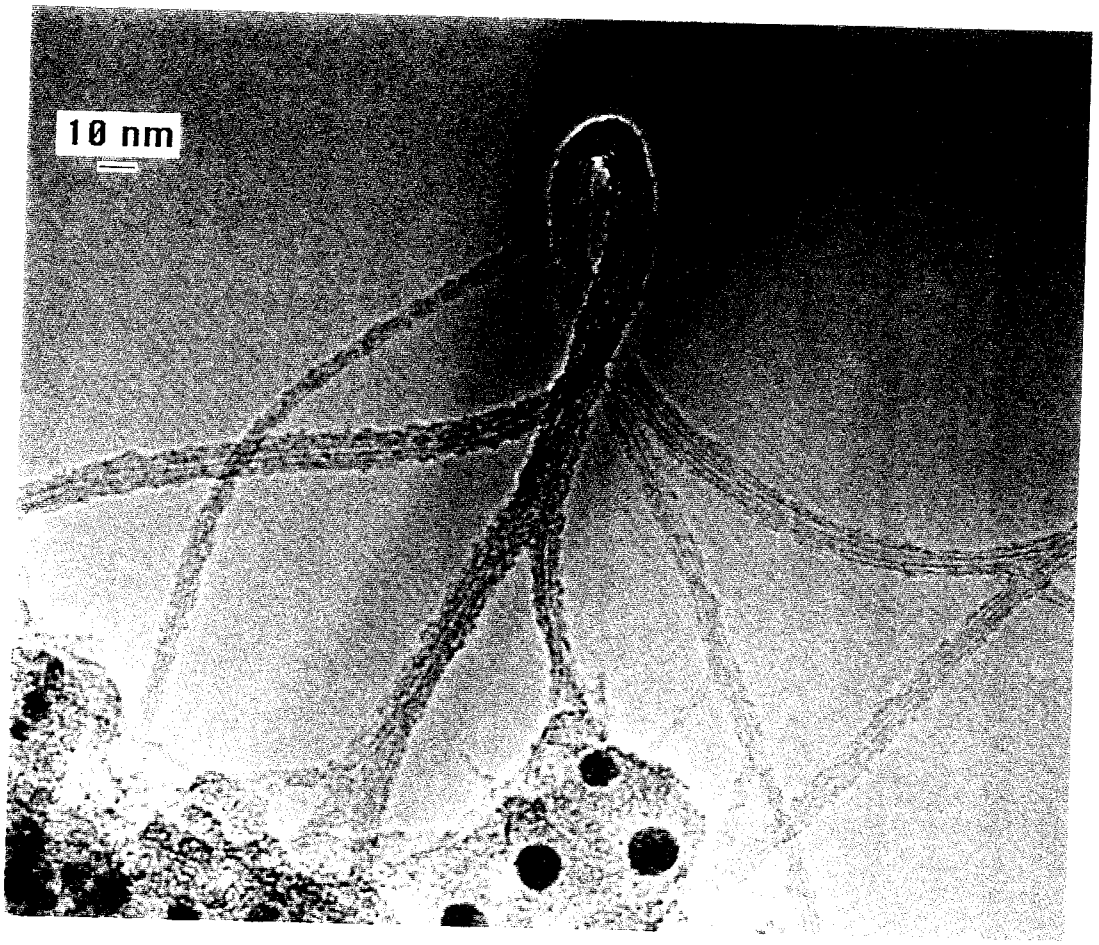

Figure 5.5: TEM image of a bundle of nanotubes with a 20 nm radius of curvature.

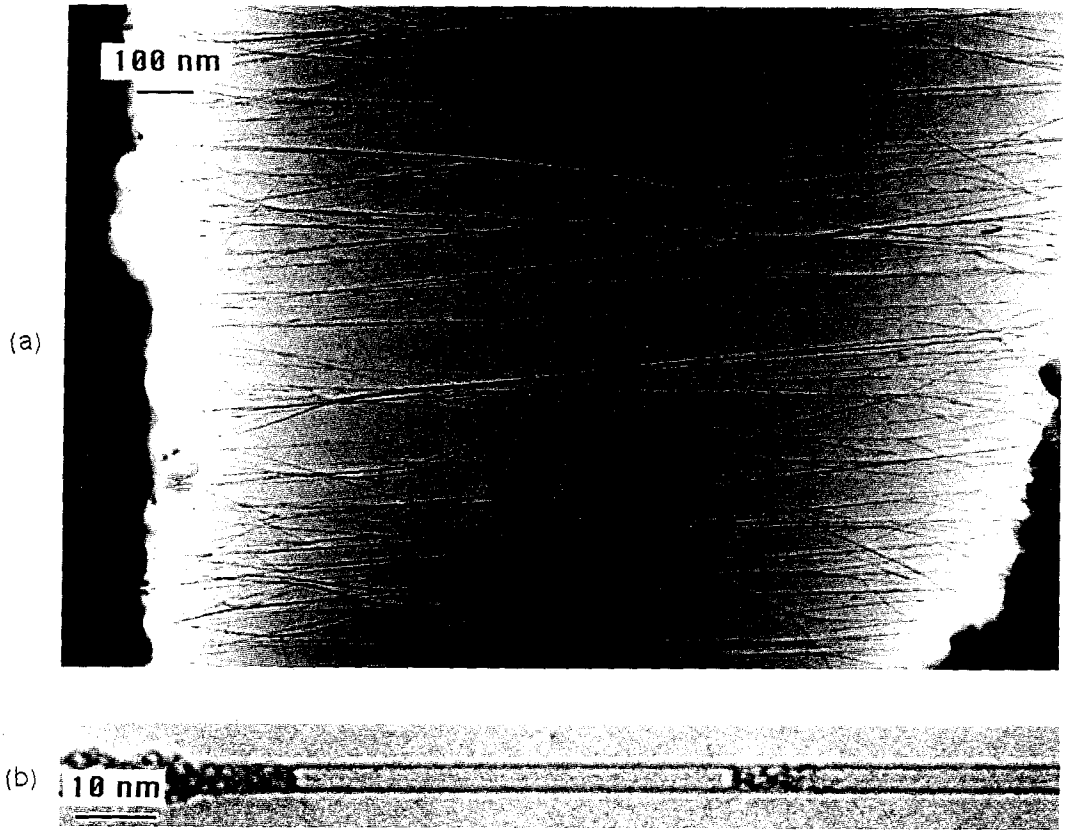

Figure 5.6: (a) TEM of nanotube bridges over a split in the soot deposit. (b) High resolution TEM image of a nanotube containing some amorphous material.

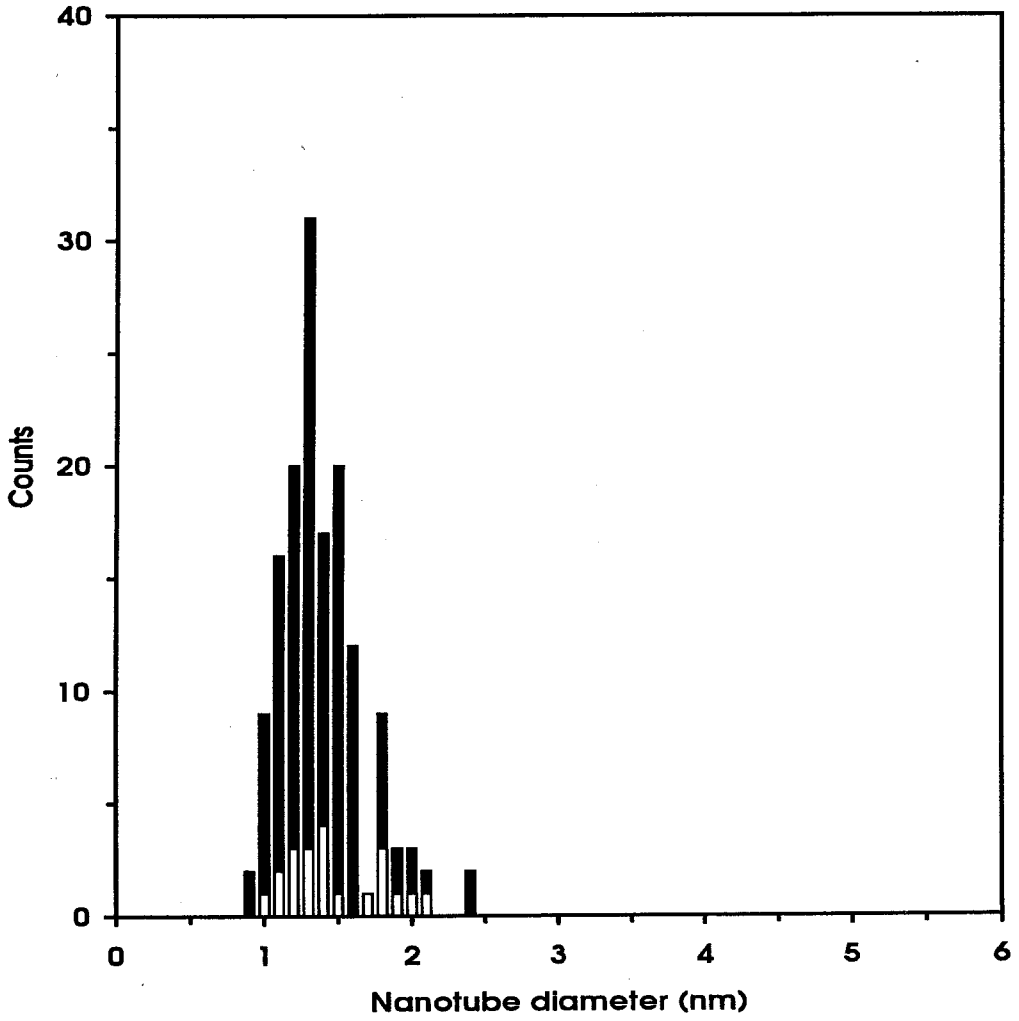

Figure 5.7: Single-layer carbon nanotube diameter distributions for samples made using 4 % Co from Co metal (black bars) and 2 % Co from Co oxide (white bars). All atomic percentages are with respect to the total carbon content of rod. The diameters of the tubes were obtained by measuring the distance between the most intense portions of the TEM image of the tube wall.

in reference [7] for iron catalyzed nanotubes, which have peaks at 0.8 nm and 1.05 nm.

We found that the soot deposited on the chamber wall did not contain multilayer carbon nanotubes. Conversely, we did not observe single-shell nanotubes in the deposits which formed on the cathodes during the runs. The cathode deposits did contain multilayer nanotubes, as found earlier for pure graphite burns [1]. This is consistent with the postulate that single-shell nanotubes nucleate and grow in the gas phase, unlike the multilayer nanotubes that form on the graphite electrode surface [3, 17, 18].

5.2.3 Sulfur Is a Promoter

Sulfur is well known to be a promoter for the transition metal catalysts used to produce vapor-grown carbon fibers (VGCF) [19, 20]. In an effort to increase single-layer nanotube yield, we co-vaporized S, Co, and C in an arc-fullerene generator, using procedures similar to those described previously for cobalt-catalyzed nanotubes [6]. In brief, we used a graphite cathode and a 6 mm diameter graphite anode drilled with a 4 mm diameter hole and filled with a mixture of S, Co, and graphite. Sulfur was incorporated in the form of either cobalt sulfide (CoS, 99.5%) or powdered sulfur, at concentrations of 2 or 4% relative to carbon. The Co concentration was fixed at 4%. The arc current was 95 A DC at 25 V and the He buffer gas pressure was kept between 300–400 Torr. As in the Co experiment, the soot produced was rubbery and web-like material formed inside the chamber.

A typical TEM image of the web-like material (Fig. 5.8) shows fibers consisting of individual and aggregated single-layer nanotubes, and carbonaceous particles with embedded Co clusters. Sulfur enhanced the nanotube growth, as evidenced by an increased fiber-to-particle ratio and by the greater amount of web-like material in

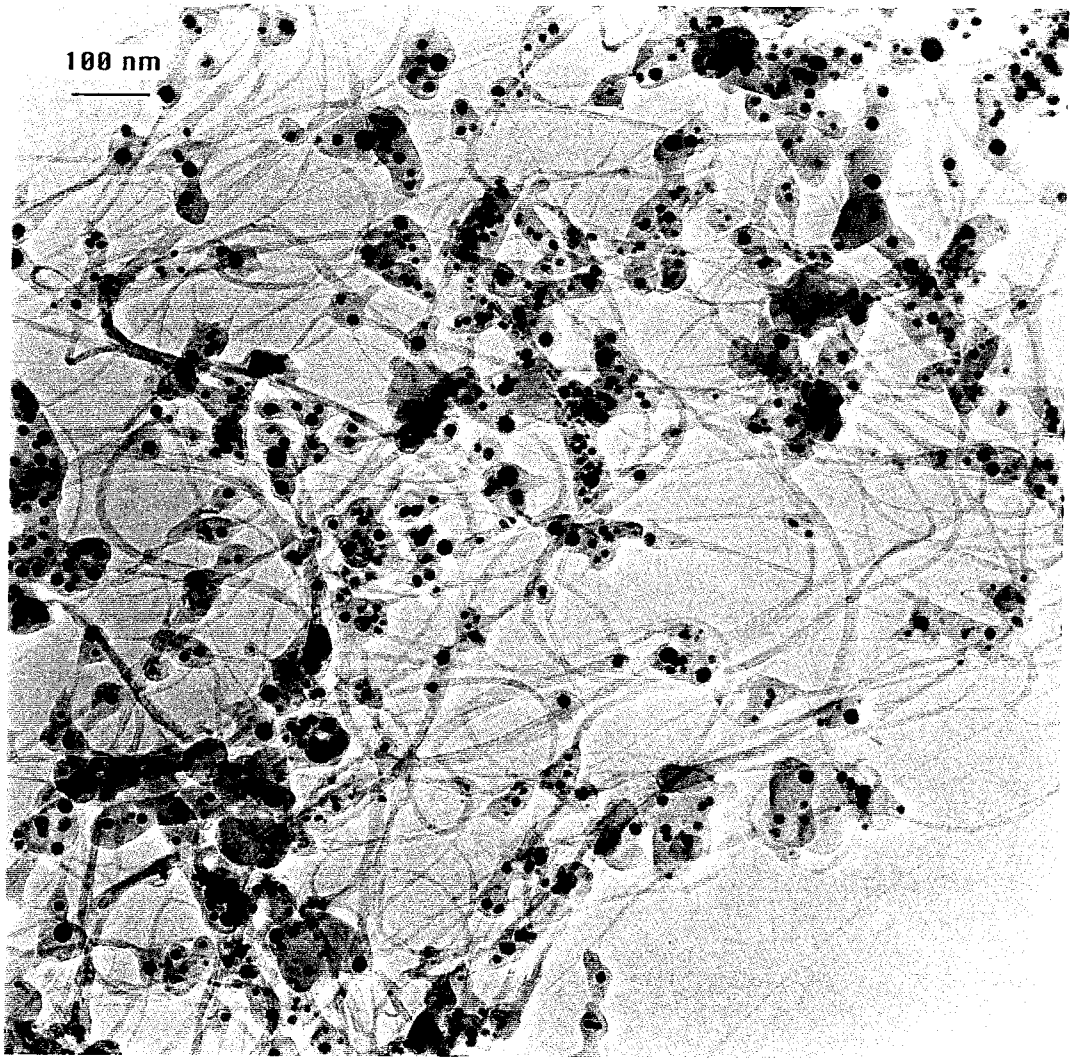

Figure 5.8: Typical low magnification TEM image of single-layer nanotubes in a soot sample made with sulfur promoter. The soot was collected on the chamber walls.

the chamber. We estimate that the relative tube abundance was at least doubled. Electron diffraction patterns of selected nanotubes confirmed the graphene structure of these tubes, and showed that the tubes have various helicities [5, 7]. Interesting topological conformations of the nanotubes were found in the soot. Figure 5.9a, for example, shows a 3.6 nm diameter tube with a 1.3 nm tube spiraling around it. Figure 5.9b shows an example of a nanotube with a double-layer wall, found in the soot away from the electrodes even though almost all of the tubes in this material had single-layer walls. The inner tube diameter is 1.5 nm and the spacing between the two layers is 0.34 nm, comparable to that of bulk graphite. The completeness of the second layer suggests that once nucleated, the growth of additional layers could be rapid.

The sulfur promoter dramatically altered the diameter distribution of the nanotubes. The diameters of carbon nanotubes catalyzed by Co or Fe are between 0.7 and 2.4 nm. In contrast to the pure Co experiment, larger diameter (2–6 nm) single-layer nanotubes form abundantly with the addition of the sulfur promoter. Figure 5.10 is a histogram showing the diameter distribution, obtained by measuring over 330 individual nanotubes using TEM. The diameters of the tubes were obtained by measuring the distance between the most intense portions of the TEM image of the tube wall. The uncertainty in diameter is approximately 0.1 nm for small tubes, and is greater for tubes with diameters larger than 2 nm because they often exhibit radial deformation. The histogram shows an oscillation of the abundance as a function of tube diameter. Groups of peaks occur at roughly one nanometer intervals and within the groups there appears to be a fine structure, with peaks spaced approximately 0.2 nm apart. Prominent peaks occur at 1.3 and 1.5 nm, as was also observed for Co catalyzed nanotubes produced without sulfur [21]. The diameter distribution for nanotubes made with Fe and methane also showed fine structure, with peaks at 0.8 and 1.05 nm [7]. Numerical simulation with Gaussian random numbers suggests that

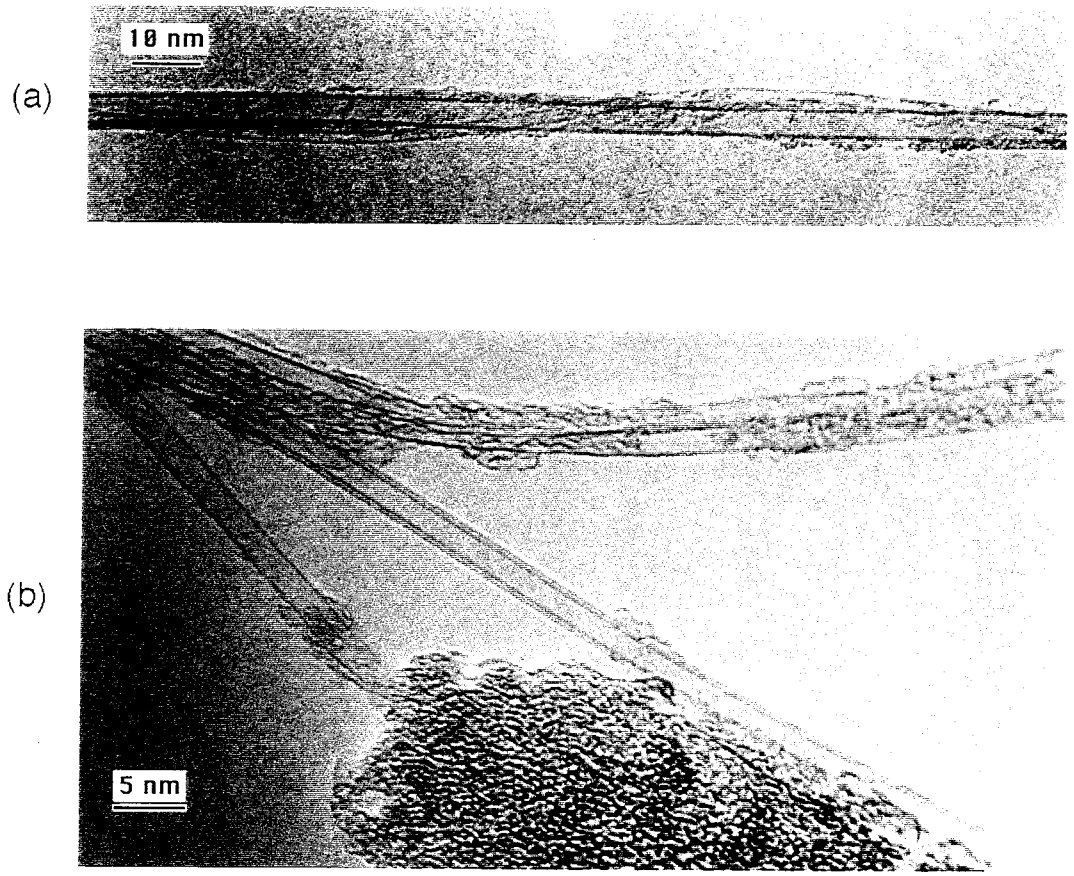

Figure 5.9: (a) High resolution image of a 3.6 nm diameter nanotube with a 1.3 nm tube spiraling around it. (b) Double-layer nanotube among single-layer nanotubes.

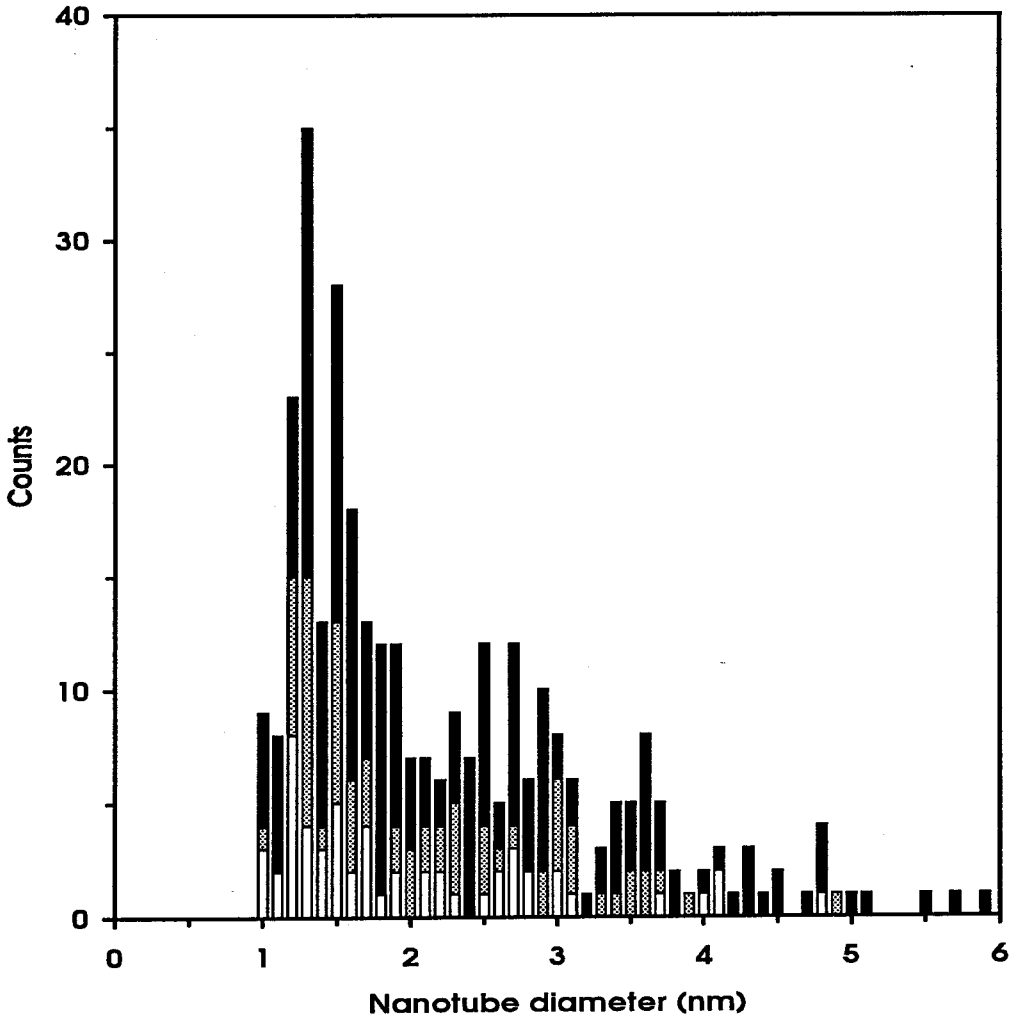

Figure 5.10: Single-layer carbon nanotube diameter distributions for samples made using 4% each S and Co powder (black bars), 4% CoS (grey bars), and 2% S from CoS and 4% Co from 1:1 ratio of Co and CoS (white bars). The uncertainty in diameter is approximately 0.1 nm for small tubes and is greater for tubes with diameters larger than 2 nm because they often exhibit radial deformation.

the fine structure is not due to statistical noise, even for peaks with as few as 50 counts. The fluctuation of the tube abundance versus diameter, therefore, appears to be significant. Examination of the statistical distribution of possible tube diameters (with all helicities equally weighted) reveals no structure that could account for either the fine or coarse features of the observed distribution. Both empirical potential modeling and *ab initio* calculation show that larger diameter tubes have reduced strain energy and, hence, are energetically more favorable [17, 22]. Nanotubes with diameters larger than 3 nm, however, are considerably more rare than are smaller tubes in the data reported here. Such large tubes were not observed in earlier experiments using Co or Fe. That the diameter distribution is structured and depends on the transition metal and the presence of sulfur demonstrates the importance of the catalytic route to the product, underscoring the importance of kinetics rather than energetics.

The role of sulfur in tube growth mechanism is not yet understood. Sulfur was not detected in the nanotubes, and as noted above, the largest peaks at 1.3 and 1.5 nm in the tube diameter distribution are similar whether or not sulfur is present. It has been noted that sulfur-containing species can be effective scavengers of the blocking groups at graphite basal planes [19]. This suggests the possibility that sulfur may affect the kinetics by removing terminating species from growing tube ends. Another possibility is that sulfur could stabilize the growing ends of large diameter tubes.

5.2.4 The Effect of Heavy Metals on Nanotube Synthesis

We were interested in improving the production efficiency of single-layer carbon nanotubes. This lead us to consider various additives that might change the catalytic properties of the primary catalyst. We chose cobalt as the catalyst [6, 21], and Bi and Pb as the additives because they are thought to have exceptional ability to oxidize the

carbon at the nanotube ends [23, 24]. We generated an arc with a DC current under 400 Torr helium and 10–15 ml/min flow rate. The electrodes were 6 mm diameter graphite rods, with the anode cored by a 4 mm cylinder filled in with mixtures of C, Co, and heavy metal (*e.g.* Bi and Pb). The metal concentration was 4% Co and an equal amount (in atomic percent) of heavy metal.

Shortly after the arc started, fine black threads rapidly aggregated to form a web-like material, which filled up the reaction chamber. This is a common phenomenon when nanotubes are grown catalytically in an arc chamber, but the rate of thread formation and the final amount of the web-like material was dramatically enhanced when Bi or Pb was added to the anode. We then sonicated the soot in ethanol and placed a drop of the solution containing the suspended materials on a holey carbon grid for TEM study. The density of nanotubes was very high, and large diameter (> 2 nm) single-layer nanotubes were abundant. Figure 5.11 is a typical TEM image of the soot containing nanotubes, metal particles, fullerenes, and non-crystalline graphite. Bundles consisting of hundreds of single-layer nanotubes were frequently observed, as shown in Fig. 5.12.

It is intriguing that Bi and Pb do not catalyze the nanotube growth when used alone, yet they promote the Co catalytic efficiency. We noticed that the nanotube diameter distribution has been modified, *i.e.* it contains tubes of sizes in the range not accessible without a catalyst promoter [7, 13, 21]. The diameter distributions, each measured by high resolution TEM from over 150 tubes, is shown in Fig. 5.13. The ranges of the nanotube diameters are 1 to 5 nm and 1 to 4 nm, for tubes produced by promoter Bi and Pb, respectively, compared to 1 to 2 nm with Co alone [21]. The histogram indicates that the fine structure (*e.g.* the peaks appearing at around 1.3 and 1.5 nm) is similar to that produced from Co alone. This result suggests that the nucleation process of the nanotubes is independent from the catalytic growth controlled by the promoters.

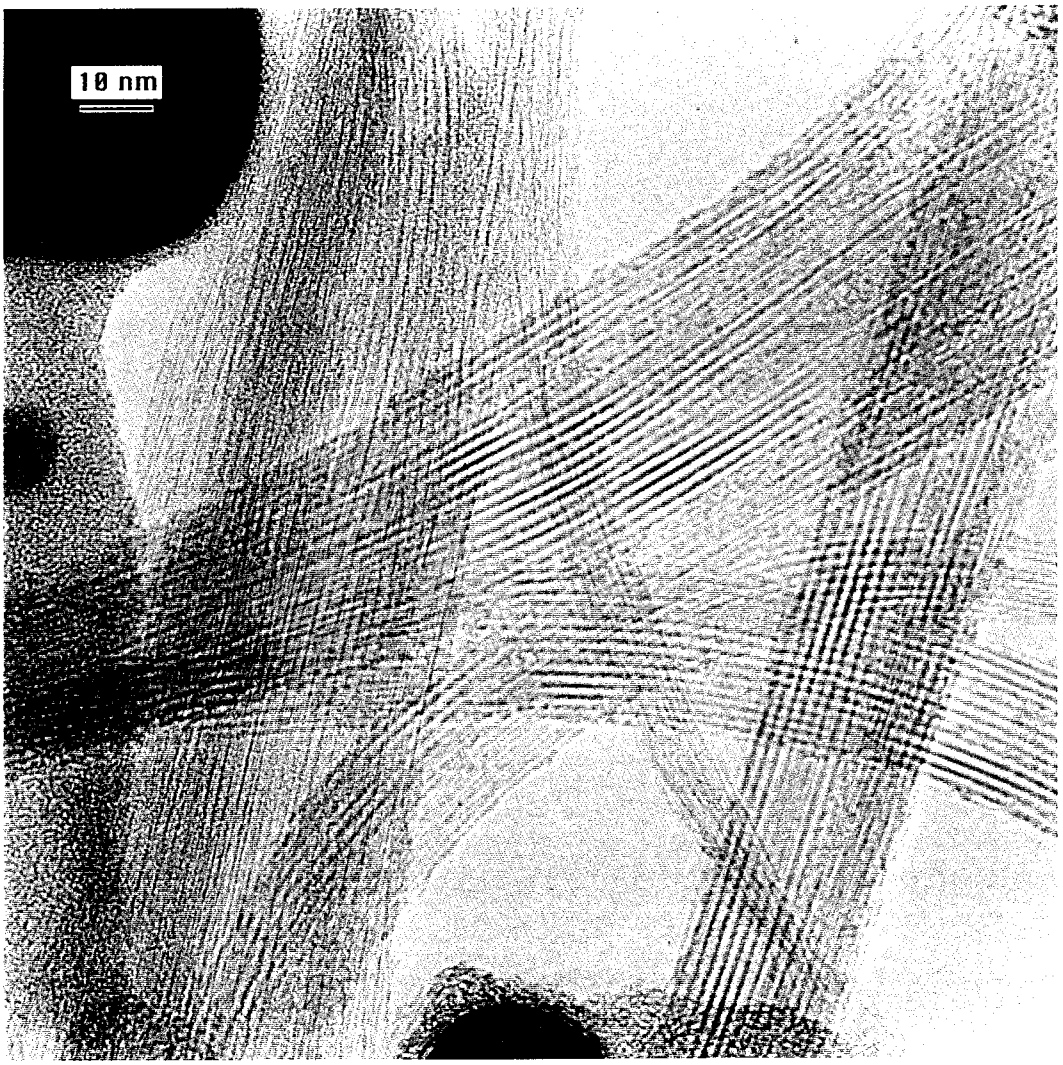

Figure 5.11: TEM of soot produced by vaporizing Co, Bi, and C in an arc. The large dark objects shown in the figure are pure Bi particles. The smaller spots are *fcc* Co crystals, as shown by EDS and high resolution TEM images.

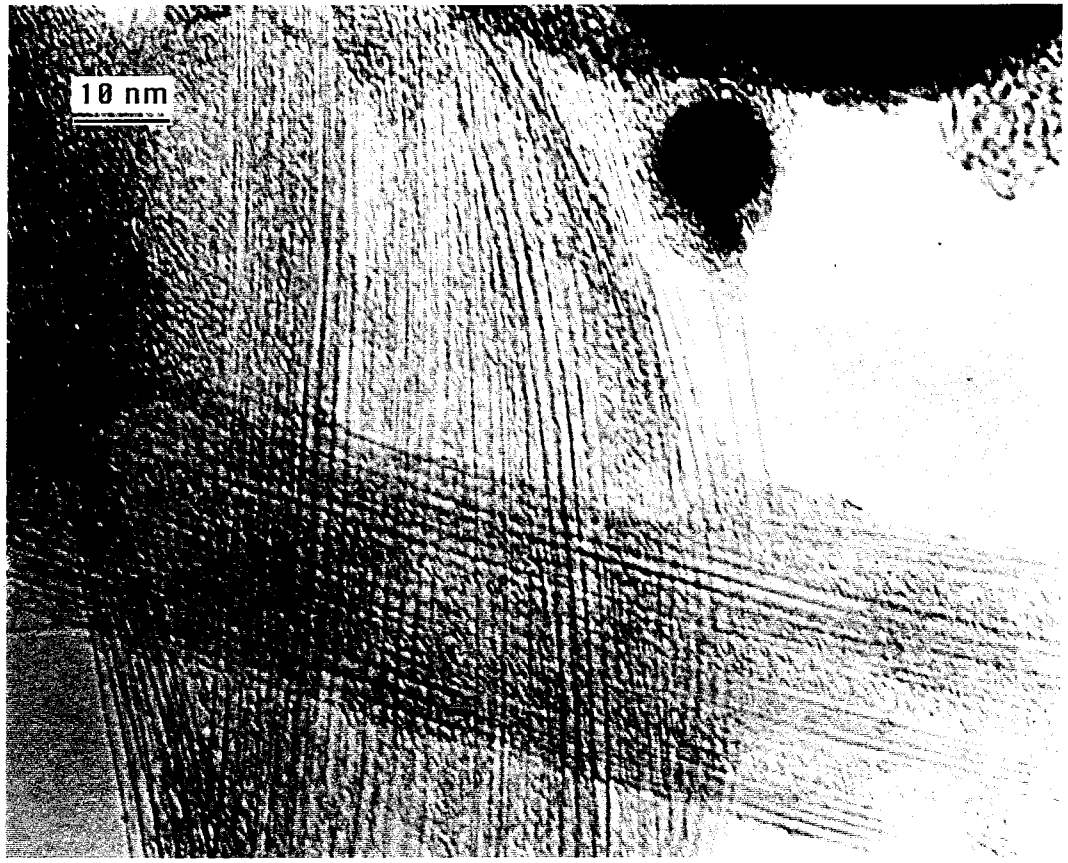

Figure 5.12: Bundles of single-layer carbon nanotubes produced with Co, Bi, and C. The 3 nm diameter tube is larger than any single-layer carbon nanotubes produced to date with Co alone.

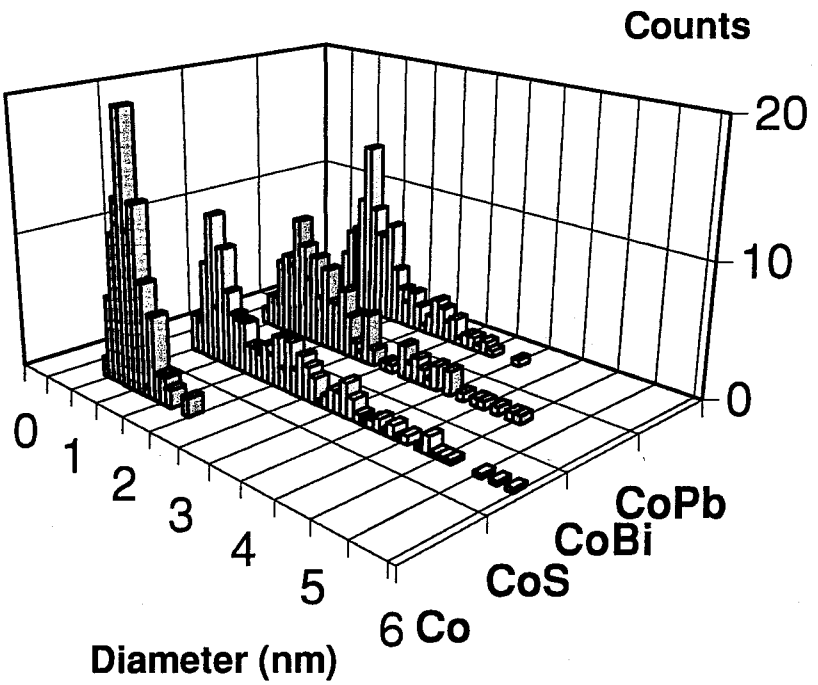

Figure 5.13: Histogram of nanotube diameter distribution of samples made from catalyst Co, Co+S, Co+Bi, and Co+Pb. The numbers of tube diameters measured were more than 150 for Co, 300 for Co+S, 150 Co+Bi, and 200 for Co+Pb. There is a 10 % uncertainty in the measured diameters.

These observations motivated us to study further the influence of heavy metals on the growth of various carbon structures in the arc. We selected Xe for its chemical inertness and its similarity in physical size to Bi and Pb. When we used Xe:He = 1:2 as the buffer gas, the arc was unstable, and the formation of nanotubes was critically reduced. Another heavy metal, W, was tried and found to reduce the nanotube yield. Platinum was found to increase the nanotube yield [25], but with nanotube diameters only in the range 1 to 2 nm, similar to that of W. Recall we have demonstrated that these effects are not particular to heavy metals. A non-metal element, sulfur also enhances the growth of nanotubes. It seems clear that the chemical, rather than physical, properties of these elements are responsible for the observed growth of nanotubes.

5.3 Encapsulated Cobalt Metal Nanoparticles

Embedded within the soot particles were round cobalt clusters with diameters ranging from 1 to 50 nm. Both electron and X-ray diffraction patterns showed that these clusters were face-centered-cubic (*fcc*) cobalt (Fig. 5.14). This indicates that the clusters were rapidly quenched, since cobalt is normally hexagonal-close-packed (*hcp*) below 690K. Scanning electron microscopy (SEM) images show that the rubbery soot deposits from the chamber walls contain thin fibers and soot particles similar to those in the web material, but with the particles in greater relative abundance. The cobalt particle sizes produced with sulfur, typically between 1 nm and 20 nm, are similar to those obtained without sulfur. Powder X-ray diffraction data show that these clusters are predominantly *fcc*-Co crystallites (Fig. 5.14b). The carbon around the cobalt clusters consists partly of fullerenes, which can be extracted from the soot using toluene. Laser-desorption/laser-ionization mass spectrometry of the raw soot showed a CoC_{60} peak. This species, however, was not found in a toluene extract of

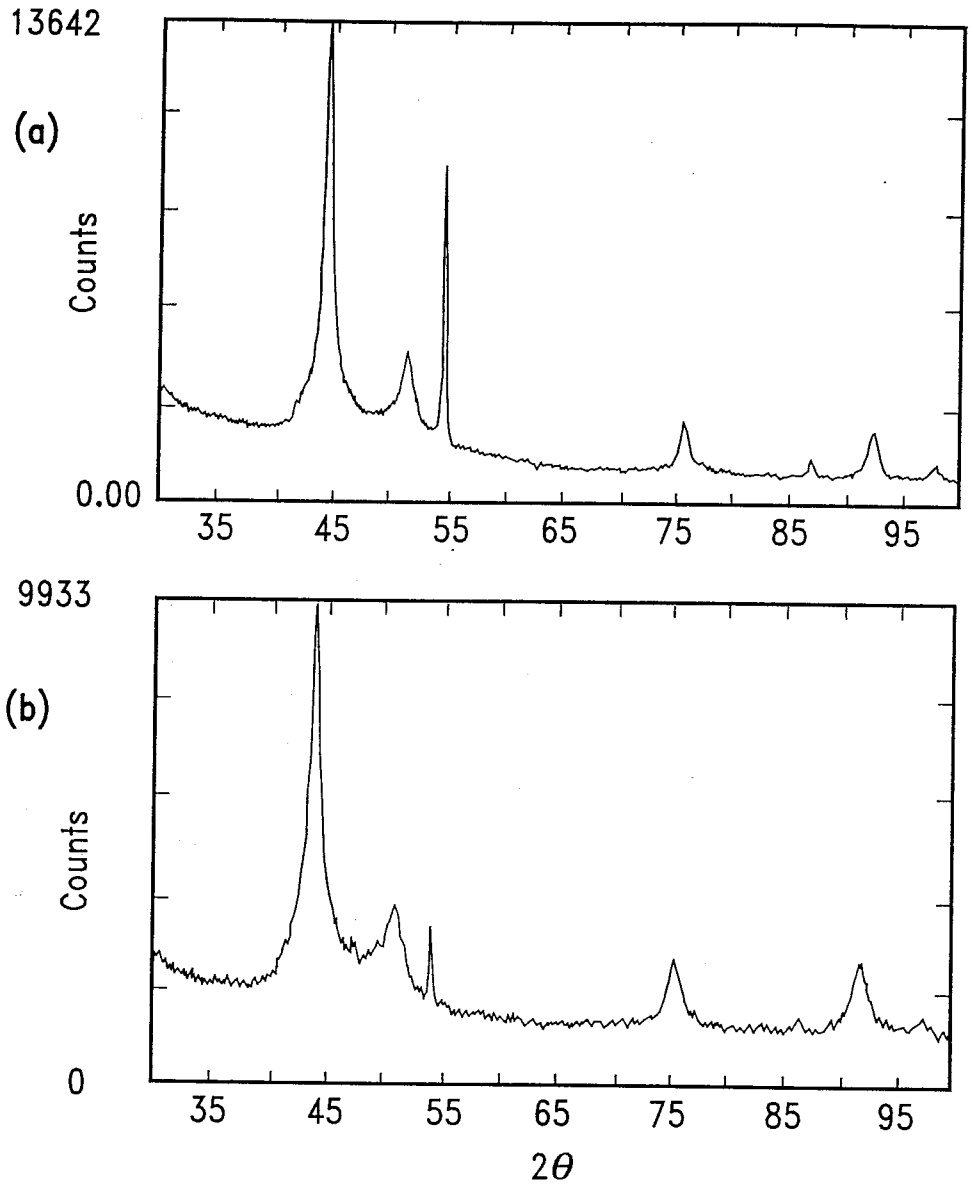

Figure 5.14: X-Ray powder diffraction spectra of (a) soot made with Co and (b) soot made with Co and S. The peak at $2\theta = 45^\circ$ is due to graphitic carbon structure. In both spectra, only the *fcc* phase of Co was detected.

the soot (Fig. 5.15).

These cobalt clusters produced in this process are of substantial interest. When sulfur was incorporated in the reaction, many of the clusters are encapsulated in graphitic polyhedra, as shown in Fig. 5.16. Energy dispersive X-ray spectra (EDS) on selected crystallites indicate Co and C compositions, with very few crystallites containing S. These encapsulated particles are similar in structure to the encapsulated carbide crystallites found earlier in cathode deposits [4, 26] but are here distributed throughout the soot. Such graphite-encapsulated ferromagnetic clusters could be of value in applications such as ferrofluids and data storage, since the graphitic layers chemically and magnetically isolate the magnetic nanoparticles [27, 28]. Significantly, the particles are of a size that they can each be a single magnetic domain. These encapsulated clusters, found throughout the soot rather than only in the cathode deposit, can presumably be synthesized in large quantities. This approach may facilitate investigations of their material properties, identification of their growth mechanisms, and eventual assessment of their utility.

We have also investigated the catalytic properties of Bi, Pb, and W on the formation of metal-filled graphitic polyhedra. High resolution TEM images show that most of the Co particles are wrapped in layers of graphene sheets. Figure 5.17 is a typical image of the metal particles produced in the soot made using Co and Bi. Lead does not seem to have a noticeable effect on the metal particle formation. W results in the encapsulation of Co in graphitic polyhedra, as shown in Fig. 5.18. Previous studies that used an arc to vaporize metal and carbon produced only metal carbide crystallites (*e.g.* LaC_2 and YC_2) encased in graphitic polyhedra [4, 12, 26]. Here, with the aid of S, Bi, or W, *fcc*-Co crystallites tightly wrapped in graphitic polyhedra are produced catalytically and in good yields.

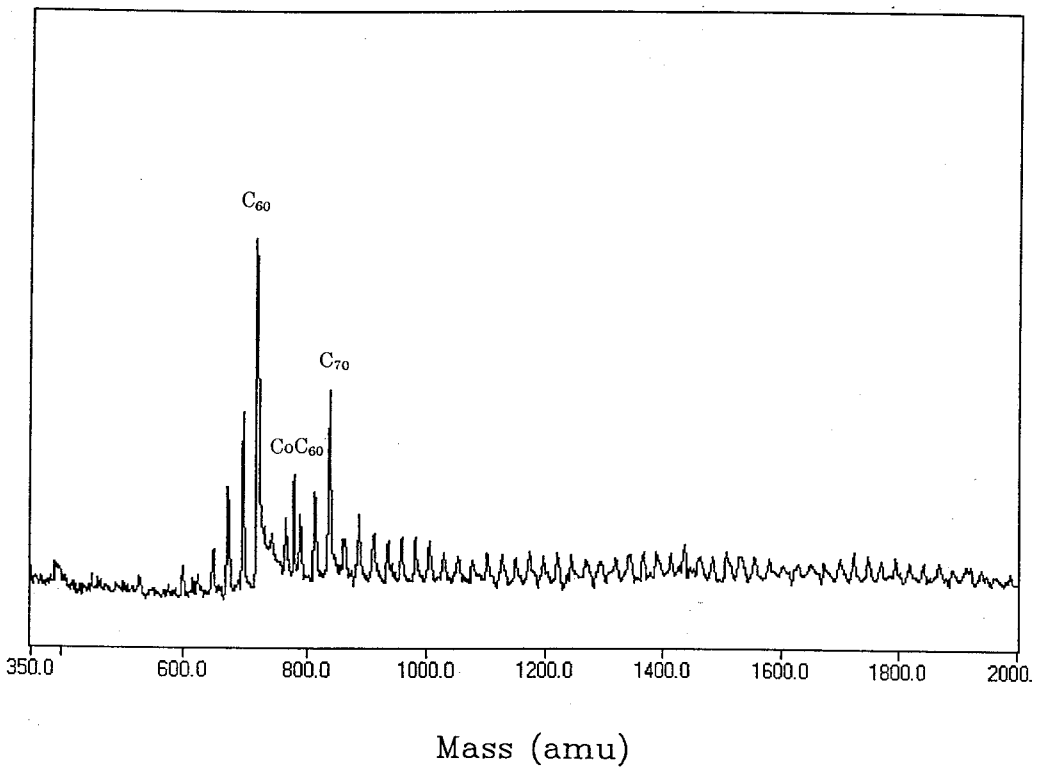

Figure 5.15: Mass spectrum of soot containing nanotubes made with cobalt catalyst.

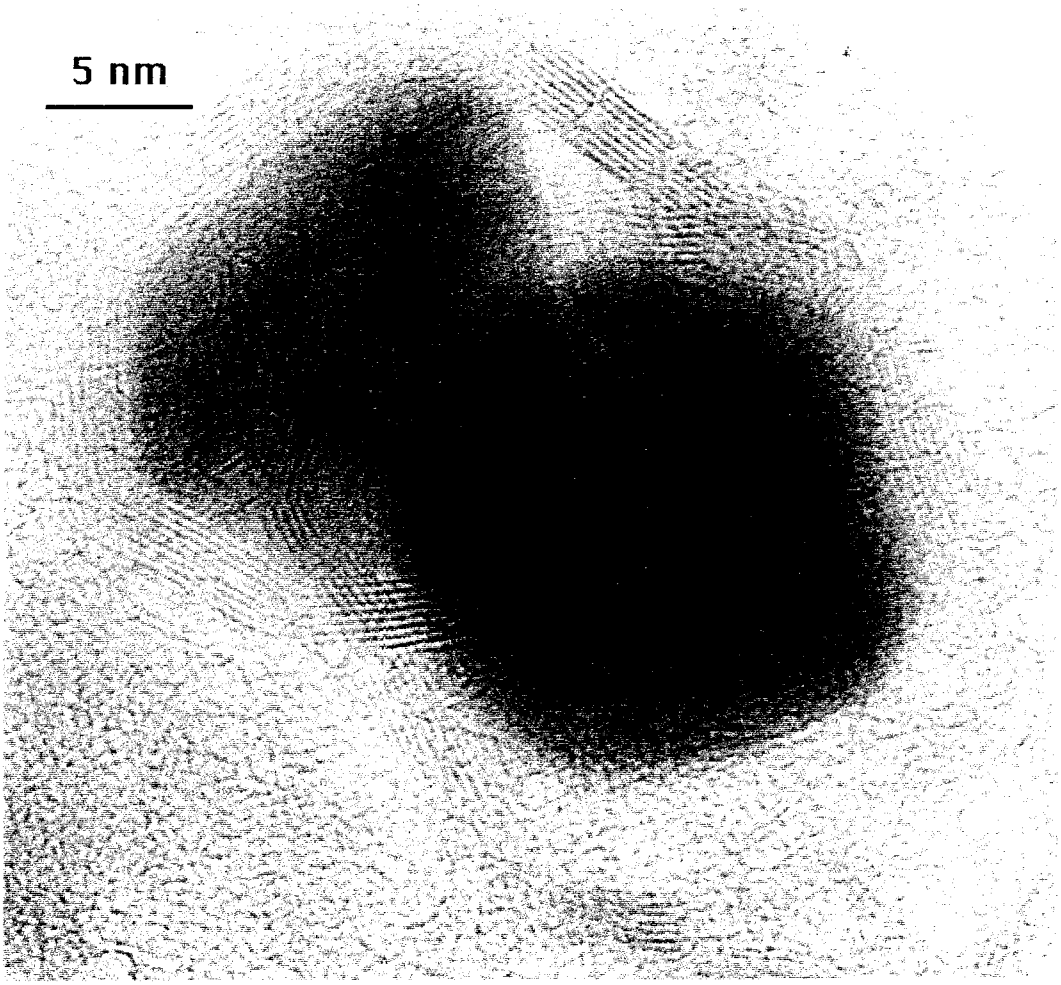

Figure 5.16: TEM image of cobalt particles encapsulated in graphitic polyhedra found in the soot away from the electrodes. The soot was produced with Co catalyst and S promoter.

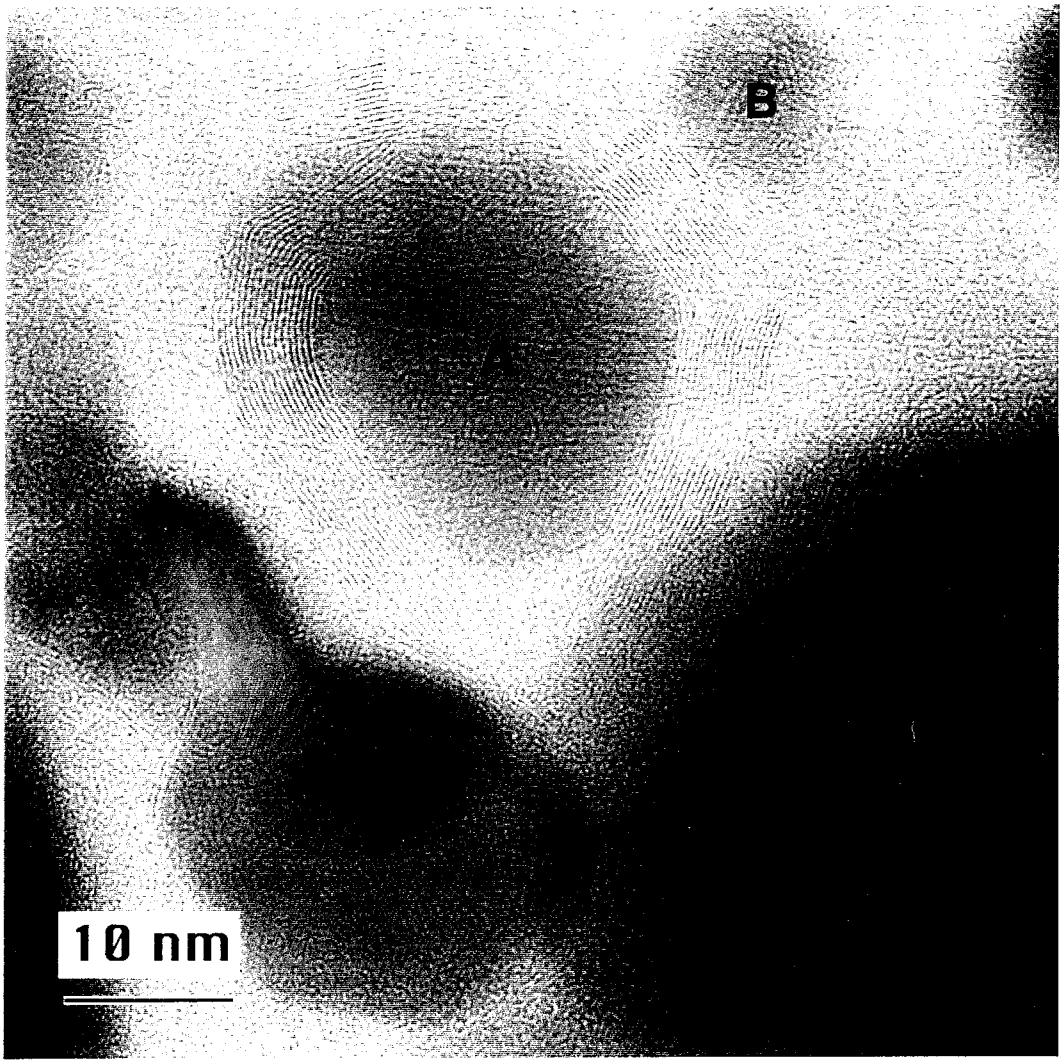

Figure 5.17: Co crystallites encapsulated in graphitic polyhedra, produced with Co and Bi. The crystallite marked A is a 20 nm diameter *fcc*-Co crystallite encapsulated in 17 layers of graphene sheets, which have a constant spacing comparable to that of bulk graphite. The particles marked B, C, and D are also *fcc*-Co crystallites, similar to those produce without Bi, and the particle marked E is a pure Bi particle.

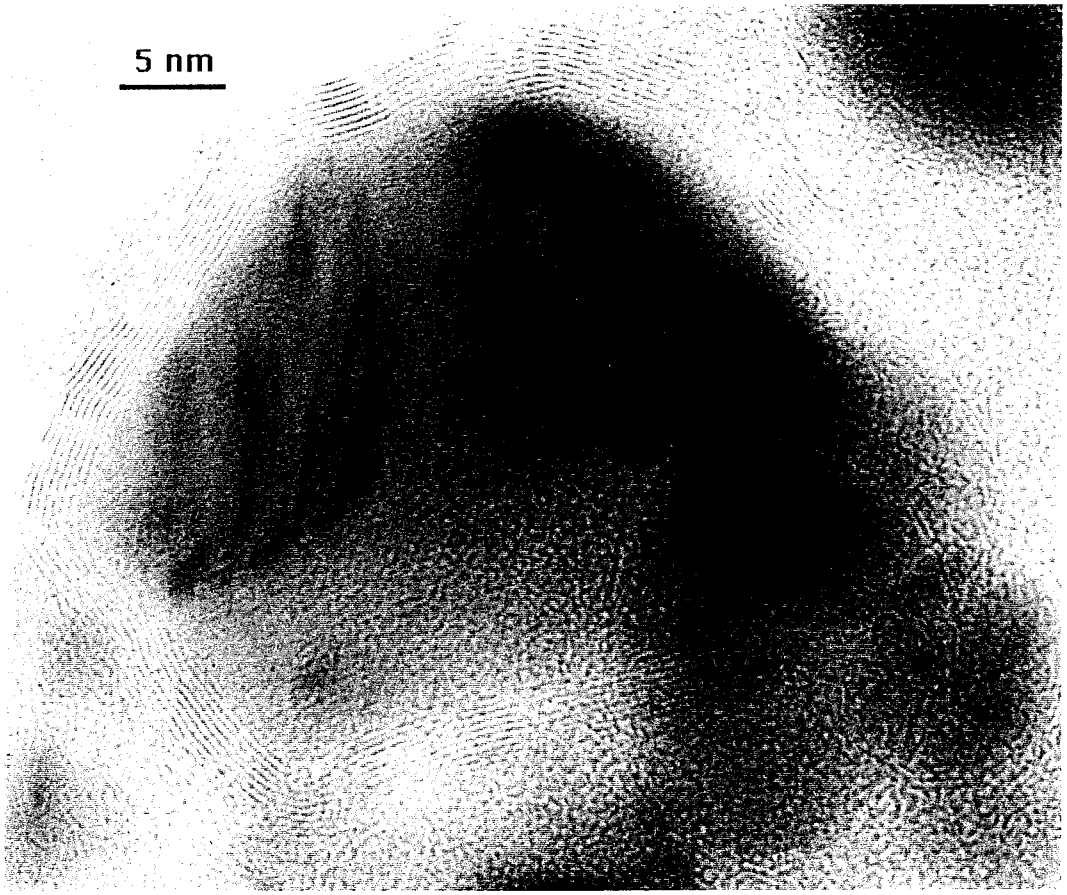

Figure 5.18: Co crystallites encapsulated in a graphitic polyhedron, produced with Co and W. There are two crystallites encased in the nanopolyhedron.

5.4 Comparison with Results from other Groups

We here review results from other groups that were stimulated by Iijima's and our discovery of single-layer nanotubes in 1993.

An electric arc is almost always used to produce single-layer carbon nanotubes. Typically the cathode is a graphite rod, the anode is composed of graphite powder mixed with Fe, Co, or Ni [6, 7, 13, 21, 29, 30]. A He buffer gas is usually employed. The arc is typically generated with a DC current of 50–200 A, supply voltage 20–30 V, electrode diameters between 5 and 20 mm, and buffer gas pressure of 50–600 Torr at a 5–15 ml/min flow rate. The anode is a hollowed out graphite rod packed with a mixture of a metal and powdered graphite. In addition to the pure form of metals, mixtures of these metals [13] and metal compounds (oxides, carbides and sulfides) [21] have been successfully used as source materials. The amount of metal with respect to graphite is set to be a few atomic percent.

The tubes formed with lanthanide catalysts such as Gd, and Y are relatively short and grow radially from the surface of 10–100 nm diameter particles of metal carbide [13, 31]. These tubules have diameters of 1 to 2 nm, similar to the longer tubules produced by the iron group metals, but have lengths of only 10 to 100 nm. These structures have been found in the primary soot, suggesting that they form in the gas phase. Similar structures reported for the case of Ni, however, were found in the rubbery blanket surrounding the cathode [32, 33]. In that case, the nanotubes radiated out from metal particles, identified by electron diffraction to be crystalline *fcc*-Ni or Ni_3C. The Ni-containing particles were typically encased in several graphitic carbon layers, and the free ends of the short, radial single-layered tubes were generally observed to be capped.

When Cu was present in the anode, single-layer nanotubes formed in the center region of the cathode deposit [34]. These tubes had lengths of a few tens of

nanometer and diameters of 1–4 nm. Unlike tubes produced using iron group metals or lanthanides, these nanotubes usually had irregular shapes, with diameters varying markedly along the tube axes, indicating that the nanotube structures contained relatively large amounts of pentagonal and heptagonal defects. The tubes were not found to be associated with Cu-containing particles, although Cu crystals wrapped in graphitic polyhedra were observed.

Endo's group has demonstrated growth of single-layer tubules without a catalyst [35]. Carbon nanofibers were deposited on a graphite substrate by pyrolysis a hydrogen/benzene mixture in a gas phase flow-reactor at 1000 ° C.

5.5 Conclusions

In summary, we discovered single-layer carbon nanotubes simultaneously with Iijima in 1993. In this chapter, we detailed the systematic experiments that varied experimental conditions, such as the chemical character and percentage of Co in the rod, the buffer gas pressure, composition, and flow rate. With cobalt oxide in place of Co, comparable amounts of nanotubes were produced with similar diameter distributions. We found that the yield of nanotubes was best between 2–6 atomic percent Co under our conditions. Buffer gas pressures between 200 and 500 Torr (static or with slow flow) could be used to produce nanotubes. On the other hand, the presence of a small amount of hydrogen in the chamber suppressed the formation of nanotubes.

We also found that sulfur, bismuth, and lead promote nanotube production and extend the diameter distribution of single-layer carbon nanotubes out to 6 nm. The diameter distribution shows structure that may provide clues to the nucleation and growth mechanisms of these single-layer nanotubes.

It may be possible to isolate bulk quantities of bare, single-layer nanotubes. Such structures would be a new type of all-carbon polymer. Theoretical calculations predict

that they can be metallic or semiconducting, depending on their helical pitch [22, 36]. They might draw species into their interiors by capillary action, and they may be useful as catalytic containers, nanowires and solenoids [2]. The recent success in filling nanotubes with lead supports some of these ideas [23, 37, 38]. The availability of the single-layer carbon nanotubes described in this chapter is a necessary first step to characterizing such structures and understanding their properties.

The discovery of catalyst promoters provides a key to mass production of single-layer carbon nanotubes and metal encapsulated graphitic polyhedra. Nanotube properties and applications that depend on the diameter, such as electric conductivity [39], hydrogen storage media, and super strong crystals [40], may now be investigated with an increased confidence of potential applicability. Catalytic production allows high efficiency and selectivity. Additional study of nanomaterials formed with various catalysts and promoters will help elucidate the growth dynamics, fundamental information that will further aid the development of potential applications.

References

[1] S. Iijima, Nature **354**, 56 (1991).

[2] M. R. Pederson and J. Q. Broughton, Phys. Rev. Lett. **69**, 2689 (1992).

[3] R. Saito, M. Fujita, G. Dresselhaus and M. S. Dresselhaus, Mater. Sci. Eng. B **19**, 185 (1993).

[4] R. S. Ruoff, D. C. Lorents, B. Chan, R. Malhotra, and S. Subramoney, Science **259**, 346 (1993).

[5] X. F. Zhang, X. B. Zhang, G. Van Tendeloo, S. Amelinckx, M. Op de Beeck, and J. Van Landuyt, J. Crystal. Growth **130**, 368 (1993).

[6] D. S. Bethune, C.-H. Kiang, M. S. de Vries, G. Gorman, R. Savoy, J. Vazquez, and R. Beyers, Nature **363**, 605 (1993).

[7] S. Iijima and T. Ichihashi, Nature **363**, 603 (1993).

[8] R. T. K. Baker and P. S. Harris, "The Formation of Filamentous Carbon," in *Chemistry and Physics of Carbon*, **14**, edited by P. L. Walker, Jr. and A. Thrower, (Marcel Dekker, New York,1978), pp.83–165.

[9] M. Endo, Chemtech **18**, 568 (1988).

[10] G. G. Tibbetts, Carbon **27**, 745 (1989).

[11] R. T. K. Baker, Carbon **27**, 315 (1989).

[12] Y. Saito, T. Yoshikawa, M. Okuda, M. Ohkohchi, M. Inagaki, Y. Ando, A. Kasuya, and Y. Nishina, Chem. Phys. Lett. **209**, 72 (1993).

[13] S. Seraphin, in *Recent Advances in the Chemistry and Physics of Fullerenes and Related Materials*, edited by K. M. Kadish and R. S. Ruoff (The Electrochemical Society, Pennington, NJ, 1994).

[14] W. Krätschmer, L. D. Lamb, K. Fostiropoulos, and D. R. Huffman, Nature, **347**, 354 (1990).

[15] P. M. Ajayan, J. M. Lambert, P. Bernier, L. Barbedette, C. Colliex, and J. M. Planeix, Chem. Phys. Lett. **215**, 509 (1993).

[16] M. S. de Vries, K. Reihs, H. R. Wendt, W. G. Golden, H. E. Hunziker, R. Fleming, E. Peterson, and S. Chang, Geochimica et Cosmochimica Acta **57**, 933 (1993).

[17] A. A. Lucas, P. H. Lambin, and R. E. Smalley, J. Phys. Chem. Solids **54**, 587 (1993).

[18] S. Iijima, P. M. Ajayan, and T. Ichihashi, Phys. Rev. Lett. **69**, 3100 (1992).

[19] H. Katsuki, K. Matsunaga, M. Egashira, and S. Kawasumi, Carbon **19**, 148 (1981).

[20] T. Kato, K. Kusakabe, and S. Morooka, J. Mater. Sci. Lett. **11**, 674 (1992).

[21] C.-H. Kiang, W. A. Goddard III, R. Beyers, J. R. Salem, and D. S. Bethune, J. Phys. Chem. **98**, 6612 (1994).

[22] D. H. Robertson, D. W. Brenner, and J. W. Mintmire, Phys. Rev. B **45**, 12592 (1992).

[23] P. M. Ajayan and S. Iijima, Nature **361**, 333 (1993).

[24] P. M. Ajayan, T. W. Ebbesen, T. Ichihashi, S. Iijima, K. Tanigaki, and H. Hiura, Nature **362**, 522 (1993).

[25] J. M. Lambert, P. M. Ajayan, P. Bernier, J. M. Planeix, V. Brotons, B. Cog, and J. Castaing, Chem. Phys. Lett. **226**, 364 (1994).

[26] S. Seraphin, D. Zhou, J. Jiao, J. C. Withers, and R. Loutfy, Appl. Phys. Lett. **63**, 2073 (1993).

[27] M. E. McHenry, S. A. Majetich, J. O. Artman, M. DeGraef, and S. W. Staley, Phys. Rev. B **49**, 11358 (1994).

[28] E. M. Brunsman, R. Sutton, E. Bortz, S. Kirkpatrick, K. Midelfort, J. Williams, P. Smith, M. E. McHenry, S. A. Majetich, J. O. Artman, M. De Graef, and S. W. Staley, J. Appl. Phys. **75**, 5882 (1994).

[29] C.-H. Kiang, P. H. M. van Loosdrecht, R. Beyers, J. R. Salem, D. S. Bethune, W. A. Goddard III, H. C. Dorn, P. Burbank, and S. Stevenson, to appear in Surf. Rev. Lett.

[30] S. Seraphin and D. Zhou, Appl. Phys. Lett. **64**, 2087 (1994).

[31] S. Subramoney, R. S. Ruoff, D. C. Lorents, and R. Malhotra, Nature **366**, 637 (1994).

[32] Y. Saito, T. Yoshikawa, M. Okuda, N. Fujimoto, K. Sumiyama, K. Suzuki, A. Kasuya, and Y. Nishina, J. Phys. Chem. Solids **54**, 1849 (1993).

[33] Y. Saito, M. Okuda, N. Fujimoto, T. Yoshikawa, M. Tomita, and T. Hayashi, Jpn. J. Appl. Phys. 2. Lett. (Japan) **33**, L526 (1994).

[34] X. Lin, X. K. Wang, V. P. Dravid, R. P. H. Chang, and J. B. Ketterson, Appl. Phys. Lett. **64**, 181 (1994).

[35] M. Endo, K. Takeuchi, S. Igarashi, K. Kobori, M. Shiraishi, and H. W. Kroto, J. Phys. Chem. Solids **54**, 1841 (1993).

[36] N. Hamada, S-I. Sawada, and A. Oshiyama, Phys. Rev. Lett. **68**, 1579 (1992).

[37] E. Dujardin, T. W. Ebbesen, H. Hiura, and K. Tanigaki, Science **265**, 1850 (1994).

[38] S. C. Tsang, Y. K. Chan, P. J. F. Harris, and M. L. H. Green, Nature **372**, 159 (1994).

[39] R. Saito, M. Fujita, G. Dresselhaus, and M. S. Dresselhaus, Appl. Phys. Lett. **60**, 2204 (1993).

[40] J. Tersoff and R. S. Ruoff, Phys. Rev. Lett. **73**, 676 (1994).

Chapter 6

Further Characterization of Carbon Nanomaterials

6.1 Introduction

Since the discovery of multi-layer carbon nanotubes by Iijima in 1991 [1], there have been numerous studies of the synthesis and characterization of these materials. Investigations of these materials have relied heavily on microscopy, due to the difficulty of obtaining pure samples. Despite a wealth of theoretical work on the electronic structure [2, 3, 4, 5, 6, 7] and vibrational properties [6, 8, 9] of single-layer nanotubes, very little characterization beyond transmission electron microscopy (TEM) imaging and diffraction has been done, owing to the difficulty in separating the tubes from the soot. Recently the Raman spectrum of a soot containing nanotubes and Co particles has been reported [10]. The spectrum exhibits features that are assigned to the vibrational frequencies of single-layer tubules. Transmission electron energy loss spectroscopy has been applied to study the electronic structure of a bundle of single-layer nanotubes [11]. TEM, however, remains the most powerful general structural

tool for studying catalytically grown single-layer carbon nanotubes.

In this chapter we discuss the many structures that are produced by the reaction conditions described in Chapter 5. Various deformations to perfect nanotubes are detailed. Destruction and reconstruction reactions catalyzed by the electron beam are discussed. A variety of carbonaceous nanotubule structures are exhibited. The metal particles produced in this process are also discussed in some detail.

6.2 Structures of Single-Layer Carbon Nanotubes

The morphology of tubes synthesized with the Co catalyst is different from that of tubes produced without a catalyst. Figure 6.1 depicts typical soot produced by the Co catalyst. Thin threads of tubules are woven into a carbon net, giving rise to a rubbery texture. Those formed on the cathode tip without a catalyst are straight and have multiple layers, whereas those produced with a Co catalyst are single-layered with a rigidity that seems to depend on diameter. Large (diameter $>$ 2 nm) nanotubes often appear deformed from the perfect cylindrical shape of small diameter tubes, as shown in Fig. 6.2a. Figure 6.2b displays an end view of a cylindrical 1 nm diameter tube. Deformation of tubes in the radial direction normally occurs at intersections with other materials such as the soot or other tubes. As a typical example, tube A in Fig. 6.2a can be seen to deform only at its junction with the soot. Similarly, defects often occur when tubes are tangled with each other (Figs. 6.3ab).

Folding of tubes was commonly observed, particularly for larger diameter tubes. Figure 6.4a shows a 3.3 nm diameter tube that folded along the soot, with a rigid 1.5 nm diameter tube nearby. Figure 6.4b displays a 2 nm diameter tube wrapped around the soot, with two apparent defects that change the tube axial direction. The nanotube diameter appears unchanged throughout the stretch of the tube seen on the images. This is in contrast to bends in multilayer tubes, which are caused by pentagon

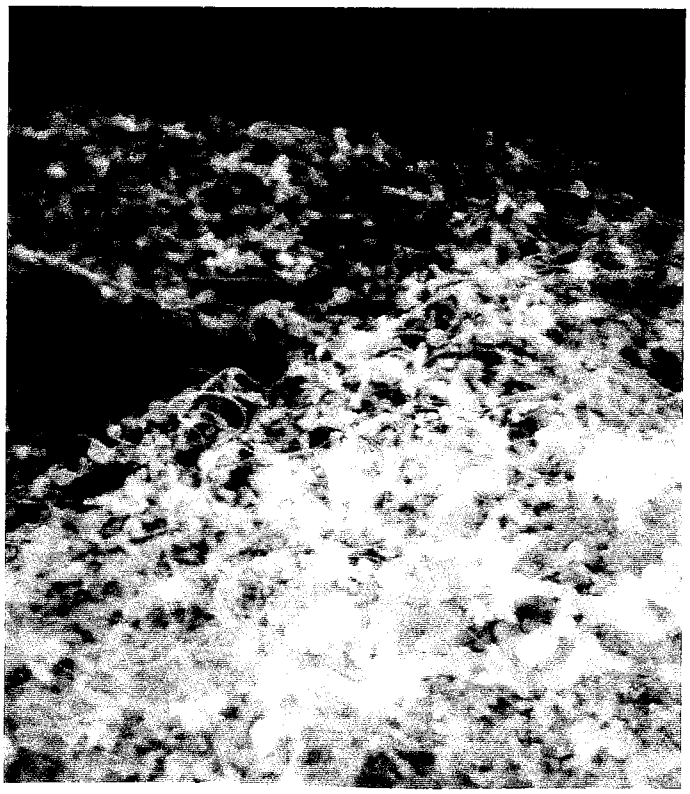

Figure 6.1: Scanning electron micrograph of soot containing nanotubes made with cobalt catalyst.

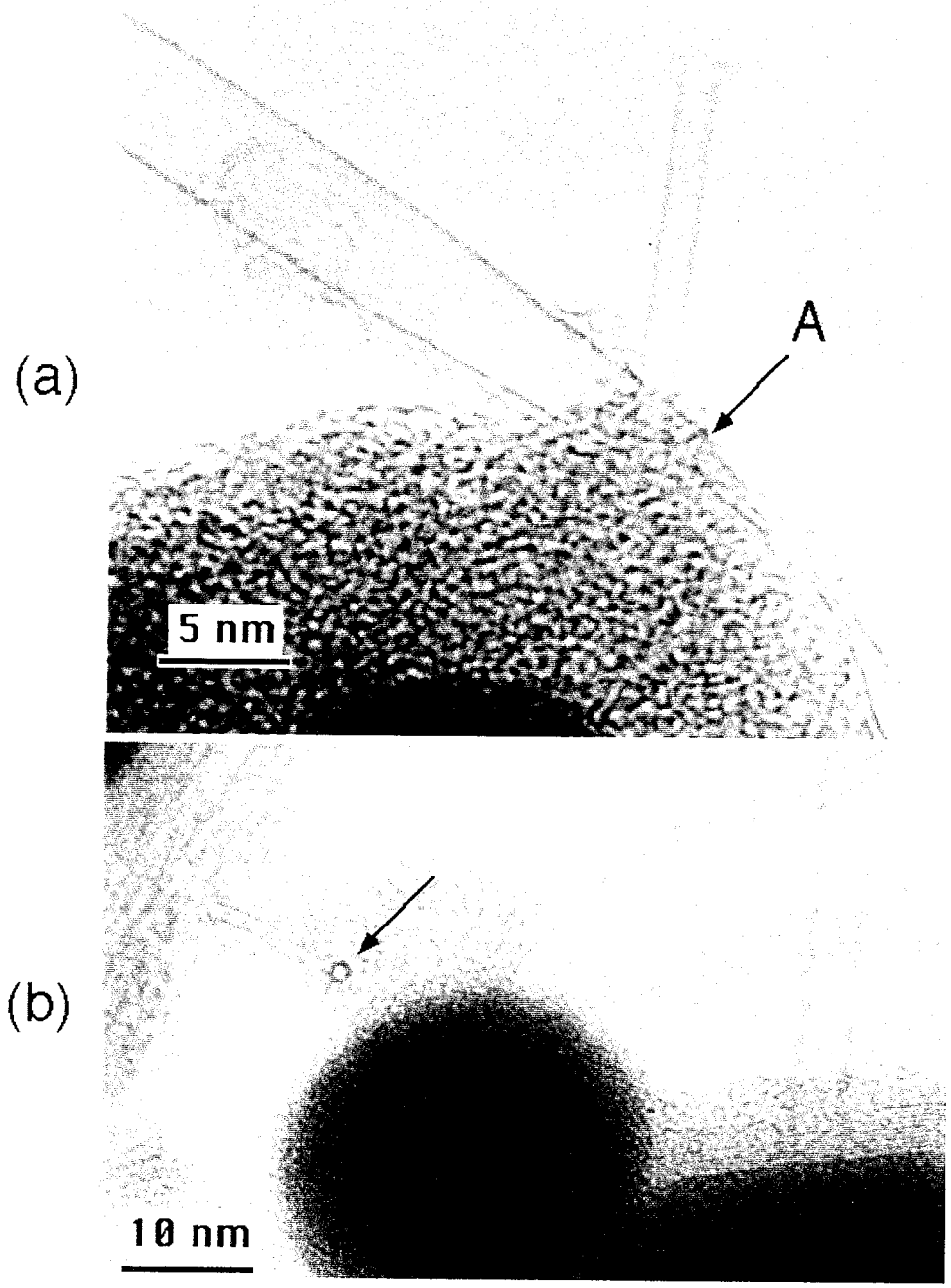

Figure 6.2: TEM of soot containing nanotubes of different diameter. (a) The larger tube is a 3.8 nm diameter tube, showing deformation near the soot. (b) The end view of a tube showing a near circular shape, indicating a cylindrical, tubular structure.

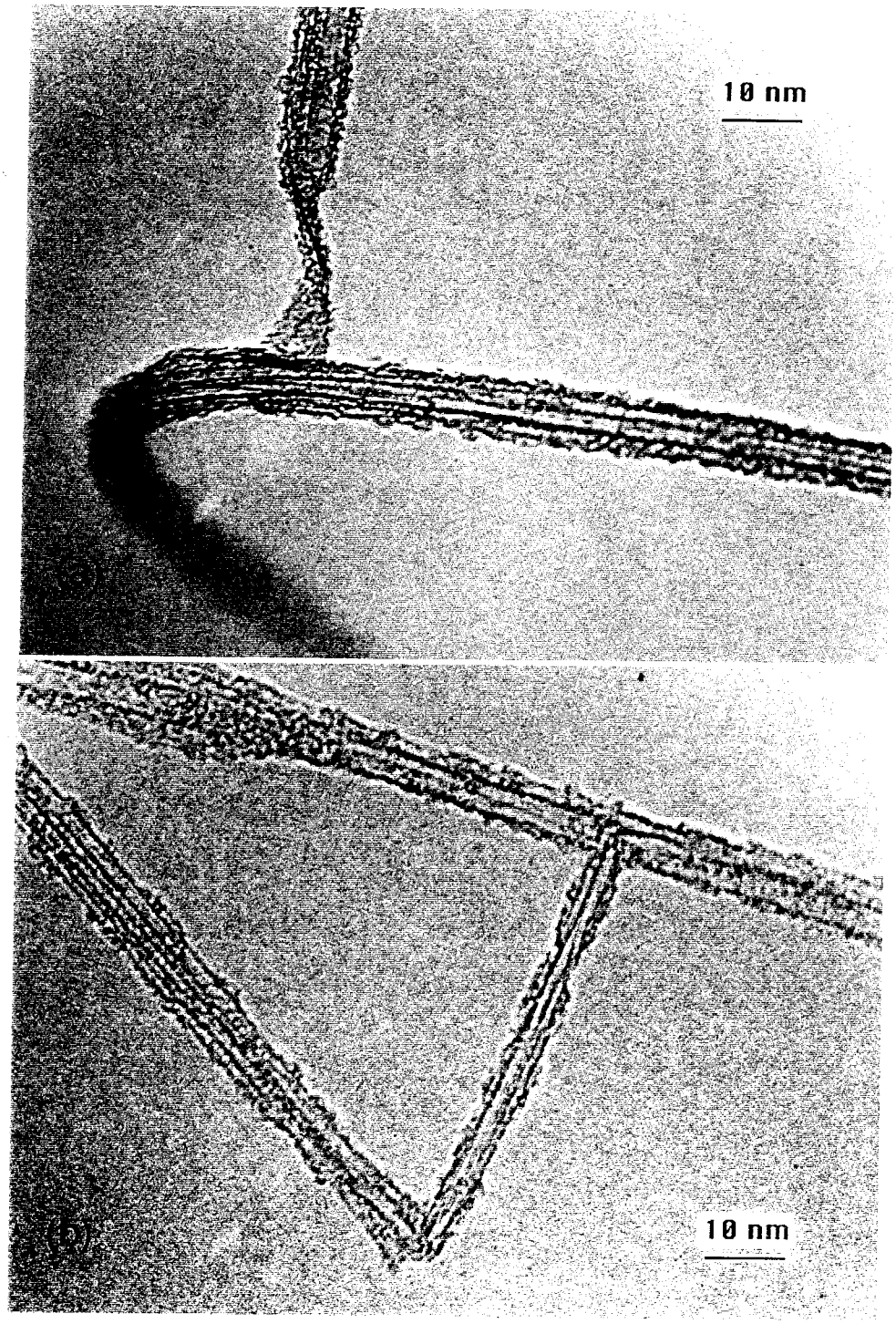

Figure 6.3: TEM of nanotubes showing (a) twisting and (b) bending.

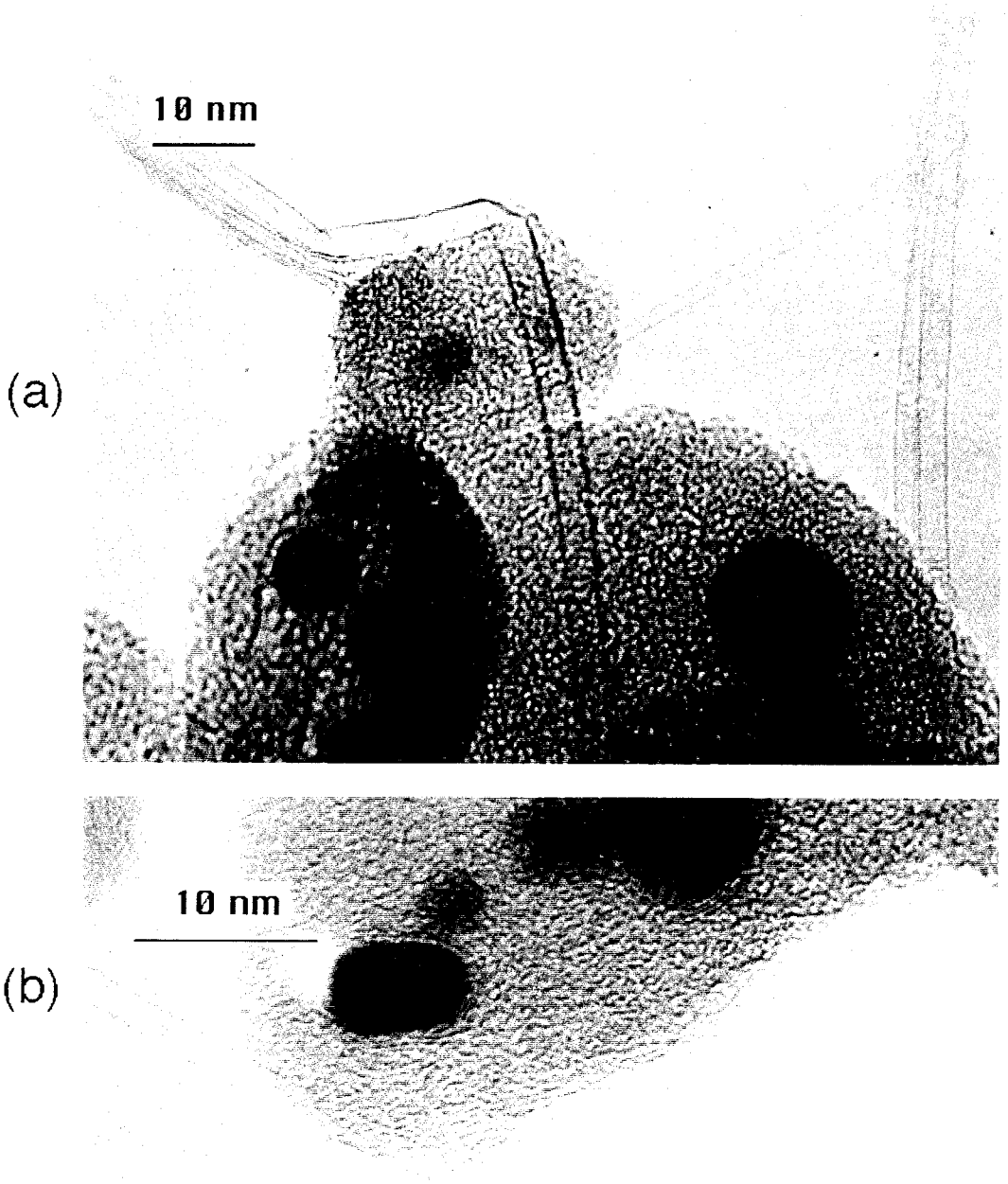

Figure 6.4: TEM showing nanotubes wrapped around the soot.

or heptagon defects and which change the tube diameter [12]. This result suggests that the twisting and folding of the single-layer nanotubes was likely introduced after the tubes were formed, since such tension during the formation process would likely have lead to defects that would have changed the diameter.

The ends of the tubes are also of interest, for they can contain clues to the growth mechanism of these nanotubes. For example, carbon fibers grown in the vapor phase are believed to stem from carbon that diffuses on the surface of catalyst particles. This model is supported by TEM results that show almost all the tubes terminate with a metal particle [13, 14, 15]. The multilayer tubes grown on the cathode deposit without a catalyst, however, grow with an open end. They stop when pentagons form and the tubes close [16]. This growth model is based solely on TEM observations, the most significant source of structural information to date. We examined TEM images showing the terminations of the catalytically-grown single-layer tubes in an effort to gain some insight into the formation process. Figure 6.5 shows tube ends containing pentagons in the cap [12]. According to Euler's theorem for the closure of a hemisphere with polygons, six pentagons are required to cap the tube with hexagon network [18, 19, 20]. Conical capping, on the other hand, needs five pentagons to complete the cone at the tube end [20, 21]. We have observed tubes capped with both polygons and cones in the catalytically grown single-layer nanotubes (see Fig. 6.5). No catalyst particles were ever found at the end of the tubes. The shapes of the tube ends resemble those of the multilayer tubes [12, 16]. We, therefore, propose a growth model similar to the one suggested for tubes grown on the cathode. In this model the closure of the tubes is a result of a sudden change of the environment, *e.g.* temperature or carbon vapor density, which causes the formation of pentagons that eventually cap the tube.

On the molecular scale, single-layer carbon nanotubes can be thought of either as a one-dimensional crystal or as an all-carbon semi-flexible polymer. Alternatively,

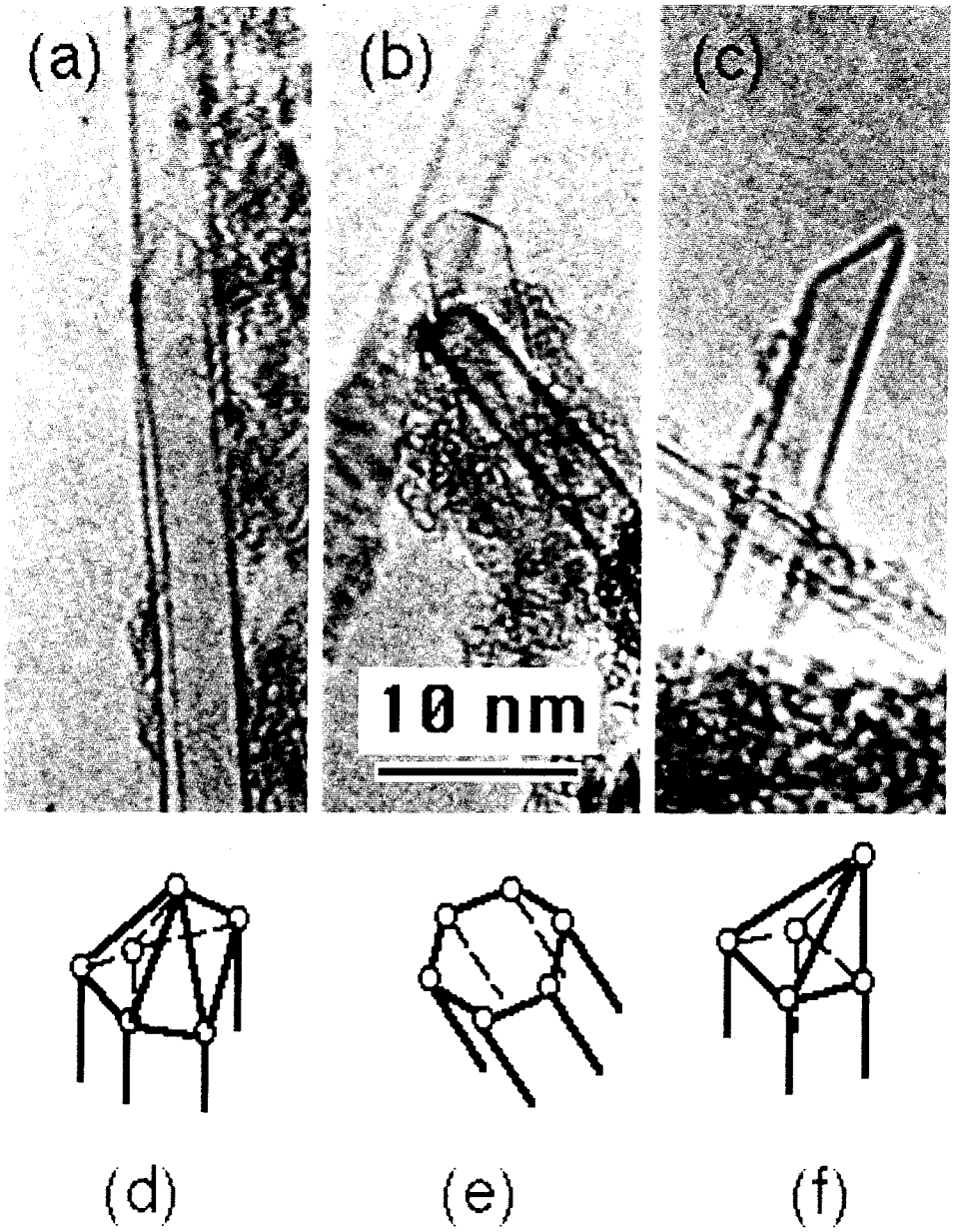

Figure 6.5: TEM of different structures of single-layer nanotube ends. The tubes are capped, similar to the ends of multilayer nanotubes. The open circle indicates a pentagon. (a) Helical tube capped with six pentagons, as illustrated in (d). (b) Two tubes capped with six pentagons. The non-helical tube end is illustrated in (e). (c) Cone-shaped capping with 5 pentagons, as illustrated in (f).

one can think of capped nanotubes as extended fullerenes [17]. For example, one can take a C_{60} molecule and add a belt of carbon to form a C_{70}. By repeating the process one can make a long tubule of 0.7 nm diameter with zero helicity [2]. Likewise, joining belts of 75 edge-sharing benzene rings generates a nanotube of about 6 nm diameter.

The detailed atomic arrangement of carbon nanotubes can be obtained directly from TEM images and diffraction patterns. Figures 6.6 shows the diffraction pattern and the $D = 3.6$ nm tube that the diffraction pattern was taken from. A helicity angle of $\alpha = 30^\circ$, which represent a zero-helicity, armchair structure, was obtained from the diffraction pattern [22, 23]. With the diameter D and helicity α from the diffraction pattern, one can determine the molecular structure of the tube uniquely. Whereas nonzero helicity is thought to be essential for the growth of multilayer nanotubes [16], we have observed several tubes with zero helicity, similar to that shown in Fig. 6.6. The difference in the nucleation process is considered to be the reason for the discrepancy. An interpretation of these results will be presented in the section of growth model.

Thermogravimetric analysis (TGA) of soot containing nanotubes has shown a low onset temperature of decomposition. We heated the soot made with Co and Co+S in N_2 at rate 10° C/min, and found that the weight loss started at $\sim 400^\circ$ C, as shown in Figs. 6.7a and 6.7b, compared to $\sim 600^\circ$ C for C_{60} and $>1000^\circ$ C for graphite [24]. The lack of stabilization of dangling bonds from graphite basal planes for single-layer nanotubes could cause the tube to decompose rapidly once the end is open. Individual single-layer nanotubes are, therefore, expected to be unstable at high temperature.

6.3 Electron Beam Heating of the Nanotubes

Although stable nanotube structures contain information about the formation process, a study of the reaction dynamics of the tubes is essential to gain definite con-

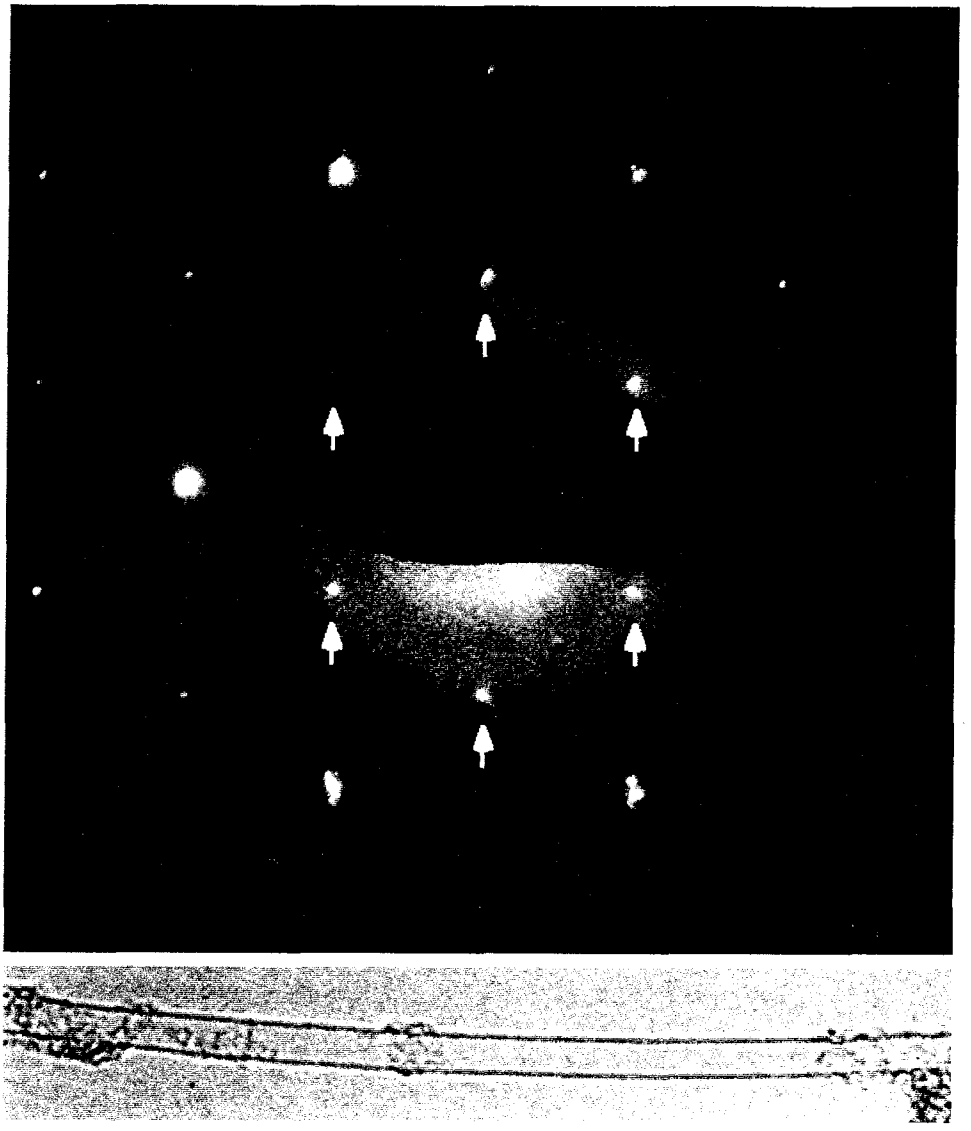

Figure 6.6: Diffraction pattern and image of a single-layer nanotube. The pattern shows the tube has a zero-helicity, armchair structure.

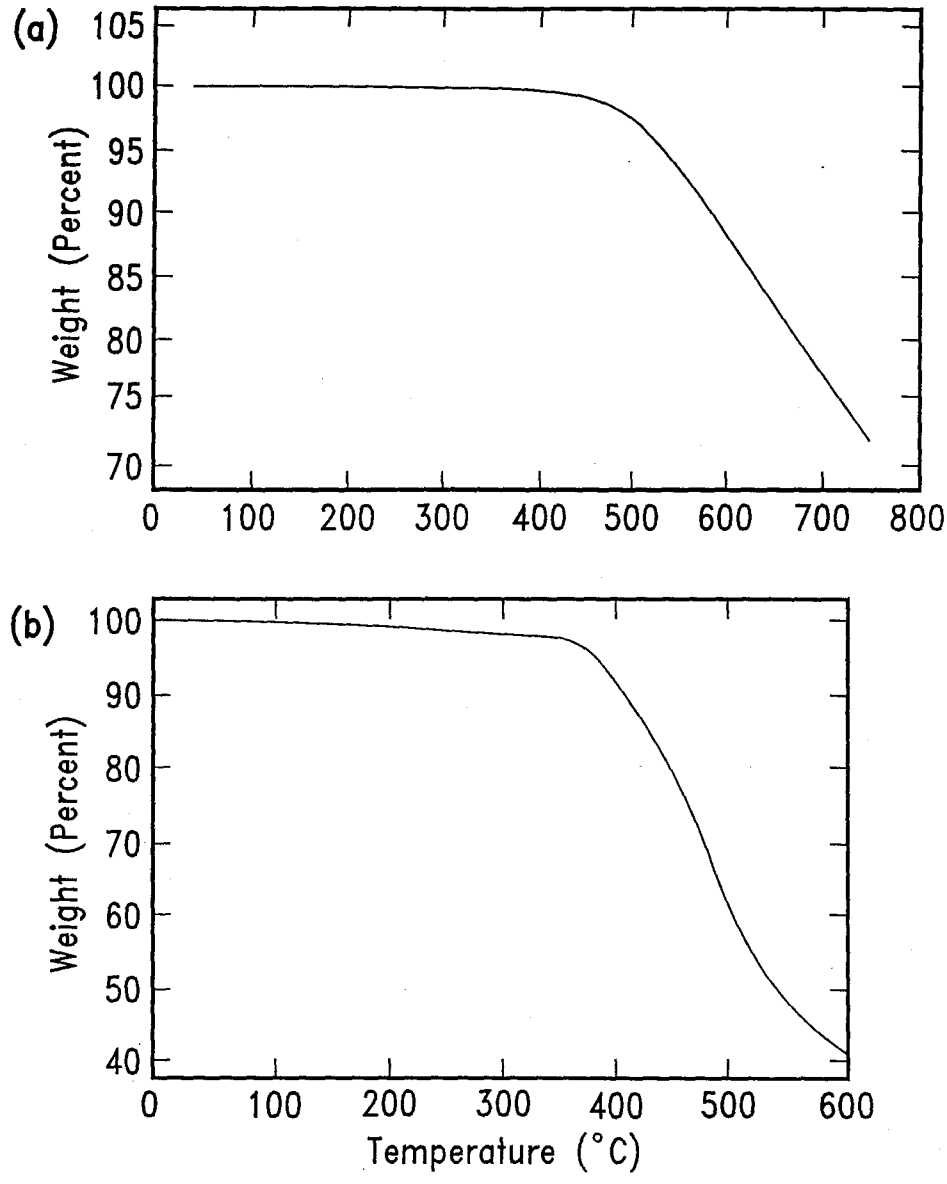

Figure 6.7: Thermogravimetric analysis of soot containing single-layer nanotubes made with (a) Co and, (b) Co and S. Samples were heated in N_2 at the heating rate of 10 ° C/min.

clusions. Electron beam heating has been demonstrated to transform a multilayer nanotube into a nested fullerene cage [25]. Studies of the structural evolution due to local heating of the tubes under vacuum may furnish an understanding of the self-assembly process of carbon nanotubes.

A variety of reactions induced by the electron beam were observed for the nanotubes under the microscope. The most common phenomenon was a perfectly straight tube that gradually developed small ripples. This eventually resulted in breakage of the tube, as shown in Fig. 6.8. Both individual and bundles of tubes were split in this way after a few minutes of electron beam heating. The free ends usually reconstructed to form caps (pointed with solid arrows), but some of the tubes were left opened (pointed with hollow arrows). Occasionally the tubes were fragmented into sections, as in the tube in Fig. 6.9a where a 3 nm tube is supporting a 2 nm tube that has been disintegrated into small sections of open cylinders. These segments could later reconstruct to form giant fullerenes. Electron beam heating can also be used in a constructive way. Figure 6.9b is a tube with a segment that originally had a kink. Under intense electron beam heating, the defect seemed to be patched, and the tube acquired a regular, cylindrical shape.

These phenomena can be rationalized by considering the strain induced by defects in the tube, leading to a structure less stable than the perfect hexagonal bonding network. When excess energy is put into the tube, the C–C bonds absorb the energy. They may rearrange, or they may dissociate, causing deterioration of the tube or evaporation of excess carbon. The choice between destruction and reconstruction depends on the dynamics of the heat distribution and bond rearrangement. It also depends on the difference between the heat required for destruction and the barriers to reconstruction. Figures 6.10a to 6.10d show a sequence of tube evolution under electron beam irradiation. Initially the tube was almost divided into two tubes at the turning point. After a few seconds of electron beam heating, the two sections of the

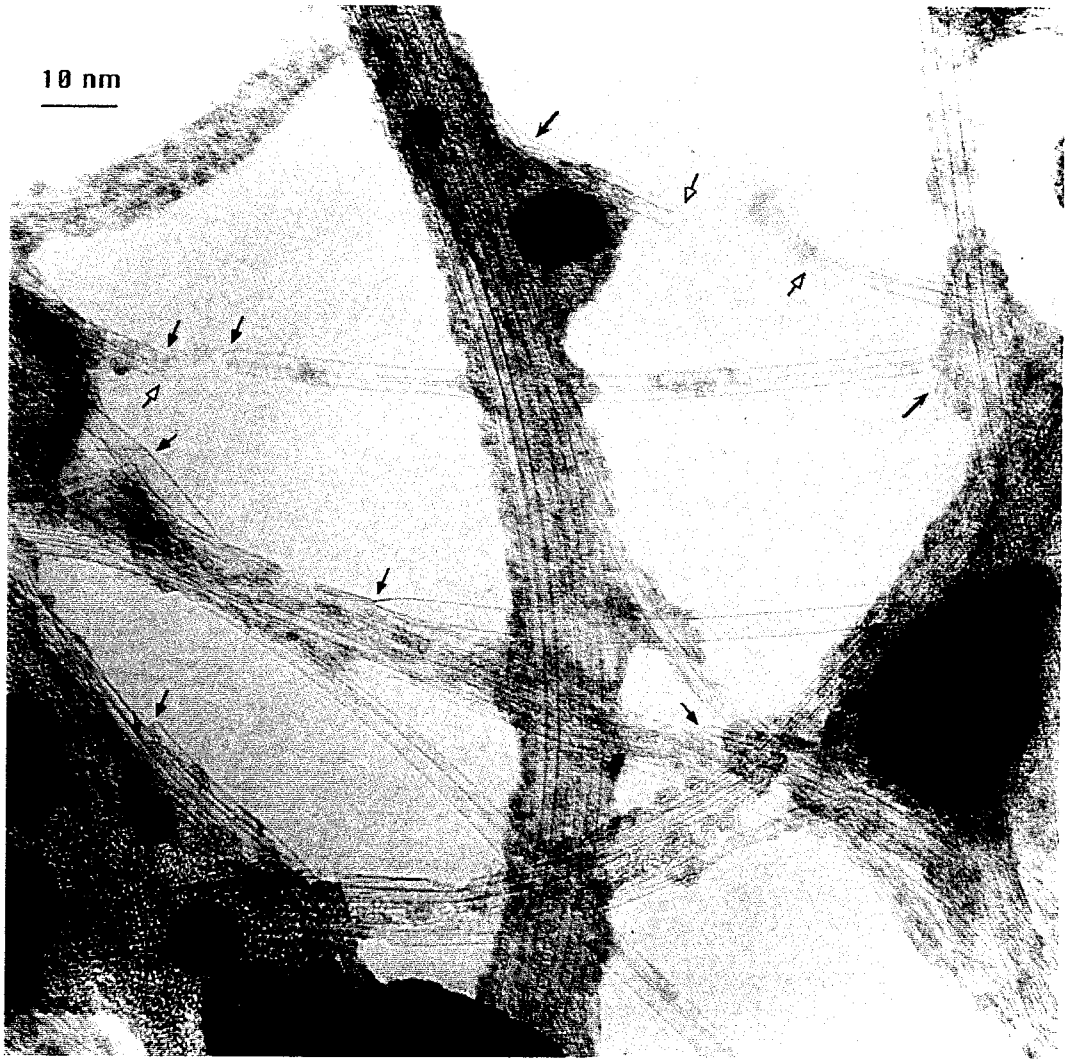

Figure 6.8: Nanotubes disintegrated under electron beam heating. The arrows point at locations where structural modification occurred due to the electron beam heating. The solid arrows are pointing to closed ends and the hollow arrows are pointing to open ends of nanotubes.

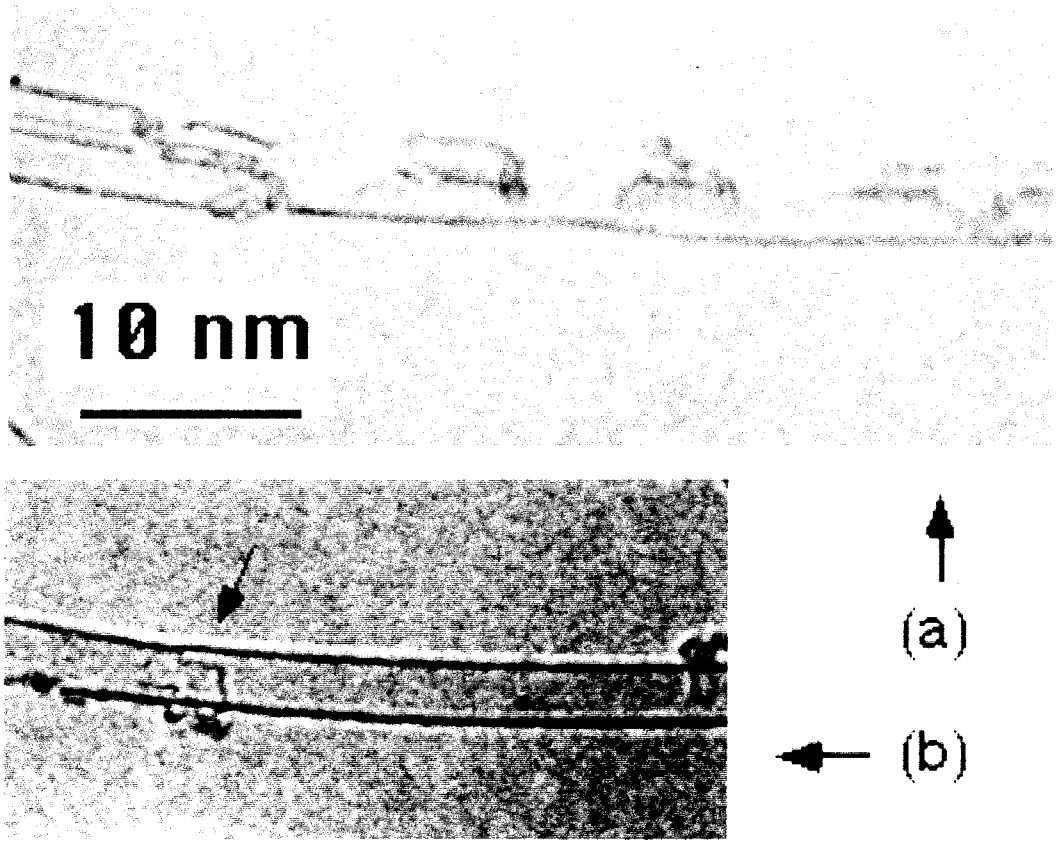

Figure 6.9: Breaking and forming carbon bonds of single-layer nanotube under electron beam heating. In (a) the tube was broken into sections, and in (b) the originally defective section was gradually healed.

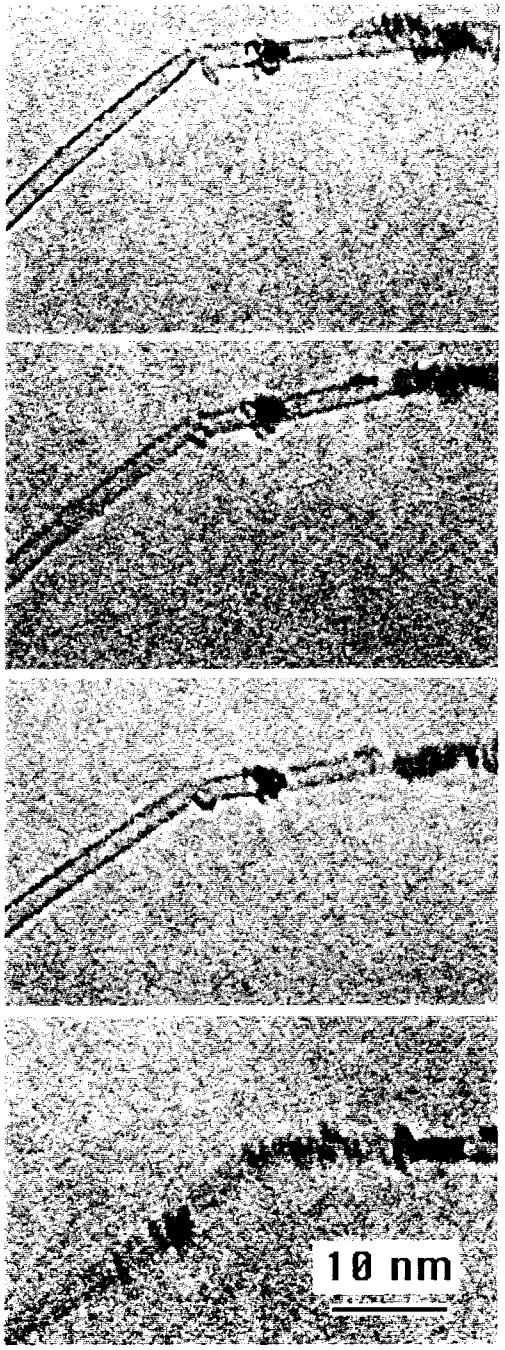

Figure 6.10: A nanotube heated by intense electron beam. From top to bottom: tube was almost divided into two tubes at the turning point. The two sections of the tube almost recombined after a few seconds of electron beam heating. Prolonged heating broke the tube.

tube joined and almost recombined. Prolonged heating, however, eventually caused the tube to fracture.

We also observed bundling of nanotubes in real time. Figures 6.11a to 6.11c are a series of images taken at approximately 1 minute intervals. The tube was initially bridging between two bundles. After being heated for 1 minute bundle A disintegrated and the tube was separated from it. Tube A slowly approached bundle B, coming to rest next to bundle B. Note that it took about 2 minutes for the tube to sweep across the 20 nm distance. This is an exceptionally long time for such a microscopic motion. The force responsible for assembly of nanotube bundles is usually assumed to be to van der Waals [26], with the tubes zipping-up to form a bunch. The extremely slow event in this figure, however, appears not to be explainable by van der Waals or electrostatic attraction. Other materials exist in the soot, which could hinder the aggregation of the tubes. Figure 6.12a shows two tubes coupled nicely together, whereas Fig. 6.12b shows an example of two adjacent tubes split at the end, where one tube has a free end that points away from the tube. It is conceivable that if material obstructed the clustering, the tubes would stay apart, as the material would block the aggregation. Analogously, we can see from Figs. 6.11a to 6.11c that while imaging the tubes with the electron beam, bundle A was gradually disintegrated. Therefore, a plausible explanation for the slowness of the reaction is that the electron beam radiation was slowly removing the blocking group that prevented the tubes from aggregating, *i.e.* bundle A and the soot near the root of the tube. Under these conditions, the reaction rate would be controlled by evaporation or decomposition of the obstacles to the tube aggregation.

Use of a transmission electron beam to both induce and view the reaction enables us study reactions *in situ* and in real time. The effects of heating could be utilized to generate various rearrangements of nanotubes that may be worth investigating. For example, under appropriate conditions the defects in the tubes may be repaired

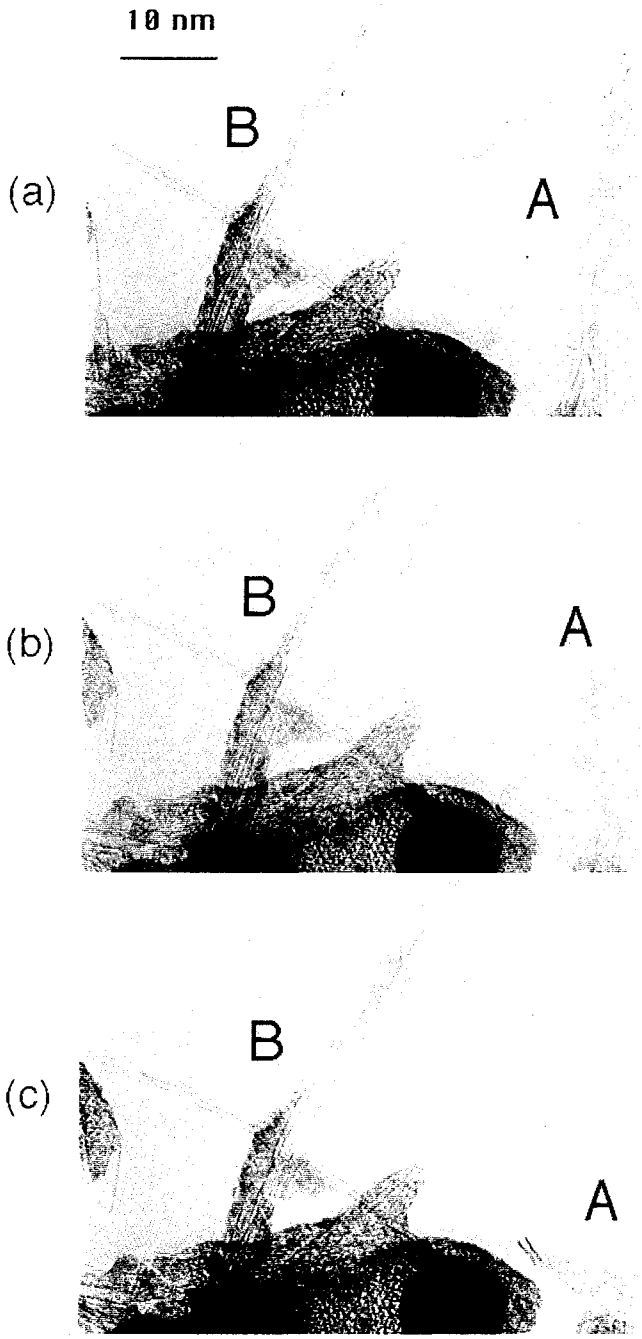

Figure 6.11: Nanotube bundling imaged in real time. (a) A tube bridge between bundle A and B. (b) Bundle A disintegrated, and the tube is pulled towards bundle B. (c) The tube eventually bundled with B.

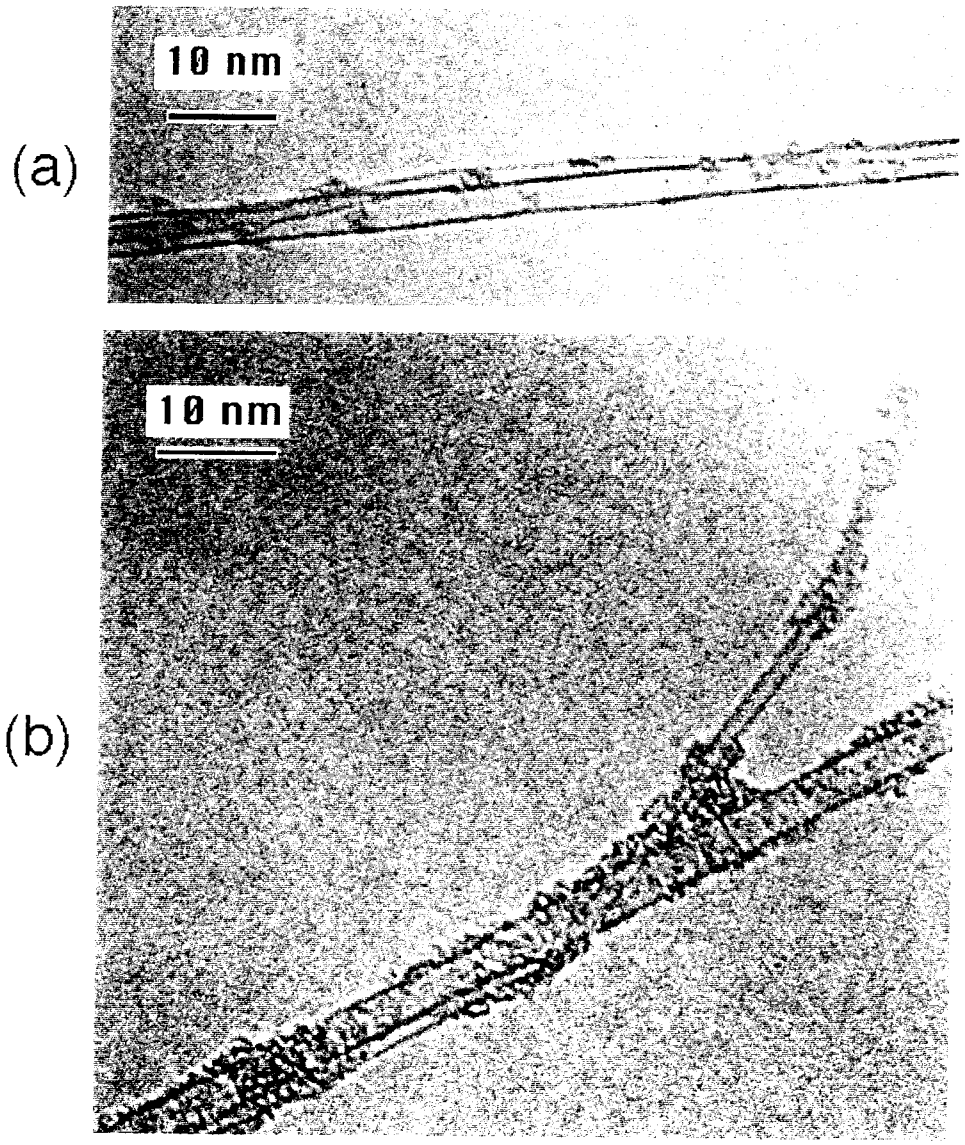

Figure 6.12: Two nanotubes coupled together. In (b) the tubes split at one end.

in an effort to strengthen the materials. Moreover, breakage and reconstruction of the tubes modifies the morphology of the soot. This could result in a material phase transition from, for example, rubber to glass or crystal. Additives may also prove fruitful in an effort to make a nanotube composite with useful material properties.

6.4 Other Carbon Structures Produced in the Arc

When Co and S were added to the anode of the arc, a variety of interesting carbon structures formed around the cathode and developed into a rubbery soot [27, 28]. Figure 6.13 gives an overview of the composition of this fuliginous deposit. Multilayer and single-layer nanotubes, strings of cone-shaped compartments, carbon nanofibers with metal particles at the tips, and filled nanotubes were all present in this soot. These carbon materials, except for the single-layer nanotubes, are usually not found in this soot when using Co alone. The catalytic properties of sulfur, therefore, must play an important role in the formation of these materials.

Multilayer carbon nanotubes, similar to those nanotubes usually found in the central portion of the cathode deposit [1], are occasionally found in this soot. Figure 6.14 shows a multilayer nanotube in this soot, with two single-layer nanotubes adjacent to it. The diameter of the innermost shell of the multilayer nanotube (6.5 nm) is much larger than that of the single-layer nanotubes (1.6 nm). The multilayer nanotubes have diameters comparable to those found in the central portion of cathode deposit generated without a catalyst, whereas the single-layer nanotube diameters lie in the range corresponding to the tubes found on the chamber walls [28].

The composition of the central part of the cathode deposit is similar to that formed without a catalyst. Figure 6.15 shows that multilayer nanotubes and graphitic polyhedral particles are the major components of this deposit. We did observe, however, that some tubes appear different from those produced without a catalyst. Figure

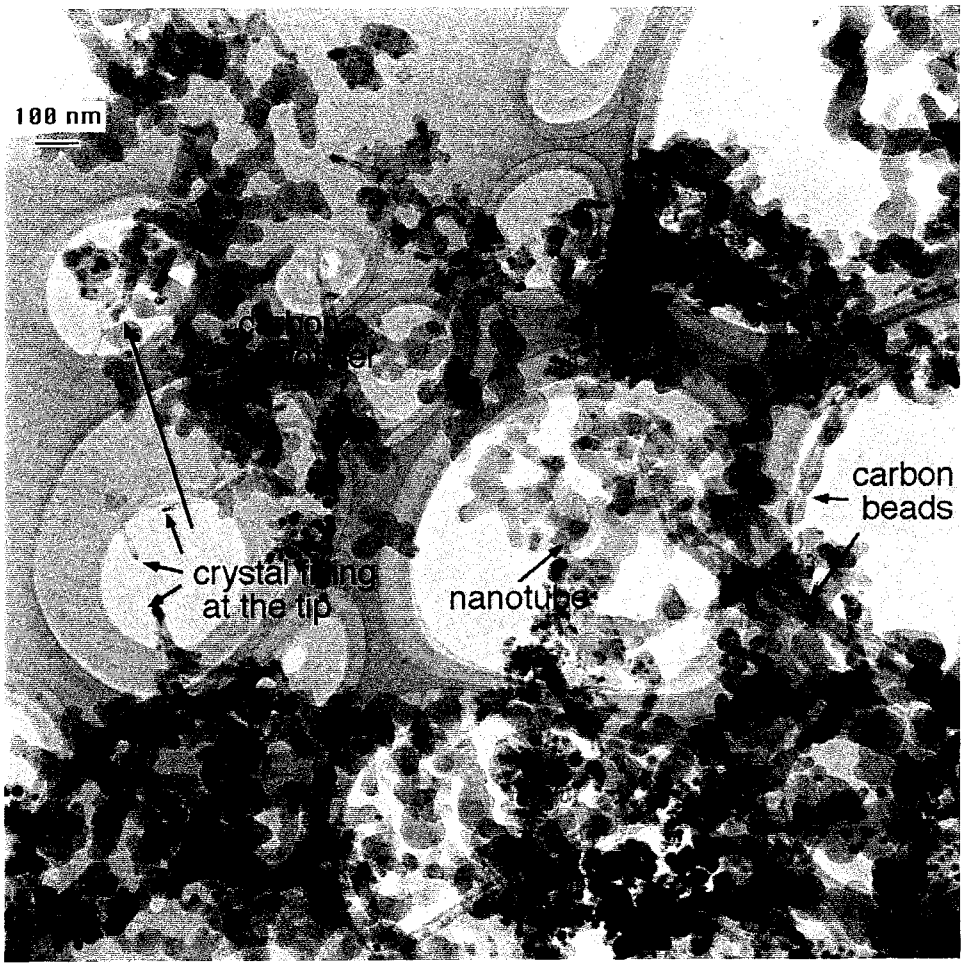

Figure 6.13: Various carbon structures exist in the rubbery soot around the cathode when both Co and S were used in the anode.

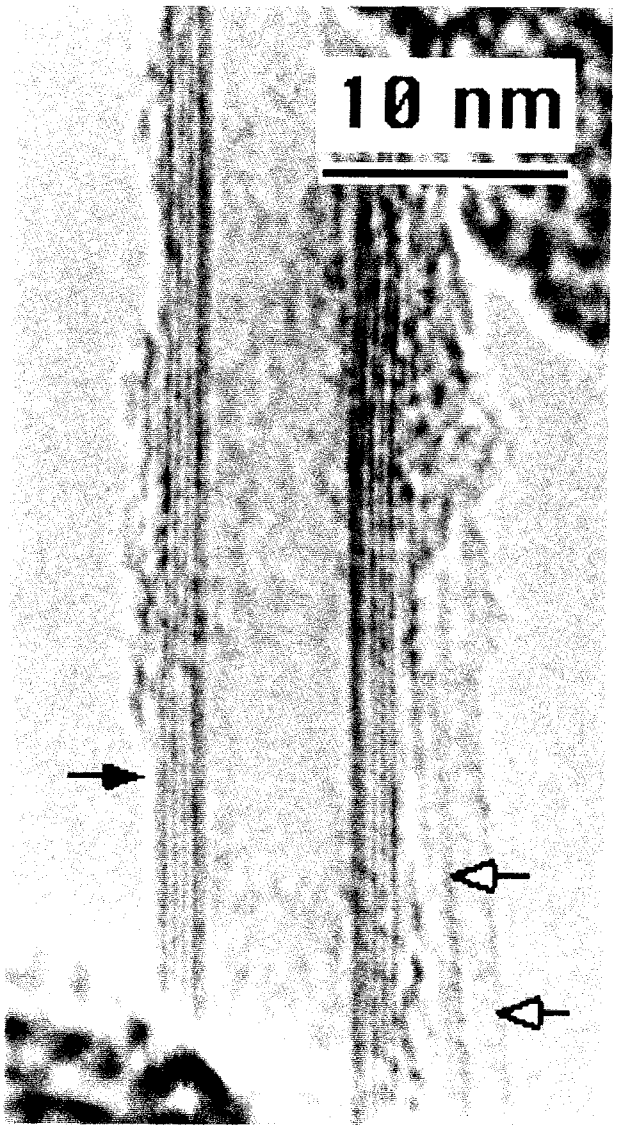

Figure 6.14: Multilayer and single-layer nanotubes co-exist in the soot around the cathode.

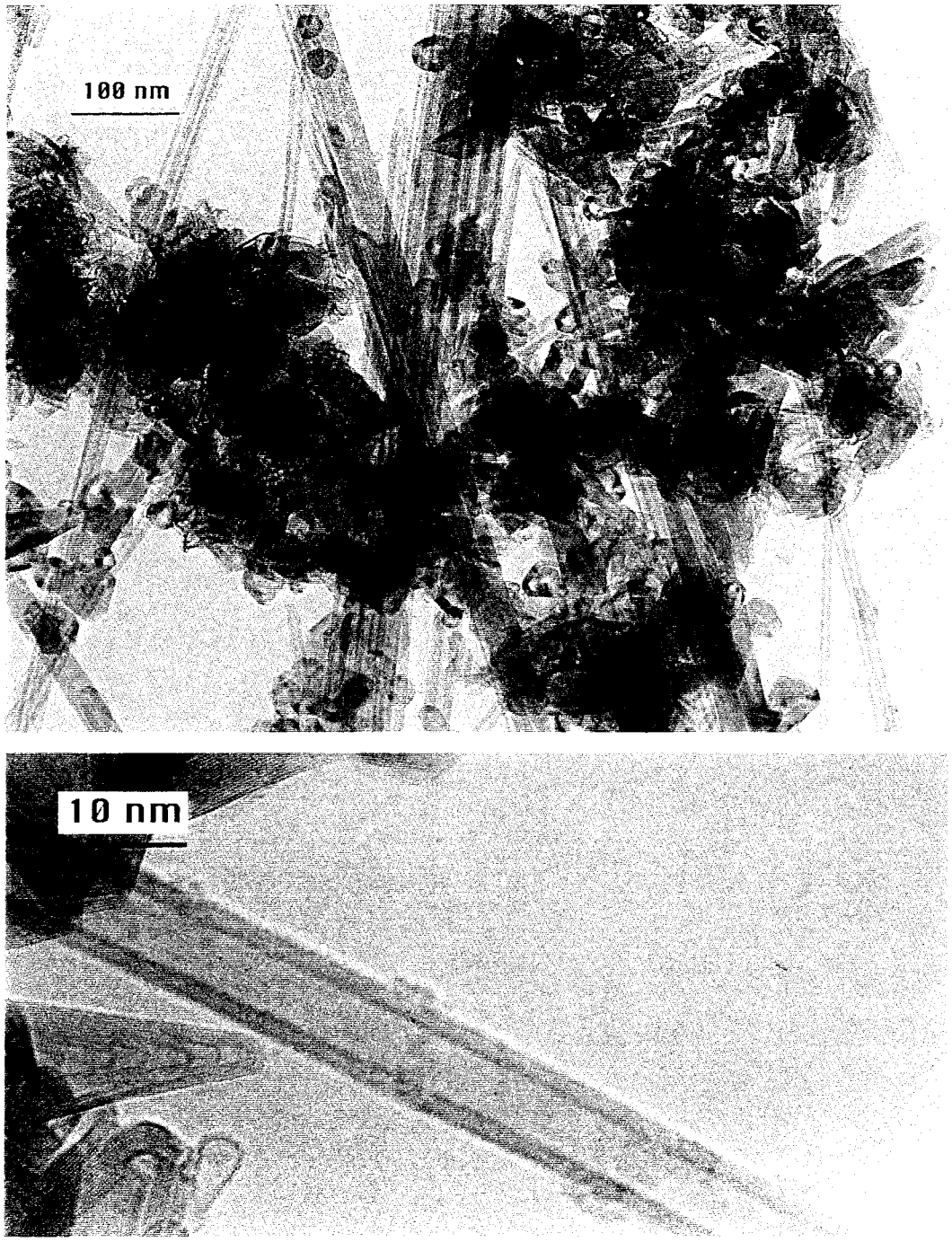

Figure 6.15: A typical composition of the central part of cathode deposit formed without catalyst.

6.16, for example, shows a curved tube with many defects, unusual for nanotubes formed without a catalyst.

The coexistence of multilayer nanotubes and single-layer nanotubes in this soot is intriguing. This is the first report of multilayer nanotubes found outside the center deposit. The soot deposited on the wall, generated with Co catalyst, contains almost no multilayer nanotubes [28, 29]. Multilayer tubes are believed to grow from a surface, under a high electric field [16, 30, 31], whereas single-layer tubes form catalytically in the gas phase. It appears that these multilayer nanotubes formed on the surface. The single-layer nanotubes, on the other hand, assembled in the gas phase prior to landing on the electrode.

Figure 6.17 demonstrates the various conical carbon structures found in the rubbery soot around the electrode. Conical carbon filaments, strings of beads, and cone-shaped compartments are common products observed in this soot. At a higher magnification, we can see from Figure 6.18 that the cone is composed of several layers of carbon. The graphene planes in graphite filament are tilted at an angle with respect to the filament axis. Conical carbon filaments have been produced at $\sim$ 500–650 $^\circ$C, a temperature well below the melting point of catalytic particles [32]. A model for the growth of these conical carbon filament structures has been proposed [32]. In brief, the carbon diffuses through the catalytic particle that is in its solid crystalline state, and the carbon grows into graphene sheet that breaks away from the catalyst at a specific crystalline facet. These graphite whisker-like filaments are similar to those carbon fibers grown in the vapor phase, formed by hydrocarbon decomposition on transition metal particles [33]. Support for this filament growth model is shown in Figure 6.19, where graphite sheets seem to grow out of the particle at the filament end. The carbon at the tip of particle appears amorphous, which would poison the catalytic activity of the particle and, therefore, terminate the filament growth. Energy dispersive spectra (EDS) of the particle at the termination of the fiber indicates

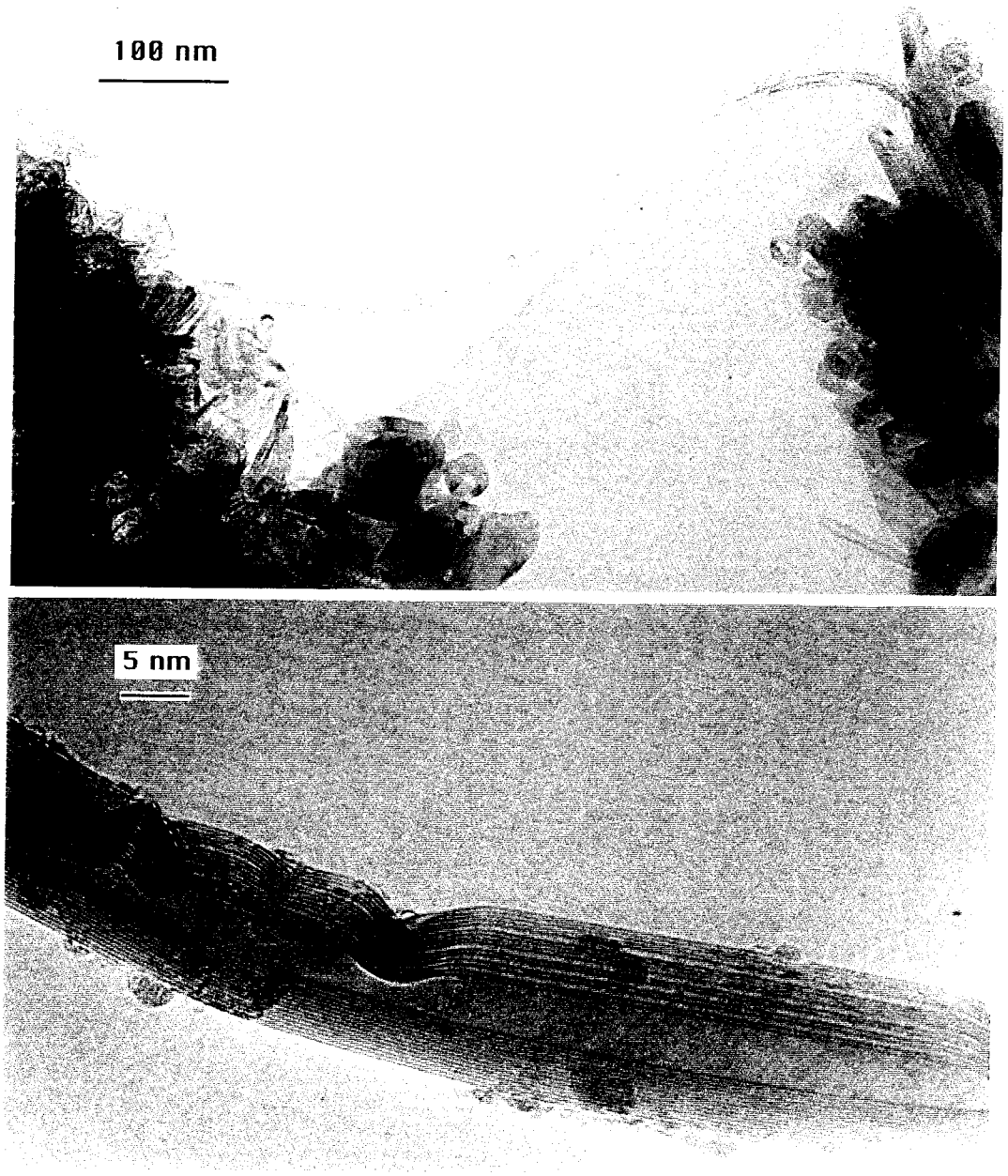

Figure 6.16: Multilayer nanotube found in the center part of cathode deposit. The anode used to generate the arc contains Co and S.

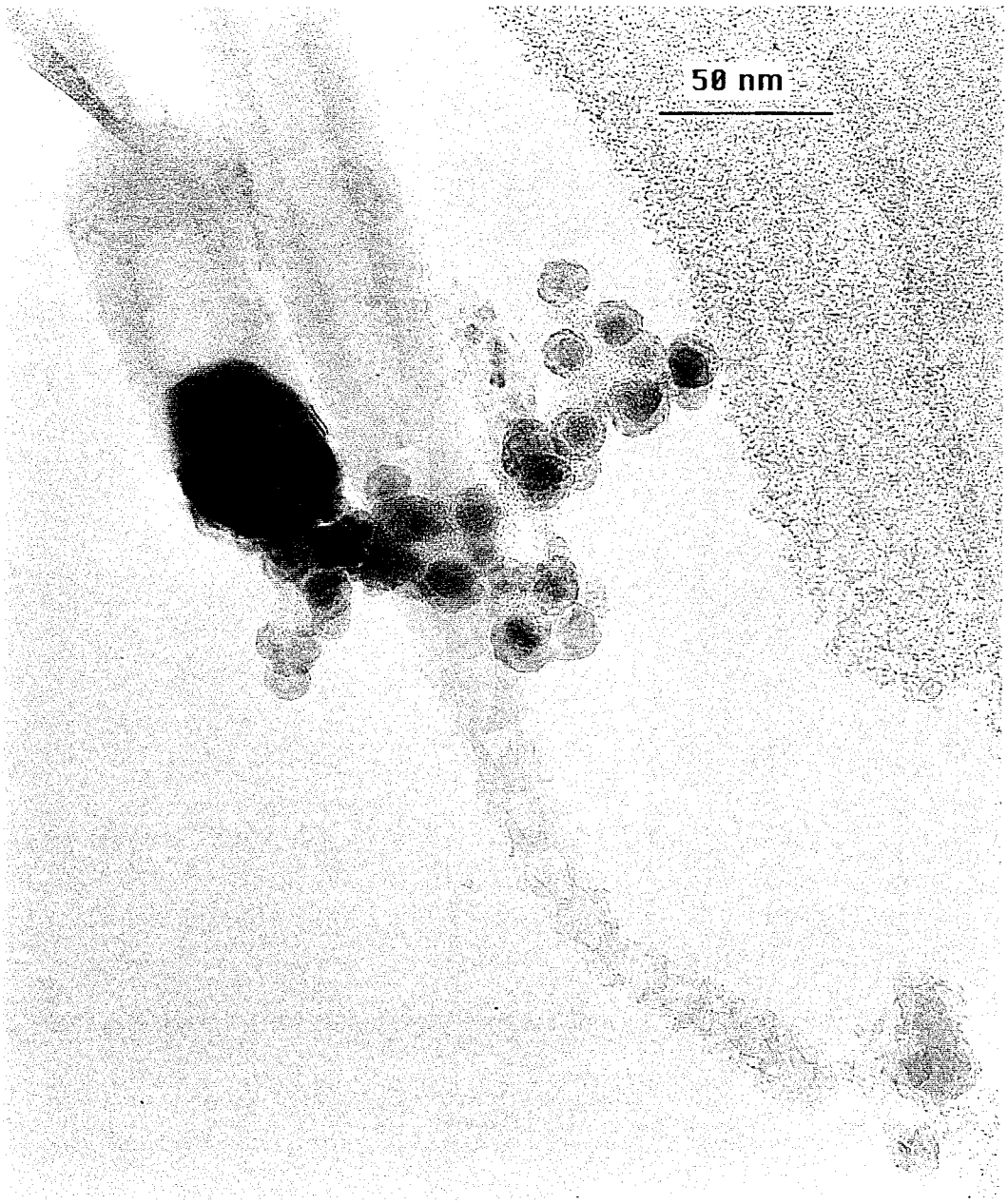

Figure 6.17: Conical graphite filament linked to a strings of carbon beads in the soot around the cathode, when Co and S were added to the anode.

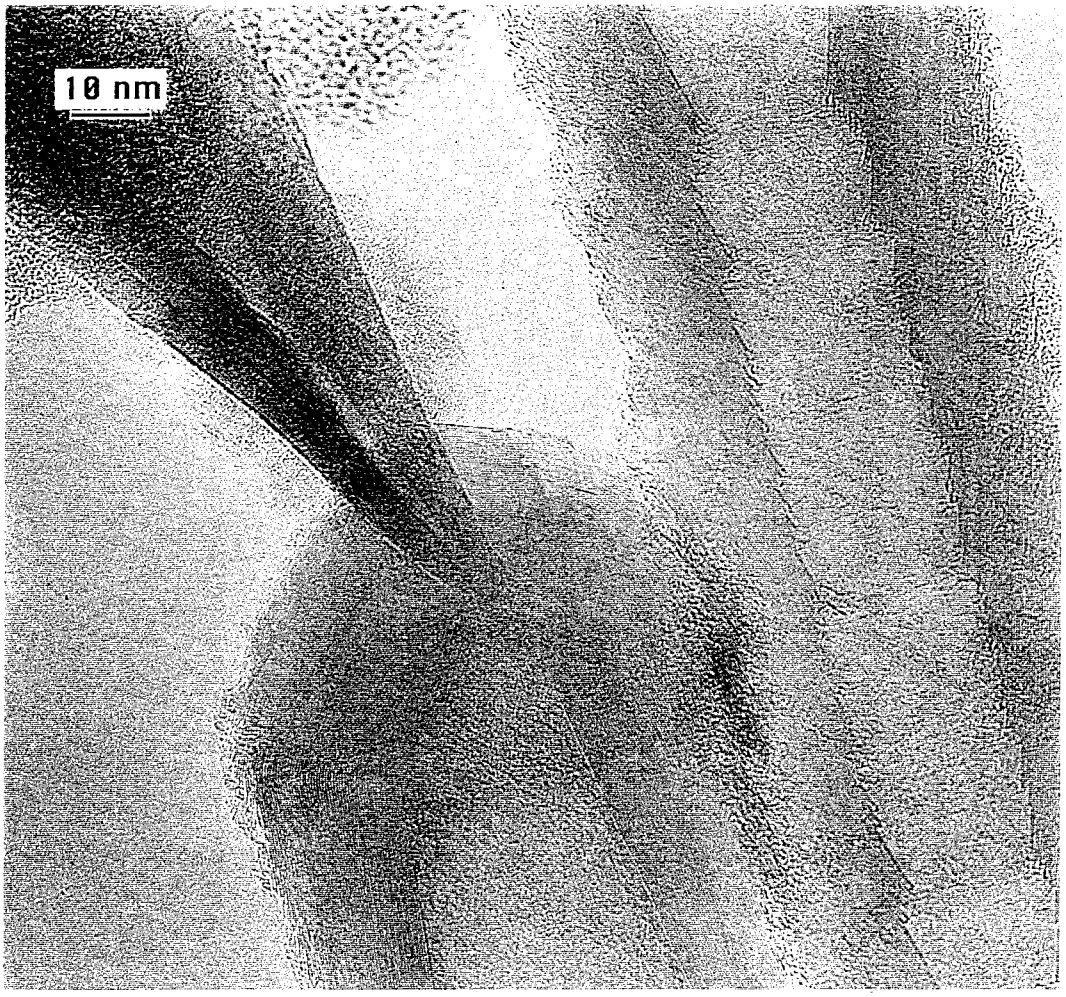

Figure 6.18: Carbon cone found in the rubbery soot, made with Co and S.

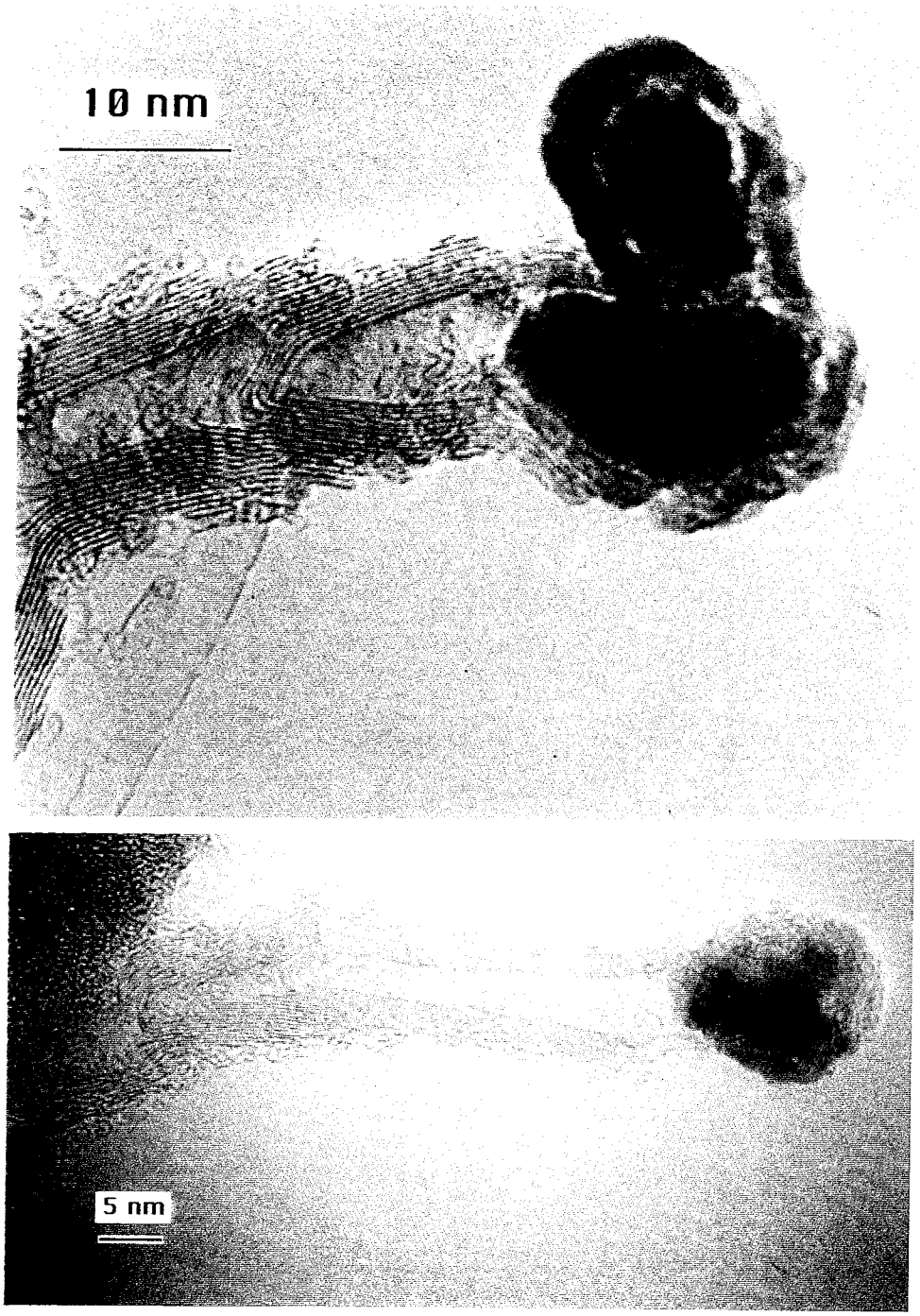

Figure 6.19: Carbon nanofibers in the soot around the cathode, when Co and S were added to the anode. The particles at the end of the fibers are cobalt sulfide crystals.

a composition of S, Co, and C. Selected area diffraction reveals the material to be crystalline. We identified it as a cobalt sulfide crystal, but further analysis is needed to verify the exact crystal composition.

Apparent in Figure 6.17 is a string of beads connected to the conical graphite filaments. At a high magnification, we can see from Fig. 6.20 that these triangle beads have comparable shapes and sizes throughout the chain. Each pyramidal segment comprises layers of graphene sheet at a spacing comparable to that of bulk graphite. Note that in Fig. 6.17 the filament seems to grow out of the the string, suggesting that a common catalytic particle for these two structures and a similar growth mechanism.

There are also carbon fibers with bamboo-like sections that link to a chain of carbon fiber. Figure 6.21 displays the portion where the tilted graphite cones joined to form a compartment-like fiber structure. The bamboo-like structure has been found in the cathode deposit when using a Ni/C composite bar as the anode [34]. Ni has a catalytic effect on the nanotube growth similar to that of Co, but no bamboo-like structures were found when using Co alone without the aid of S in an arc chamber. By incorporating sulfur, however, we were able to enhance the catalytic effect of Co for the growth of various carbon structures that are otherwise too insignificant to be observed.

Some of these compartments contain catalyst particles, either at the end or at the middle of the chain, as shown in Fig. 6.21. Figure 6.22a is the high resolution TEM image of the crystallite at the tip of the chain in Figure 6.21, with a lattice spacing of 4.9 Å clearly seen. EDS (Fig. 6.22b) and selected area diffraction pattern indicate that this particle is a cobalt sulfide crystal, perhaps Co_9S_8 or β-CoS. Filling of the tubes has also been observed, and the lengths of fill range from a few tens of nanometers (Fig. 6.23a) to several hundred nanometers (Fig. 6.23b). Figure 6.23c shows two partially filled sections of tubes. These structures are similar to the manganese-filled carbon nanofibers grown in the vapor phase [35]. The proposed growth model, which

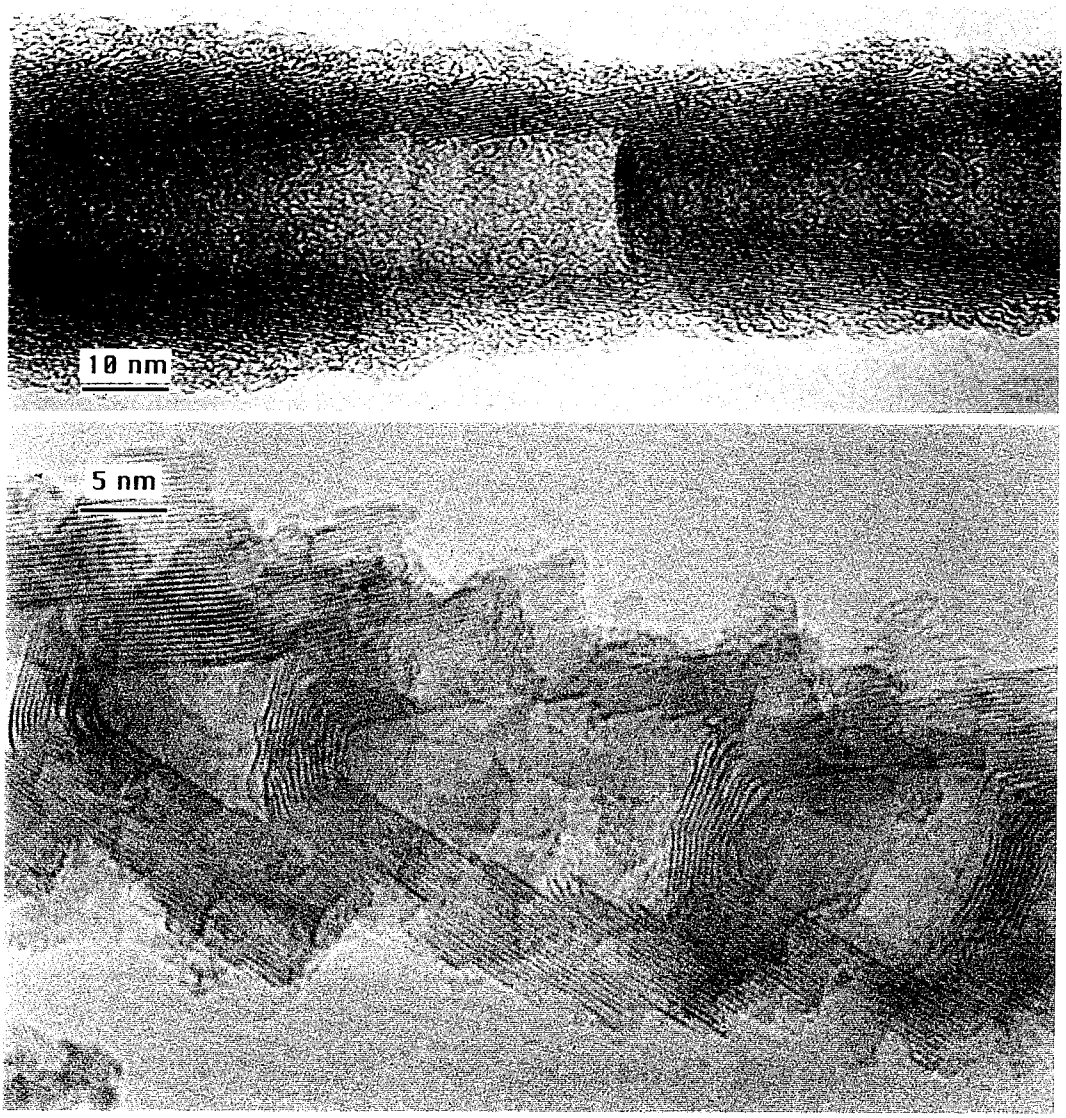

Figure 6.20: String of pyramidal shaped carbon beads, found in the rubbery soot.

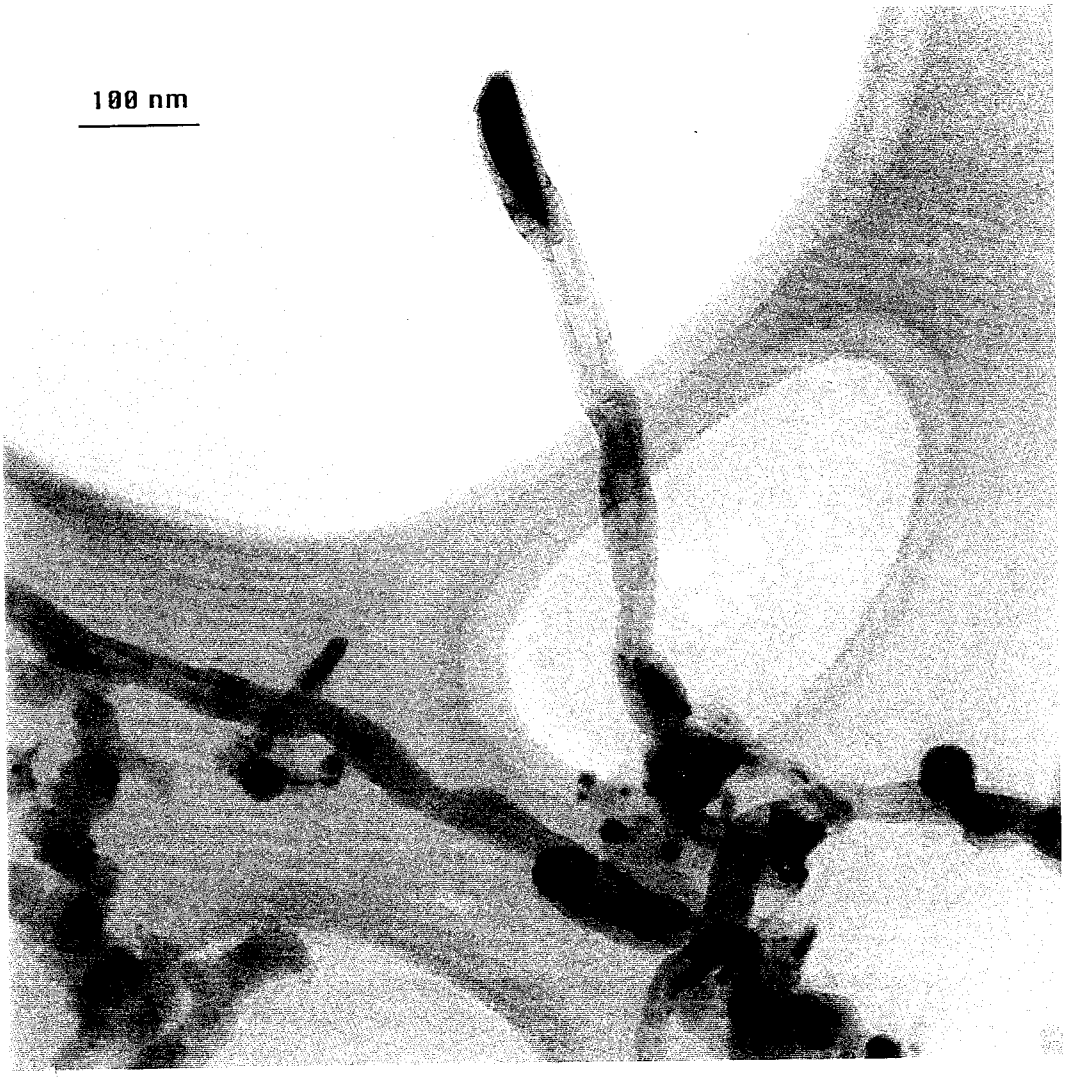

Figure 6.21: The bamboo-like carbon structures form abundantly in the rubbery deposit around the cathode when sulfur was added.

(a)

(b)

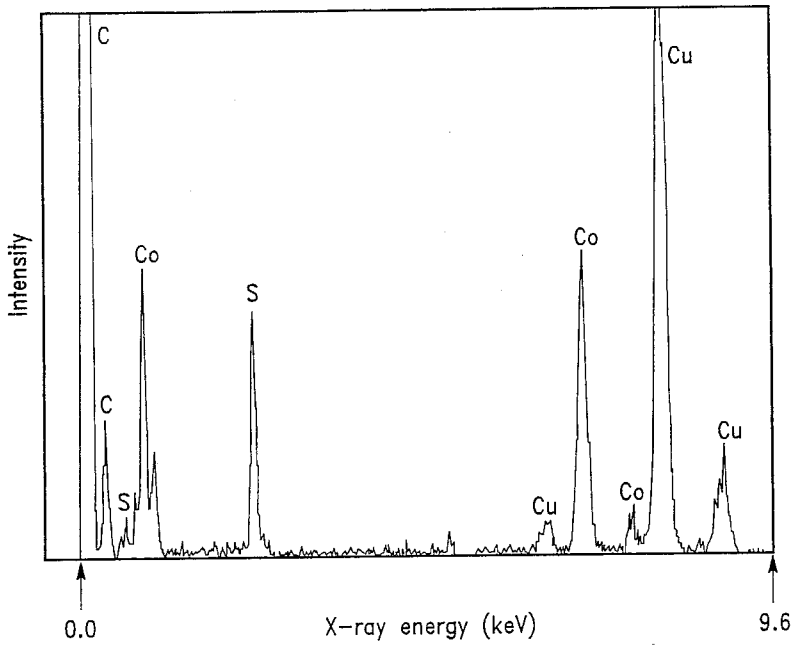

Figure 6.22: (a) High resolution TEM of the crystal in the nanocompartment. (b) EDS of the crystal (a).

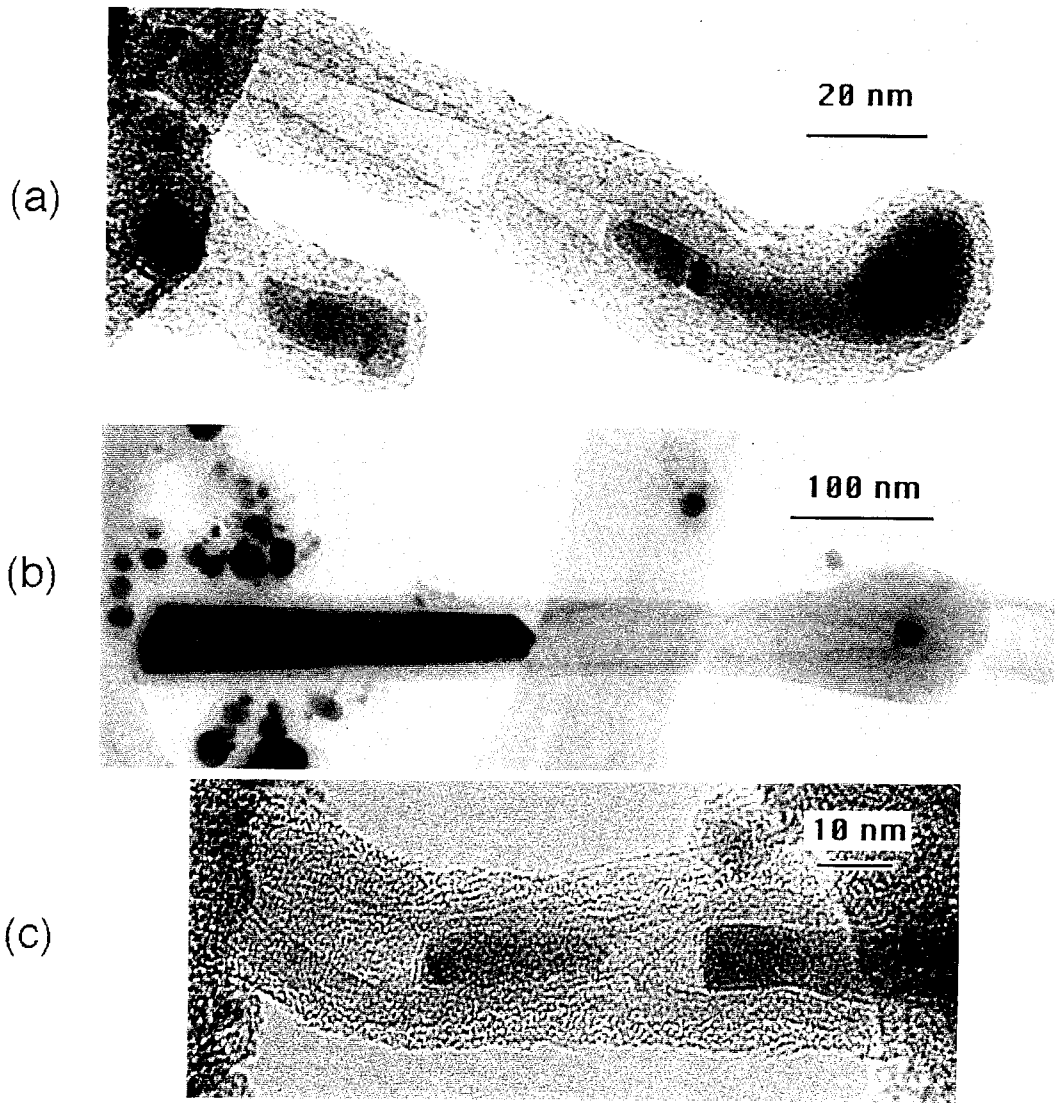

Figure 6.23: Filling of nanotubes. (a) Many of the ends of the carbon compartments contains cobalt sulfide. (b) Crystalline cobalt sulfide filled tube, with the filling more than 100 nm long. (c) Two sections in the middle of the strings of bead partially filled with cobalt sulfide.

regards the encapsulations as catalysts and attributes the lengthy filling from the simultaneous deposition of carbon and metal vapor, may be applicable here [35].

That such a variety of carbon structures appear in the rubbery soot around the cathode gives us clues about the growth of the carbon networks. We know that in this region the electric field and the temperature are not as high as those near the center of the electrode, where carbon nanotubes can grow without a catalyst. The presence of Co and S, however, make it possible for the multilayer carbon nanotubes to form in this region. The large temperature gradient in the arc may be important to the nanotube growth. The crystal structure of Co provide clues to the temperature history in the arc. The Co particles in the soot on the walls are *fcc*-Co, which is the high temperature phase ($>$ 690K), indicating the metal is rapidly quenched and not annealed to its thermodynamically most stable form at room temperature. Conversely, the Co crystals on the cathode deposit are predominately the stable form, *hcp*-Co. Compared to the soot deposit on the wall, this deposit stayed in the region with sustained high temperature and carbon vapor density and was annealed gradually.

According to the multi-layer nanotube growth mechanism proposed by Iijima *et al.* [16], the key to the tube growth in the center of the arc is the open end. It was suggested that the electric field in the arc, which generates ionic species and keeps the tube end open, is crucial to the construction of the tubes [30, 31]. The growth of multilayer nanotubes outside the arc center should, therefore, rely on the chemical properties of the additives Co and S. The catalytic properties of Co and S in the gas phase formation of single-layer nanotubes may play an important role in the multilayer tube growth in this region. They could assist the growth by keeping the ends open and by enhancing the reaction rate. Since sulfur does not catalyze the tube growth by itself, we speculate that sulfur keeps the tube ends open, perhaps by stabilizing the dangling bonds and prevents the bonds from reconstructing to cause

tube closure. The cobalt or cobalt carbide species, on the other hand, expedite the carbon transport and facilitate the carbon sp^2 network formation.

6.5 The Metal Particles

The encapsulated ferromagnetic particles produced by this process may eventually be of technological interest, for example in the field of magnetic storage media. Some work characterizing the magnetic properties of the encapsulated Co particles produced by arc co-evaporation with carbon has been recently reported [36]. The phase and composition of the metal-containing particles may also provide information about the growth conditions in the reactor. The temporal and spatial profiles of temperature, metal and carbon densities, and reaction rates all affect the growth of both these particles and the nanotubes. The composition of the metal containing particles in the soot deposited away from the electrode is not the same as for those found in the cathode deposit. For iron group metals, pure metallic particle as well as cementite phases (Fe_3C, Co_3C, and Ni_3C) exist in the outer surface of the cathode deposit [34]. These particles appear spherical and are wrapped with layers of graphene sheet with no gaps. The low temperature phases, α-Fe and α-*hcp*-Co, form abundantly, whereas the high temperature phases, β-Fe and β-*fcc*-Co, are found in less than 10% of the metal particles. In contrast, the metal particles found in the soot on the chamber wall contain mostly high temperature phases such as Fe_3C [22], *fcc*-Co [27, 37] and *fcc*-Ni [34], and not all of the particles are wrapped in graphitic layers. The crystalline material in the soot made with Co and Co+S soot are similar, with *fcc*-Co the dominant phase. These findings imply that as the particles move away from the arc they are rapidly quenched, which might be a crucial feature of the growth of single-layer carbon nanotubes.

The presence of S, Bi, and W induces the formation of graphitic carbon shells

around cobalt-containing particles, so that cobalt particles encapsulated in graphitic polyhedra are found throughout the soot along with the single-layer nanotubes. Figures 6.24a to 6.24c are high resolution images of some encapsulated Co particles, which have structures reminiscent of those observed for LaC_2 and YC_2 particles found in cathode deposits [38, 39, 40]. Crystallites encapsulated in graphitic polyhedra are about 30% of the total Co particles with the addition of sulfur and about 10–20% with the addition of bismuth or tungsten.

6.6 Conclusions

We have produced various carbon nanomaterials by using an arc. We have studied these structures primarily with transmission electron microscopy. Additional studies were carried out with X-ray diffraction and energy dispersive spectroscopy. The morphology of the catalytically produced nanotubes is different from that of tubes grown on the cathode tip. The structures of the ends of single-layer nanotubes, however, are similar to those of multilayer nanotubes. A common growth mechanism consisting of building a honeycomb network on the open end of the tube is believed to be operative in both cases. Detailed atomic structure of the single-layer nanotubes were also obtained, despite the extremely weak electron diffraction intensity.

Nanotube structural transformations induced by electron beam heating were discussed. Nanotubes could be either destroyed or repaired, depending on the conditions. The bundling of nanotubes was observed in real time. The time scale of the transformations was seconds, very long for a molecular motion.

Diverse structures such as nanocompartments, multilayer nanotubes, and nanofibers were produced catalytically. They were found in the rubbery deposit around the cathode when both cobalt and sulfur were vaporized together with carbon. The special environment in the region (*e.g.* the temperature and carbon density distribution),

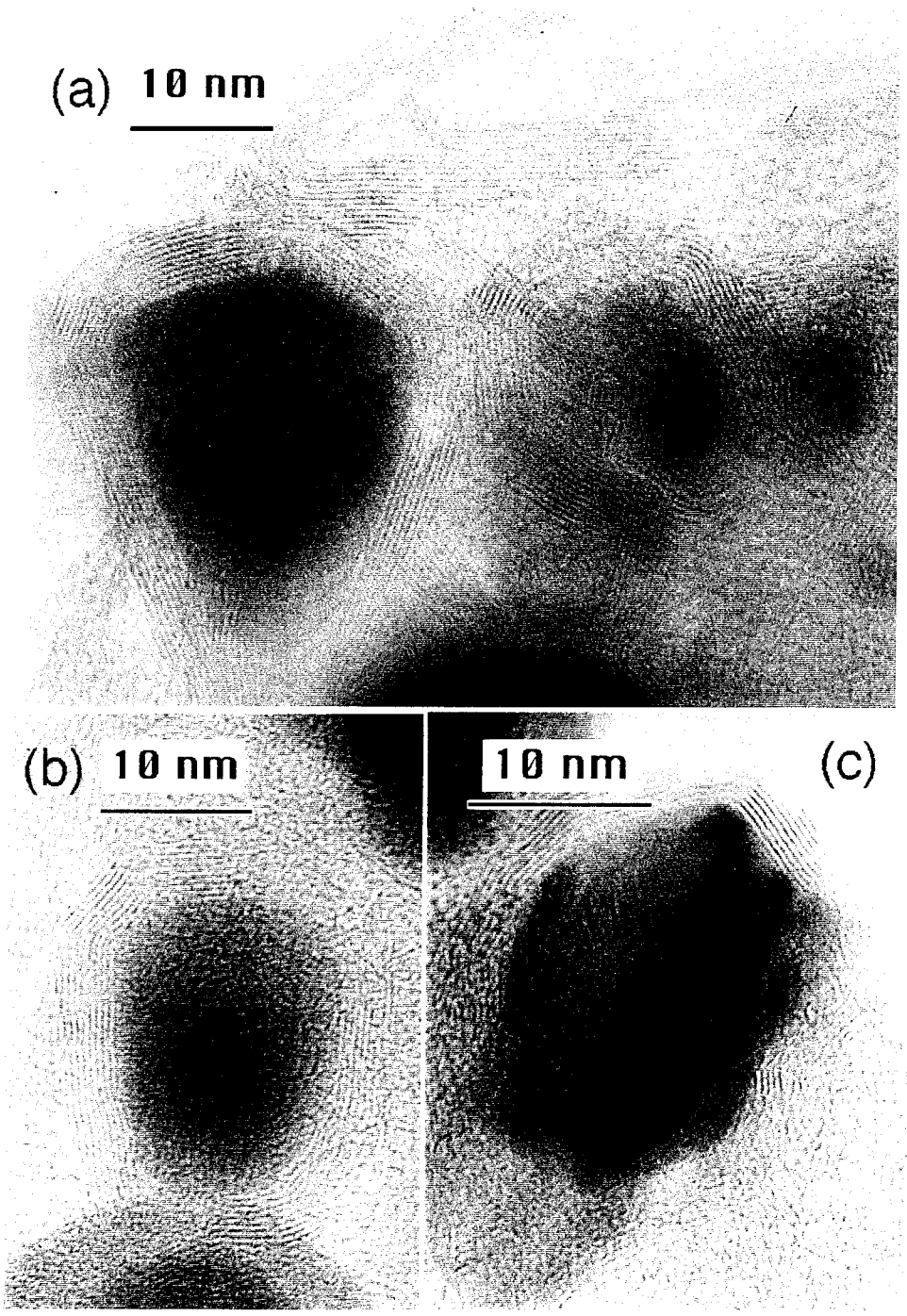

Figure 6.24: Cobalt-filled graphitic polyhedra found in soot produced with an anode containing Co and (a) S, (b) Bi, and (c) W.

and the catalytic properties of Co and S, are vital to the growth of these structures. Filling of the nanotubes and nanocompartments with metals or metal compounds was also achieved when sulfur was incorporated as the source material. Metal crystal encapsulated graphitic polyhedra also formed abundantly when sulfur, bismuth, or tungsten were present. These additives apparently modify the metal chemistry so that the carbon grows around the metal, producing nanowires or nanoparticles encased in graphitic layers.

References

[1] S. Iijima, Nature **354**, 56 (1991).

[2] R. Saito, M. Fujita, G. Dresselhaus, and M. S. Dresselhaus, Matls. Sci. and Eng. B **19**, 185 (1993).

[3] J. W. Mintmire, D. H. Robertson, and C. T. White, J. Phys. Chem. Solids **54**, 1835 (1993).

[4] R. Saito, M. Fujita, G. Dresselhaus, and M. S. Dresselhaus, Phys. Rev. B **46**, 1804 (1992).

[5] M. S. Dresselhaus, G. Dresselhaus, and R. Saito, Solid State Commun. (USA) **84**, 201 (1992).

[6] R. A. Jishi, D. Inomata, K. Nakao, M. S. Dresselhaus, and G. Dresselhaus, J. Phys. Soc. Jpn. (Japan) **63**, 2252 (1994).

[7] N. Hamada, S.-I. Sawada, and A. Oshiyama, Phys. Rev. Lett. **68**, 1579 (1992).

[8] R. A. Jishi and M. S. Dresselhaus, Phys. Rev. B **45**, 11305 (1992).

[9] R. A. Jishi, L. Venkataraman, M. S. Dresselhaus, and G. Dresselhaus, Chem. Phys. Lett. **209**, 77 (1993).

[10] J. M. Holden, P. Zhou, X.-X. Bi, P. C. Eklund, S. Bandow, R. A. Jishi, K. Das Chowdhury, G. Dresselhaus, and M. S. Dresselhaus, Chem. Phys. Lett. **220**, 186 (1994).

[11] R. Kuzuo, M. Terauchi, M. Tanaka, and Y. Saito, Jpn. J. Appl. Phys. 2. Lett. **33**, L1316 (1994).

[12] S. Iijima, T. Ichihashi, and Y. Ando, Nature **356**, 776 (1992).

[13] M. Endo, Chemtech **18**, 568 (1988).

[14] G. G. Tibbetts, Carbon **27**, 745 (1989).

[15] R. T. K. Baker, Carbon **27**, 315 (1989).

[16] S. Iijima, P. M. Ajayan, and T. Ichihashi, Phys. Rev. Lett. **69**, 3100 (1992).

[17] P. W. Fowler, J. Phys. Chem. Solids (UK) **54**, 1825 (1993).

[18] R. de Wit, J. Appl. Phys. **42**,3304 (1971).

[19] P. M. Ajayan, T. Ichihashi, and S. Iijima, Chem. Phys. Lett. **202**, 384 (1993)

[20] S. Iijima, Mater. Sci. Eng. **B 19**,172 (1993)

[21] M. Ge and K. Sattler, Chem. Phys. Lett. **220**, 192 (1994)

[22] S. Iijima and T. Ichihashi, Nature **363**, 603 (1993).

[23] X. F. Zhang, X. B. Zhang, G. Van Tendeloo, S. Amelinckx, M. Op de Beeck, and J. Van Landuyt, J. Crystal. Growth **130**, 368 (1993).

[24] J. Milliken, T. M. Keller, A. P. Baronavski, S. W. McElvany, J. H. Callehan, and H. H. Nelson, Chem. Mater. **3**, 386 (1991).

[25] D. Ugarte, Nature **359**, 707 (1992).

[26] R. S. Ruoff, J. Tersoff, D. C. Lorents, S. Subramoney, and B. Chan, Nature **364**, 514 (1994).

[27] D. S. Bethune, C.-H. Kiang, M. S. de Vries, G. Gorman, R. Savoy, J. Vazquez, and R. Beyers, Nature **363**, 605 (1993).

[28] C.-H. Kiang, W. A. Goddard III, R. Beyers, J. R. Salem, and D. S. Bethune, J. Phys. Chem. **98**, 6612 (1994).

[29] S. Seraphin and D. Zhou, Appl. Phys. Lett. **64**, 2087 (1993).

[30] D. T. Colbert, J. Zhang, S. M. McClure, P. Nikolaev, Z. Chen, J. H. Hafner, D. W. Owens, P. G. Kotula, C. B. Carter, J. H. Weaver, A. G. Rinzler, and R. E. Smalley, Science **266**, 1218 (1994).

[31] A. Maiti, C. J. Brabec, C. M. Roland, and J. Bernholc, Phys. Rev. Lett. **73**, 2468 (1994).

[32] M. Audier and M. Coulon, Carbon **23**, 317 (1985).

[33] R. Bacon, J. Appl. Phys. **31**, 283 (1960).

[34] Y. Saito, T. Yoshikawa, M. Okuda, N. Fujimoto, K. Sumiyama, K. Suzuki, A. Kasuya, and Y. Nishina, J. Phys. Chem. Solids **54**, 1849 (1993).

[35] P. M. Ajayan, C. Collies, J. M. Lambert, P. Bernier, L. Barbedette, M. Tencé, and O. Stephan, Phys. Rev. Lett. **72**, 1722 (994).

[36] M. E. McHenry, S. A. Majetich, J. O. Artman, M. DeGraef, and S. W. Staley, Phys. Rev. B **49**, 11358 (1994).

[37] S. A. Majetich, J. O. Artman, M. E. McHenry, N. T. Nuhfer, and S. W. Staley, Phys. Rev. B **48**, 16845 (1993).

[38] R.S. Ruoff, D.C. Lorents, B. Chan, R. Malhotra, and S. Subramoney, Science **259**, 346 (1993).

[39] Y. Saito, T. Yoshikawa, M. Okuda, M. Ohkohchi, M. Inagaki, Y. Ando, A. Kasuya, and Y. Nishina, Chem. Phys. Lett. **209**, 72 (1993).

[40] S. Seraphin, D. Zhou, J. Jiao, J. C. Withers, and R. Loutfy, Appl. Phys. Lett. **63**, 2073 (1993).

Chapter 7

Growth Model for Single-Layer Carbon Nanotubes

7.1 Introduction

The ability to grow carbon nanotubes by a catalytic route is crucial for exploration of new production schemes and potential applications of these materials. Nanotubes form readily in an electric arc without a catalyst, but they have a wide range of diameters, lengths, and the number of carbon shells [1, 2]. Catalysts and promoters have been discovered that greatly improve the carbon nanotube yield and final product selectivity, as described in Chapters 5 and 6 [3, 4, 5]. Such increased production efficiency and specificity is vital if the nanotube field is to progress. Study of the catalytic growth mechanism is, therefore, essential for further synthetic progress as well as for gaining an understanding of the gas-phase self-assembly of this novel carbon molecule.

Growth models for related carbon nanotube structures, such as the vapor phase grown carbon fibers and the multilayer nanotubes, have been proposed [6, 7, 8, 9, 10].

Single-layer carbon nanotubes grown by the Co catalyst, however, have unique features that are distinct from those of the vapor grown carbon fibers and the multilayer nanotubes formed on the cathode tip. For example, single-layer nanotubes are found in the soot on the chamber wall, intertwined with the fullerenes and non-crystalline carbon that are also generated. They are almost exclusively single-layered, and they often have a structured diameter distribution. These observations strongly suggest that a different growth mechanism is responsible for the single-layer nanotube growth.

Transition metal particles are used to produce carbon fibers in the vapor phase by hydrocarbon decomposition on the metal particles. The fibers typically have lengths of cm, and diameters of μm. The fibers usually terminate with catalyst particles at the fiber tip [11]. The growth model for these carbon fibers involves carbon diffusing on the metal particle surfaces and forming layers of graphene tubes surrounding the particles [6, 7, 8]. This is in contrast to the nanotubes produced catalytically in the arc, which do not have metal particles at the tip of the tubes [4, 12]. The catalytic species, therefore, must depart after the closure of the nanotubes, which favors the hypothesis that small metal clusters are the catalyst in nanotube formation.

Small metal clusters are known to have interesting catalytic properties in the gas phase. For example, Fe_4^+ has been found to be an active center that forms benzene precursors [13]. Co clusters, Co_n^+ (n = 1, 3, 4), react with cyclohexane to produce C_6H_6 bound to the metal cluster in the gas phase [15]. We suspect that small Co clusters formed in the arc play an important role in catalyzing the nanotube formation. We detail our mechanistic arguments in this chapter.

7.2 Experimental Observations

There remains a major puzzle as to what controls the growth of these nanotubes and why additional layers are not formed. The reaction conditions in the electric arc

environment currently used for nanotube production are non-ideal for mechanistic studies, since the plasma composition near the arc is very complex. This makes it difficult to isolate the effects of each parameter. To date we can only examine the final product in an effort to extract clues about the growth mechanism. One feature that can be analyzed is the diameter distribution of single-layer carbon nanotubes. Table I lists the results available so far, summarizing the discussion of Chapters 5 and 6 as well as others. Figure 7.1 illustrates the range of single-layer nanotube diameters produced by different procedures. These results should be considered illustrative only, due to the errors that arise from statistical uncertainties and the variations in the reaction conditions employed.

One of the most interesting features available from the accumulated data is the diameters of the tubes. The diameters produced by the various metals and combinations of metals all lie in the range of 1 to 2 nm. The addition of S, Pb, or Bi, on the other hand, produces considerably larger diameter tubes, although the main peak in the distribution is still located between 1 and 2 nm. Figure 7.2a to 7.2c present histograms of the abundance of different diameter nanotubes produced with Fe, Co, and Co+S, adapted from earlier reports [4, 14]. The diameter distributions produced using Co and Co+S are very similar both in overall maxima and in fine structures (Figs. 7.2b and 7.2c, respectively). For the cases where large diameter tubes (> 3 nm) are produced by adding S, Pb or Bi to Co, the tubes are still exclusively single-layered. We observed only one double-layer nanotube out of over 2000 tubes imaged. This suggests that nucleation of additional layers must be strongly inhibited. The stability of nanotubes of various diameters has been investigated theoretically via classical mechanical calculations [22, 23]. The tube energies are predicted to vary smoothly with diameter, with larger diameter tubes more stable than smaller ones. The narrow diameter distributions and the occurrence of only single-layer tubes point to the importance of growth kinetics rather than simply energetics in the nanotube

Table 7.1: Results on single-layer nanotubes.[a]

Elements	D(nm)	D_{peak}(nm)	P (Torr)	I (A)	V_0 (V)	D_E(mm) an./cat.	Ref.	note
Fe	0.7–1.6	0.80,1.05	50[b]	200	20	10/20	[14]	*c*
Fe	0.6–1.3	0.7–0.8	100/550	75	27	6/9	[16]	*d*
Co	0.9–2.4	1.3,1.5	300–400	95	25	6/6	[4]	*e*
Co	1–2	1.2–1.3	150	100	25	6/9	[17]	*e*
Co	0.6–1.8	–	100/550	75	27	6/9	[16]	*d*
Ni	1.2–1.5	–	100–600	70	25	6/10	[18]	
Ni	0.6–1.3	0.7–0.8	100/550	75	27	6/9	[12]	*d*
Fe+Ni	0.9–3.1	1.7	550	75	27	6/9	[16]	*f*
Fe+Ni	>0.6	1.3–1.8	100/550	75	27	6/9	[16]	*d*
Co+Ni	>0.6	1.2–1.3	100/550					
Co+S	1.0–6.0	1.3, 1.5	300–400	95	25	6/6	[4]	*g*
Co+Bi	0.8–5.0	1.2, 1.5	300–400	75	25	6/6	[5]	*h*
Co+Pb	1.0–4.0	1.5	300–400	95	25	6/6	[5]	*i*
Co+Pt	~ 2	–	150–500	100	25	6/16	[19]	
Y	1.1–1.7	–	100/550	75	27	6/9	[16]	*j*
Cu	1–4	–	50–760	50–300	10–30	13/25	[20]	*k*
no metal	> 2	–	–	–	–	–	[21]	*l*

[a]Unless specified, samples were from soot deposited on the chamber wall, and the buffer gas was helium. The elements are incorporated in the graphite anode, D is the nanotube diameter range, and D_{peak} is the most abundant nanotube diameter. The nanotube diameters were obtained from high resolution TEM images. [b]10 Torr CH_4+40 Torr Ar. [c]Statistics from over 60 tubes. [d]Statistics from 40 tubes, and with 10% error. [e]Statistics from over 100 tubes. [f]Statistics from 70 tubes. [g]Statistics from over 300 tubes. [h]Statistics from over 150 tubes. [i]Statistics from over 200 tubes. [j]Nanotubes grew radially out of YC_2 crystals, 15–100 nm long. [k]Nanotubes found in the cathode deposit, 3–40 nm long. [l]Nanotubes formed by benzene pyrolysis on graphite substrate.

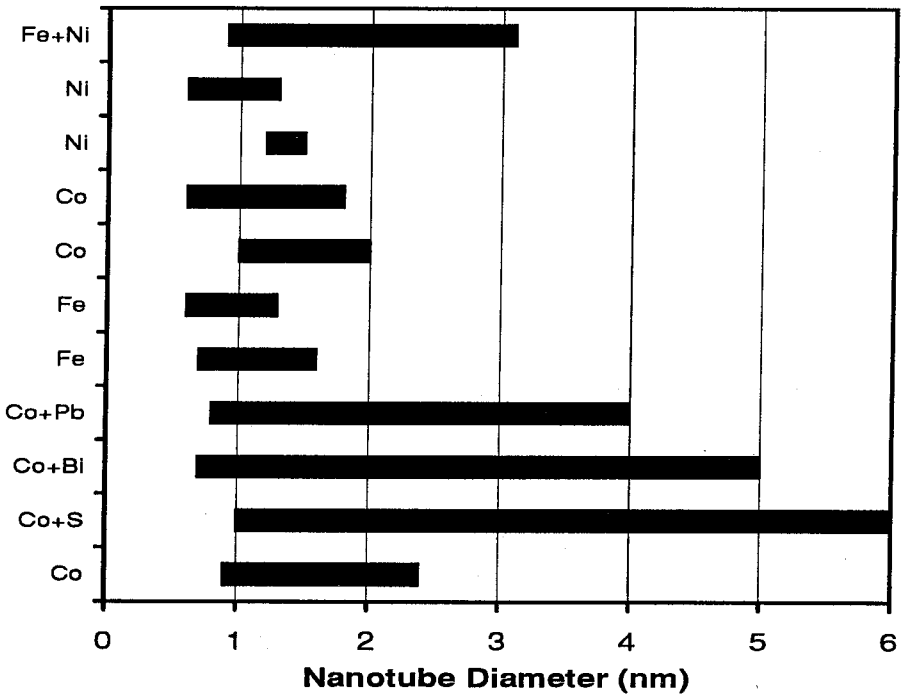

Figure 7.1: Ranges of nanotube diameters produced by using different catalyst and promoters.

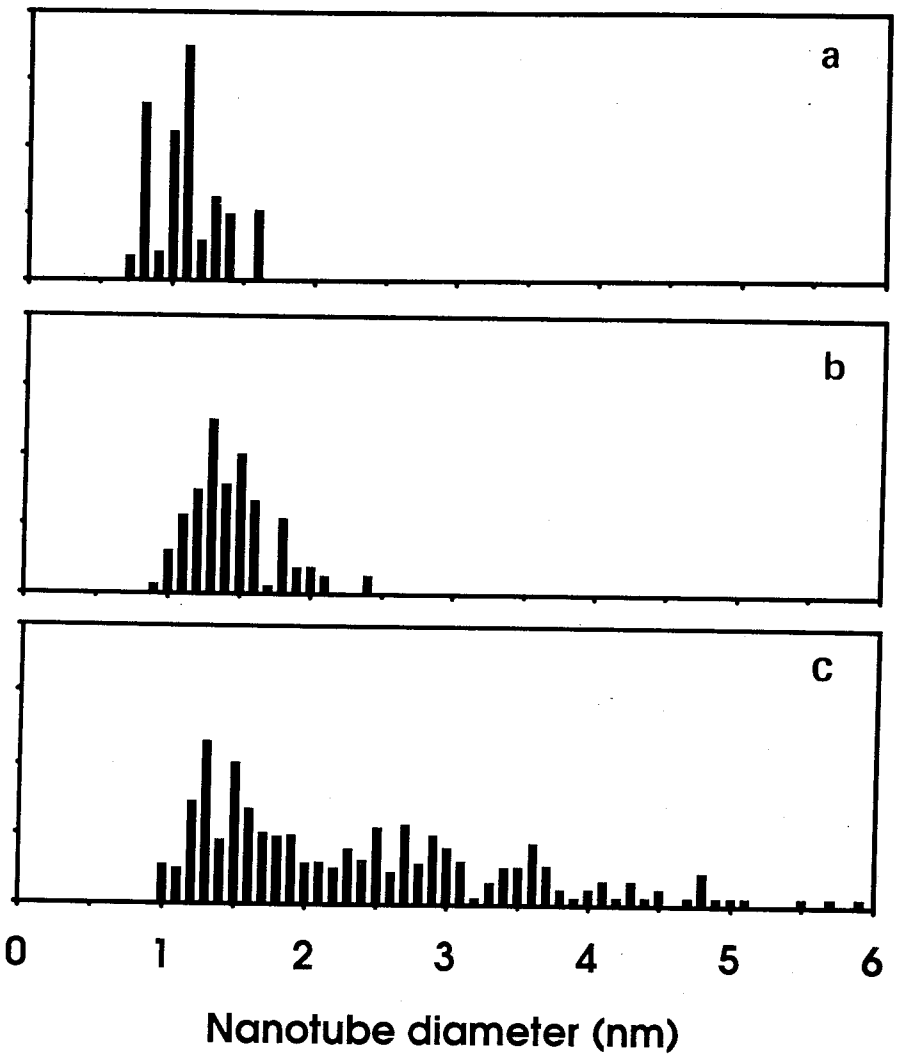

Figure 7.2: Diameter distribution of nanotubes produced via different methods: (a) Fe catalyst in an Ar/CH_4 atmosphere, adapted from Ref. [14]; (b) Co catalyst in He atmosphere, adapted from Ref. [4]; (c) Co catalyst with sulfur, about 4% each, adapted from Ref. [4].

formation process.

S, Bi, and Pb affect the Co-catalyzed production of single-layer nanotubes by greatly increasing the yield and the maximum diameter of the nanotubes. The formation of web-like material in the chamber is dramatically enhanced. These elements do not produce nanotubes without a metal catalyst, but they significantly increase the yields when Co is present. These elements may act as co-catalysts that interact with Co to catalyze the reaction or as promoters that help in stabilizing the reactants or simply as scavengers that remove blocking groups that inhibit tube growth.

Some features in the arc process are known and are relevant to the growth mechanism for single-layer nanotubes. Earlier isotope labeling analyses of fullerene formation show that fullerenes formed in the arc are built up from atomic carbon [24, 25, 26]. Also, as discussed in Chapter 5, the production of nanotubes does not seem to depend on whether metal oxide or pure metal is used in the graphite anode. These results imply that both the metal and the carbon are atomized under the arc conditions and that both the catalytic species and the nanotubes must be built up from neutral or ionic atoms. The sharp variation of the abundance as a function of tube diameter suggests the importance of growth kinetics.

7.3 Previous Growth Models

Incorporation of carbon dimers into a cage-like precursor has been considered to be a route to the growth of single-layer carbon nanotubes [27, 28, 29]. According to this model, C_2 clusters are absorbed near a pentagonal ring of fullerene molecules, and helical tubules are formed with repeated C_2 addition. In this model the tubule grows from an empty fullerene cage. Since the growing tubule is always closed, there is no mechanism to enclose materials into the tubule. This mechanism is in conflict with the evidence of carbonaceous material encapsulated in the nanotubes (see Fig.

7.3a). Figure 7.3b shows another example of a nanotube encapsulating carbonaceous materials. A section of a nanotube has been expanded radially due to the amorphous material inside, which strongly suggests that the material was included in the tube during the growth. We conclude that the material inside the tube must have been captured during the growth, and only a model with an open growing end is consistent with the data. Growing by C_2 addition to a tube cap, however, may explain the formation of single-layer nanotubes that grow radially out from a catalyst particle [16, 30, 31].

Multilayer nanotubes, on the other hand, share some common characteristics with single-layer nanotubes produced by the cobalt catalyst. Both processes utilize an arc under helium atmosphere, with a temperature estimated to be 3000 ° C [10], and atomic (ionic or neutral) carbon vapor is the elemental source. The differences lie in the regions where the tubes are formed. The nanotubes produced without catalyst are only found in the center of cathode tip deposit, whereas the tubes grown by the catalyst are found on the cold chamber walls together with fullerenes. The growth model proposed for these multilayer nanotubes says the tubes grow at the open end, which has many dangling bonds. These tubes usually have large diameters (> 3 nm), which is considered to be important in preventing the tube from closing in a strong electric field [32]. The catalyst appears to enhance the construction of carbon tubules by keeping the end open while allowing an efficient supply of the carbon species vital to the growth.

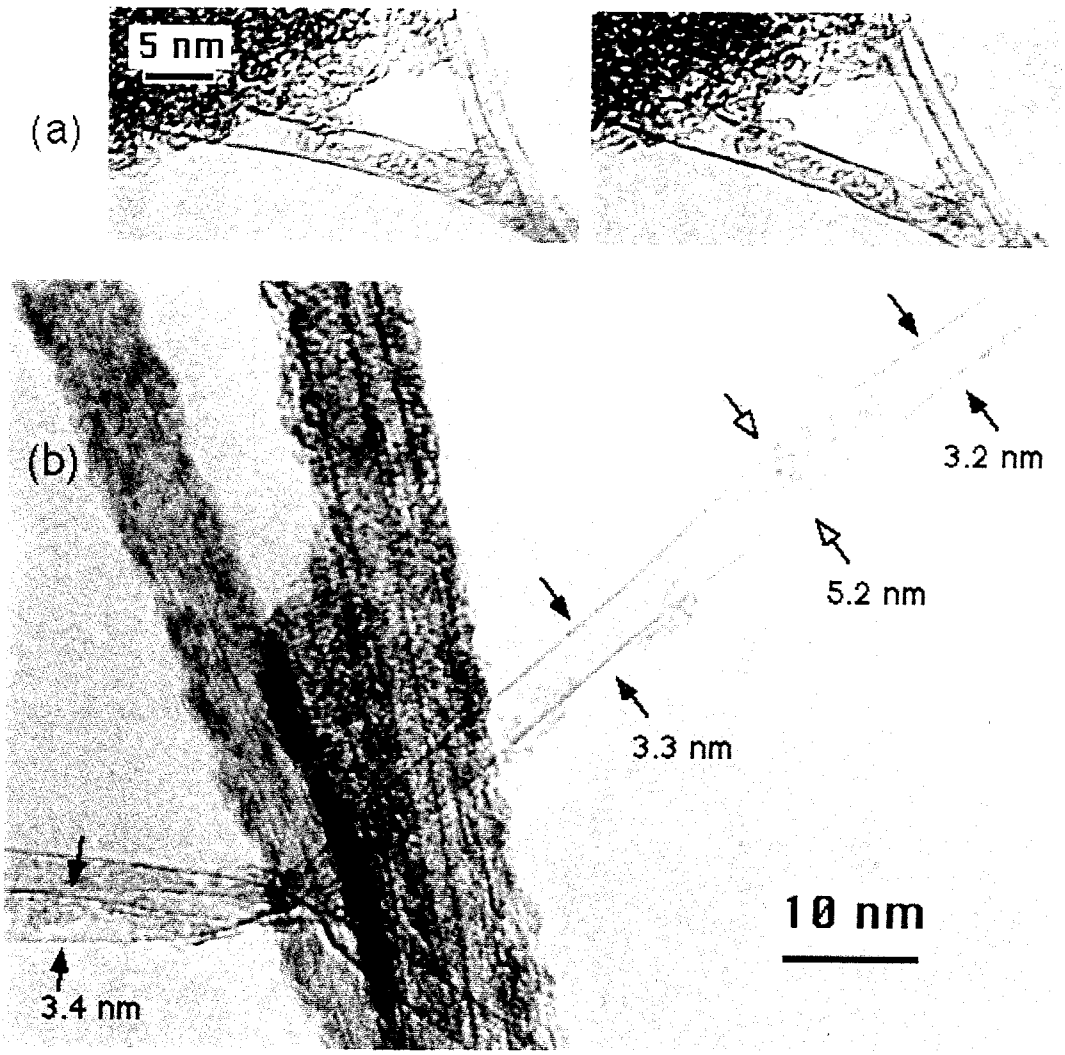

Figure 7.3: (a) A nanotube with carbonaceous material inside. The sample was rotated to verify that the amorphous material was indeed inside the tube. (b) A nanotube with material that expanded the tube wall, suggesting that the material was incorporated during the growth.

7.4 The Growth Model for Catalytically Grown Single-Layer Nanotubes

One unique feature of the catalytically grown single-layer nanotubes is the structured diameter distribution. The diameter distribution shows sharp variations, which are not understood in terms of tube stability [22, 23] or catalytic particle size [4]. Different catalyst promoters increased total yield, but the tubes produced have similar diameter distributions, concentrating between 1 and 2 nm [4, 5, 33] and with similar fine structure. The variation in the abundance is at the molecular scale. We suggest that the nanotube precursors are generated in the arc. We believe these building blocks are carbon rings, which have been observed in laser generated carbon plasmas.

Recent studies of carbon clusters suggested that planar carbon rings are possible fullerene precursors [34, 35, 36]. The carbon vapor aggregates to form linear carbon chains C_n for $n < 10$, planar rings for $10 < n < 40$, and spheroidal fullerenes for $n > 40$ [35, 36, 37]. Figure 7.4 shows the abundances of different carbon cluster isomers and Fig. 7.5 shows the nanotube diameter distribution [35]. Planar carbon rings are the dominate isomer for n = 20 to 40, and stable fullerene species are more abundant for n > 50. The diameter of a nanotube that grew from a carbon ring would correspond to the ring size. For example, a carbon nanotube grown from a monocyclic ring composed of 30 carbon will have a diameter of 1.3 nm, provided that the helicity is zero. The nanotube diameter is most abundant between 1 and 2 nm, which corresponds to between 22 and 44 carbons at the circumference. This leads us to hypothesize that the nanotubes grow from monocyclic carbon rings, which are also a precursor for fullerenes. The structured distribution of the nanotube abundance results from the competing reaction channels that lead to either spheroidal fullerenes or cylindrical tubules.

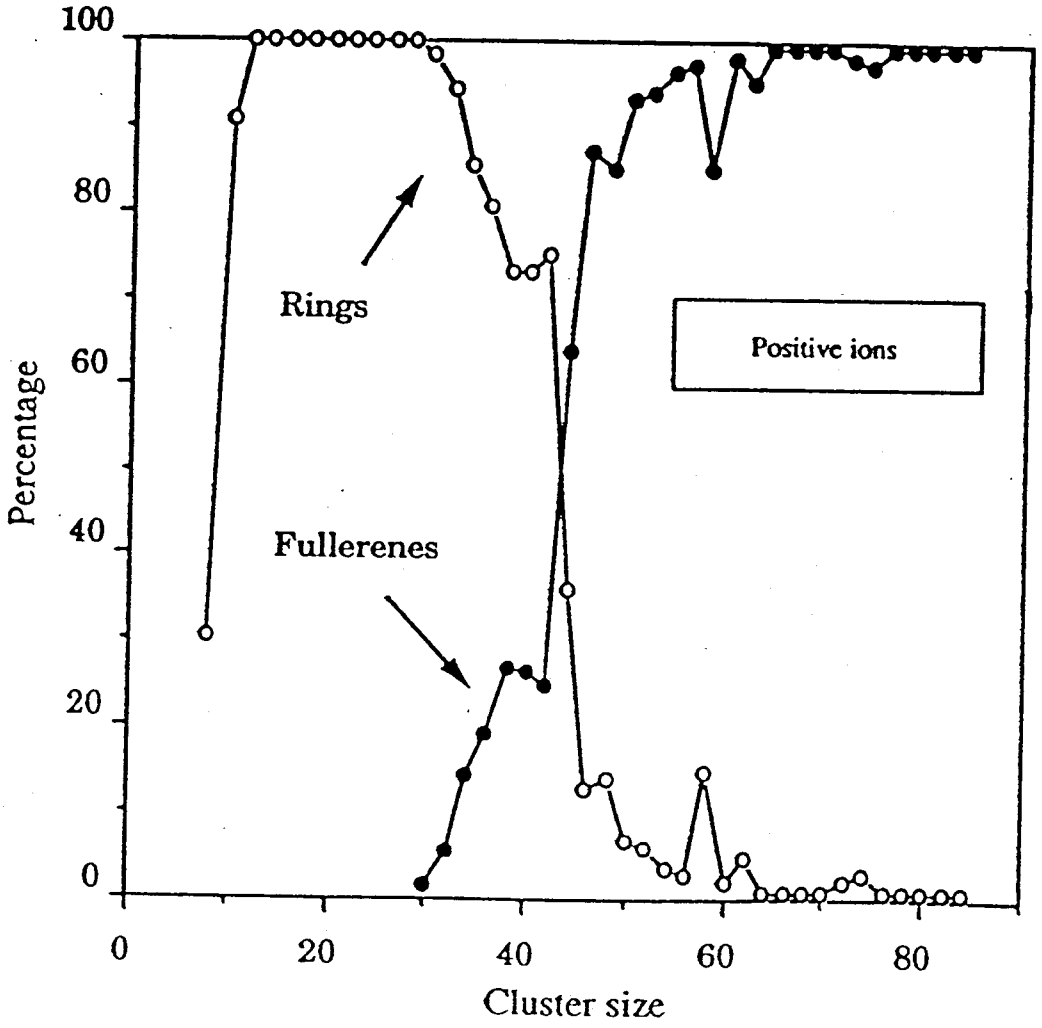

Figure 7.4: Plots of percentage of planar carbon rings and fullerenes as a function of carbon cluster size (from Ref. [35]).

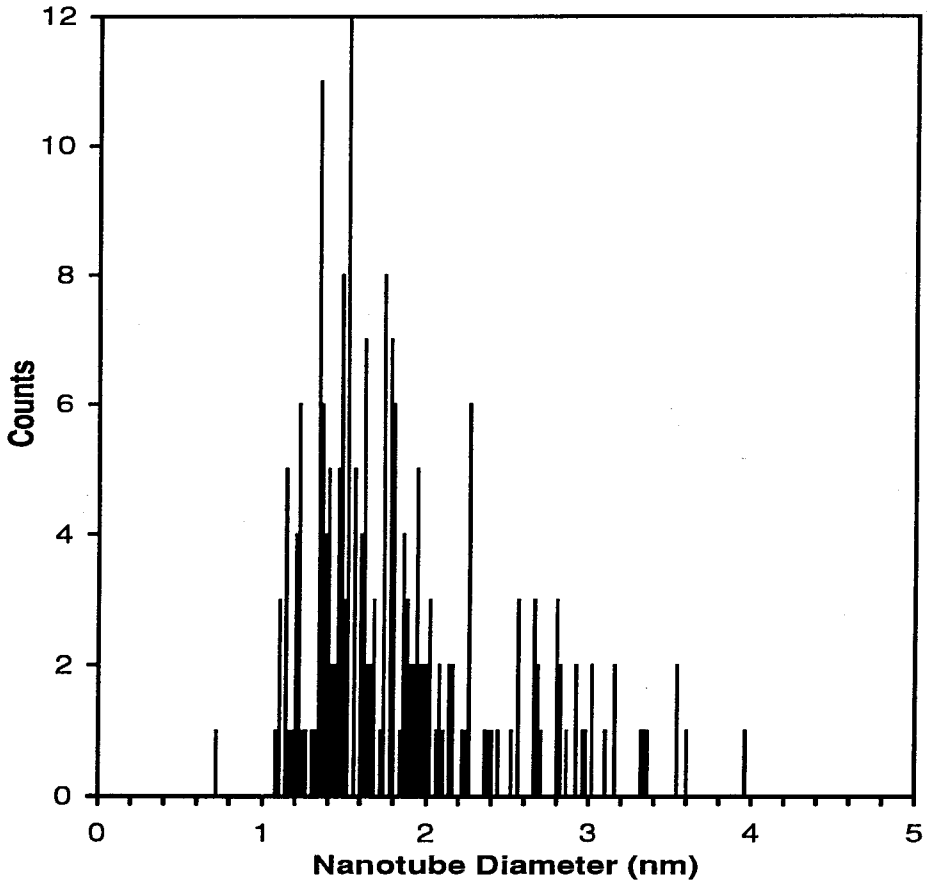

Figure 7.5: Histogram of diameter distribution of nanotubes produced with Co and Pb.

The nanotube diameter distribution shows fine structure with peaks at an approximately 0.15 nm interval. We calculated the nanotube abundance with all different helicities equally weighted and found that the peaks should be approximately 0.06 nm apart. The variation of the tube abundance, therefore, must be influenced by the tube growth kinetics. We note that adding four carbons to the tube belt increases the diameter by approximately 0.15 nm, with a carbon bond length of 1.42 Å. Earlier carbon cluster studies have shown that C_n, with $n = 14$, 18, and 22 are the predominate neutral products from the photodissociation of lager carbon cluster ions [38] such as C_{36}^+ [39] and C_{46}^+ [40]. The preferential loss of C_{14}, C_{18}, and C_{22} has been explained by noting that these products are monocyclic rings [40]. Aromatic stabilization of neutral polyyne rings C_n suggests that rings with $n = 4m + 2$ (where m is an integer) are more stable than are the neighboring species. Hence the predominance of tube diameters with an increment of four is correlated with the abundance of stable monocyclic ring sizes.

The lack of additional layers on the catalytically-produced nanotubes also supports the assumption that the nanotubes grow from a gas phase carbon species. We have imaged over 2000 tubes and found only one example of a double-layered tube. This result is in contrast to the case of nanotubes formed on the cathode, where single-layer tubules have not even been observed. Multilayer tubes are formed on the cathode, which provides a surface for the nucleation of multiple layers [9, 10, 32]. Catalytic growth in the gas phase, without a surface, does not provide a mechanism for the formation of multiple layers. The carbon rings present in the plasma are the nucleated starting material. The catalyst simply provides for the efficient addition of carbon to this species. The promoters assist the catalyst by preventing the blockage of reactive sites that otherwise would arrest the tube growth.

That the tubes grow from a precursor common to fullerenes also explains why the small diameter nanotubes, rarely formed on the cathode, are the major product for

cobalt catalyzed nanotubes. The growth of fullerenes from carbon rings starts with small monocyclic rings that coalescence to form polycyclic rings and subsequently convert to either monocyclic rings or fullerenes [35, 36]. Thus, there are two competing channels for polycyclic ring conversion. Hunter *et al.* have illustrated that the polycyclic rings converts to monocyclic rings for $n < 40$, and to fullerenes for $n > 40$ [36]. The predominance of C_{60} in the mass spectrum is the result of efficient conversion to fullerenes. The authors also comment that the lager monocyclic rings C_n (n >100) are less stable with increasing n. They have not been observed because the channel for conversion to fullerenes competes favorably, and the rings are too energetically unstable to survive at a high temperature. This may be the reason why large diameter nanotubes were not observed when using Co alone as the catalyst.

The growth of a Co-catalyzing single-layer nanotubes is depicted in Fig. 7.6. Figure 7.6a displays a monocyclic carbon ring and a Co_mC_n species as the starting materials of nanotubes. In a high temperature environment such as in the arc plasma, the geometry of monocyclic ring may deviate from its planar form, resulting in local *cis* or *trans* carbon deformations, as illustrated in Fig. 7.6b. The *cis* form provides a building block for adding C_2, carried by the cobalt carbide cluster, to the growing site. The nanotubes thus formed should have zero helicity with the armchair structure, as shown in Fig. 7.6c. This is consistent with our result that the few tubes with zero helicity all have the armchair structure. Helical structures can be produced when, after the first benzene ring is built, the *trans* form adjacent to the benzene edge furnishes a proper geometry for C_2 addition, as shown in Fig. 7.6d.

7.5 Discussion

Special care is required to interpret data obtained from an arc, since some variables that control the characteristics of the arc plasma may also affect the growth of carbon

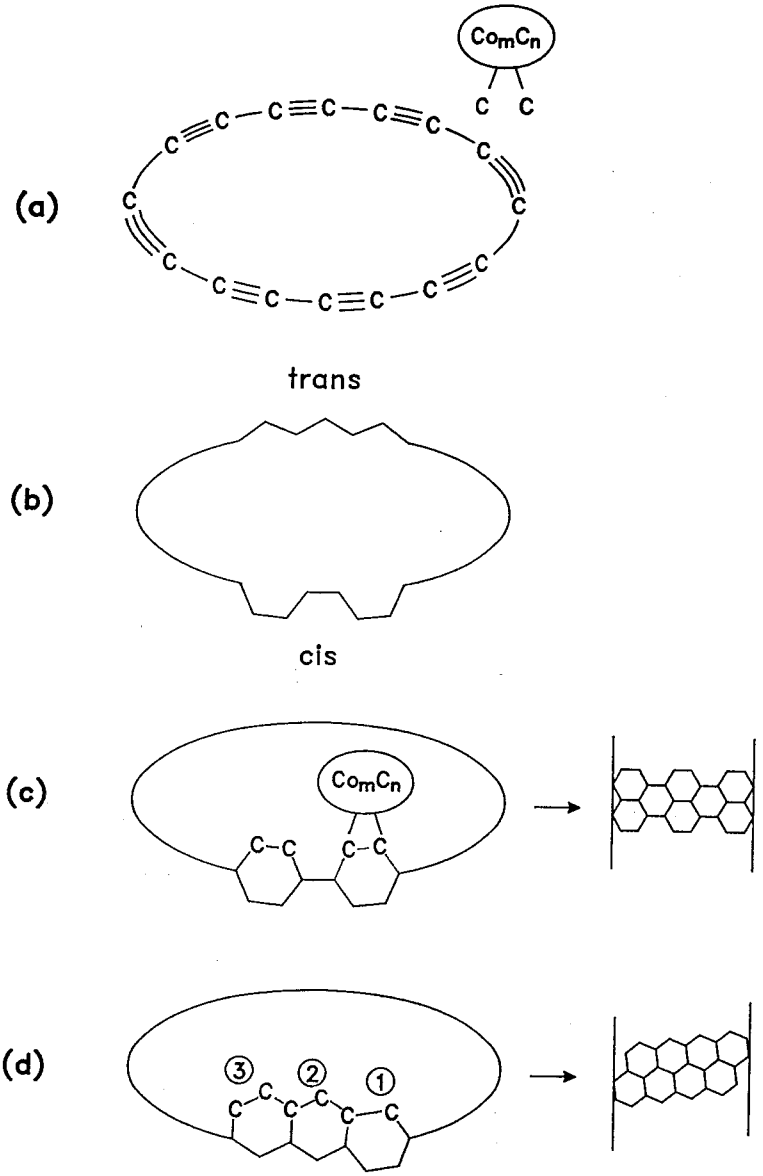

Figure 7.6: Diagrams illustrating nanotube growth mechanism. (a) A monocyclic ring as the nanotube precursor and a cobalt carbide cluster as the catalyst. The cobalt carbide cluster composition and structure is undetermined, but it should carry two carbon bonds that supply C_2 for tube growth. (b) Deformation of monocyclic ring from its planar geometry, resulting in local *cis* and *trans* forms. (c) Formation of a non-helical tubules of armchair structure. (d) Formation of helical tubules. Growth continues on a six-member ring site results in tubules of various helical structures.

nanotubes and nanoparticles. For example, the temperature profile in the reaction chamber, which should be a key parameter to the growth process, is affected by the electric current and buffer gas pressure. The voltage across the electrodes determines the kinetic energy of the electrons, which affects the composition and density distributions of both ionic and neutral cluster species [10]. The amounts of catalyst and promoter are also important in the growth chemistry. Analysis of the results of Chapters 5 and 6, therefore, provides clues to the formation mechanism rather than a direct evaluation of the effects of each reaction variable.

The temperature gradient across the arc plasma is vital to the rapid lengthening of the nanotubes. Nucleation of the nanotube precursors occurs at an elevated temperature, where isomerization between carbon rings and fullerenes occurs rapidly. The formation of the carbon networks crucial for the growth of the nanotubes, however, is exothermic, and a method of heat dissipation is required. That a He buffer gas can effectively quench the excess heat and that higher pressures favors the nanotube growth are, therefore, consistent with our model. Nanotube formation from methane, on the other hand, is endothermic. This may be the reason why nanotube formation is efficient at low pressures when CH_4 and Ar was used as buffer gas.

The formation of large diameter tubes suggests that these promoters initiate the growth at the nucleation stage. When large monocyclic rings are stabilized or start building tubular structure rapidly with the help of promoters, successive growth into long tubes is expected. The same promoting effect will also stabilize the intermediate species during the tube growth, which results in a higher yield of final product. A definite answer to the role of promoters, however, awaits for a better understanding of the catalytic process.

7.6 Conclusions

In summary, we proposed in this chapter a growth model of the single-layer carbon nanotubes grown by Co catalyst, and provided supporting experimental results. This model postulated that a carbon nanotube is built from a carbon ring, with small catalytic clusters rapidly knitting the carbon network to form a tubule. Planar carbon ring isomers, which are known to exist in laser generated carbon plasmas, were regarded as the precursors to the nanotubes. The catalyst promoters played a role in enhancing the nucleation process as well as in stabilizing the intermediates required for nanotube growth.

This model explained several experimental observations that are unique to the nanotubes grown with the Co catalyst in the arc. The single-layered feature was explained by the origination of the nanotubes from carbon ring precursors. Inclusion of materials in the tubes was explained by growth with an open end. Structured diameter distributions arose from the characteristics of the nucleation process. Large diameter nanotubes that form abundantly with catalyst promoters were explained by the stabilization of the large ring precursors.

Several aspects of this growth model could be tested experimentally. For example, if carbon vapor and cobalt or cobalt carbide clusters with narrow range of mass distribution could be controlled independently, one can vary the concentration of the proposed active catalytic species and observe the results. Annealing studies of the carbon ring isomer structures in the presence of catalyst promoters would verify the stabilization of monocyclic rings by these elements. With more information on the nanotube and carbon ring formation, the growth model may be further refined and future experiments may be proposed.

References

[1] S. Iijima, Nature **354**, 56 (1991).

[2] T. W. Ebbesen, Annu. Rev. Mater. Sci. **24**, 235 (1994).

[3] D. S. Bethune, C.-H. Kiang, M. S. de Vries, G. Gorman, R. Savoy, J. Vazquez and R. Beyers, Nature **363**, 605 (1993).

[4] C.-H. Kiang, W. A. Goddard III, R. Beyers, J. R. Salem, and D. S. Bethune, J. Phys. Chem. **98**, 6612 (1994).

[5] C.-H. Kiang, P. H. M. van Loosdrecht, R. Beyers, J. R. Salem, D. S. Bethune, W. A. Goddard III, H. C. Dorn, P. Burbank, and S. Stevenson, to appear in *Proceedings of the Seventh International Symposium on Small Particles and Inorganic Clusters*, (Kobe,Japan,1994), Surf. Rev. Lett.

[6] M. Endo, Chemtech **18**, 568 (1988).

[7] G. G. Tibbetts, Carbon **27**, 745 (1989).

[8] R. T. K. Baker, Carbon **27**, 315 (1989).

[9] S. Iijima, P. M. Ajayan, and T. Ichihashi, Phys. Rev. Lett. **69**, 3100 (1992).

[10] D. T. Colbert, J. Zhang, S. M. McClure, P. Nikolaev, Z. Chen, J. H. Hafner, D. W. Owens, P. G. Kotula, C. B. Carter, J. H. Weaver, A. G. Rinzler, and R. E. Smalley, Science **266**, 1218 (1994).

[11] R. T. K. Baker and P. S. Harris, "The Formation of Filamentous Carbon," in *Chemistry and Physics of Carbon*, **14**, edited by P. L. Walker, Jr. and A. Thrower, (Marcel Dekker, New York,1978), pp.83–165.

[12] S. Seraphin and D. Zhou, Appl. Phys. Lett. **64**, 2087 (1994).

[13] P. Schnabel, M. P. Irion, and K. G. Weil, J. Phys. Chem. **95**, 9688 (1991).

[14] S. Iijima and T. Ichihashi, Nature **363**, 603 (1993).

[15] Y. H. Pan, K. Sohlberg, and D. P. Ridge, J. Am. Chem. Soc. **113**, 2406 (1991).

[16] S. Seraphin, in *Recent Advances in the Chemistry and Physics of Fullerenes and Related Materials*, edited by K. M. Kadish and R. S. Ruoff (The Electrochemical Society, Pennington, NJ, 1994).

[17] P. M. Ajayan, J. M. Lambert, P. Bernier, L. Barbedette, C. Colliex, and J. M. Planeix, Chem. Phys. Lett. **215**, 509 (1993).

[18] Y. Saito, T. Yoshikawa, M. Okuda, N. Fujimoto, K. Sumiyama, K. Suzuki, A. Kasuya, and Y. Nishina, J. Phys. Chem. Solids **54**, 1849 (1993).

[19] J. M. Lambert, P. M. Ajayan, P. Bernier, J. M. Planeix, V. Brotons, B. Cog, and J. Castaing, Chem. Phys. Lett. **226**, 364 (1994).

[20] X. Lin, X. K. Wang, V. P. Dravid, R. P. H. Chang, and J. B. Ketterson, Appl. Phys. Lett. **64**, 181 (1994).

[21] M. Endo, K. Takeuchi, S. Igarashi, K. Kobori, M. Shiraishi, and H. W. Kroto, J. Phys. Chem. Solids **54**, 1841 (1993).

[22] D. H. Robertson, D. W. Brenner, and J. W. Mintmire, Phys. Rev. B **45**, 12592 (1992).

[23] A. A. Lucas, Ph. Lambin, and R. E. Smalley, J. Phys. Chem. Solids **54**, 587 (1993).

[24] G. Meijer and D. S. Bethune, J. Chem. Phys. **93**, 7800 (1990).

[25] R. D. Johnson, C. S. Yannoni, J. R. Salem, and D. S. Bethune, in *Clusters and Cluster-Assembled Materials*, MRS Proc. **26**, edited by R. S. Averbach, J. Bernholc and D. L. Nelson (Materials Research Society, Pittsburgh, PA, 1991), 715.

[26] T. W. Ebbesen, J. Tabuchi, and K. Tanagaki, Chem. Phys. Lett. **191**, 336 (1992).

[27] M. Endo and H. W. Kroto, J. Phys. Chem. **96**, 6941 (1992).

[28] R. Saito, G. Dresselhaus, and M. S. Dresselhaus, Chem. Phys. Lett. **195**, 537 (1992).

[29] R. Saito, M. Fujita, G. Dresselhaus, and M. S. Dresselhaus, Matls. Sci. and Eng. B **19**, 185 (1993).

[30] S. Subramoney, R. S. Ruoff, D. C. Lorents, and R. Malhotra, Nature **366**, 637 (1994).

[31] Y. Saito, M. Okuda, N. Fujimoto, T. Yoshikawa, M. Tomita, and T. Hayashi, Jpn. J. Appl. Phys. 2 Lett. (Japan) **33**, L526 (1994).

[32] A. Maiti, C. J. Brabec, C. M. Roland, and J. Bernholc, Phys. Rev. Lett. **73**, 2468 (1994).

[33] C.-H. Kiang, W. A. Goddard III, R. Beyers, J. R. Salem, and D. S. Bethune, to appear in *Science and Technology of Fullerene Materials*, MRS Proc., edited by P. Bernier, T. W. Ebbesen, D. S. Bethune, R. M. Metzger, L. Y. Chiang, and J. W. Mintmire, (Materials Research Society, Pittsburgh, 1994).

[34] J. Hunter, J. Fye, and M. F. Jarrold, Science **260**, 784 (1993).

[35] G. von Helden, N. G. Gotts, and M. T. Bowers, Nature **363**, 60 (1993).

[36] J. M. Hunter, J. L. Fye, E. J. Roskamp, and M. F. Jarrold, J. Phys. Chem. **98**, 1810 (1994).

[37] G. von Helden, P. R. Kemper, N. G. Gotts, and M. T. Bowers, Science **363**, 1300 (1993).

[38] P. P. Radi, T. L. Bunn, P. R. Kemper, M. E. Molchan, and M. T. Bowers, J. Chem. Phys. **88**, 2809 (1988).

[39] S. C. O'Brien, J. R. Heath, R. F. Curl, and R. E. Smalley, J. Chem. Phys. **88**, 220 (1988).

[40] J. M. Hunter, J. L. Fye, and M. F. Jarrold, J. Chem. Phys. **99** 1785 (1993).

Chapter 8

Summary

This thesis covered a wide range of topics, from simulation and theory to experimental synthesis and characterization.

We successfully produced a pairwise potential for AgBr, and the predicted properties agreed fairly well with experimental values. We showed that Br^- polarizability and van der Waals interactions are important in the AgBr crystal field. The shell model provided a useful tool for examining the effects of polarization on the crystal properties, especially the phonon dispersion frequencies and dielectric constants. This potential can now be used to calculate defect properties.

We have provided a formalism for simulating motions with disparate time scales, with a focus on the simulation of polarization effects in molecules and solids. The shell model has often been incorporated into molecular force fields, and it has proven to be essential for proper treatment of many systems. Inclusion of the shell model in molecular dynamics simulations has long been thought intractable because of the complications introduced by the fast shell motion. Using statistical mechanical theory, we obtained analytic effective Hamiltonians for the motion of the ion cores for both a quantum and classical description of the shells. This result extends the shell

model into a formalism useful for molecular dynamics simulations. As an example, fluctuations of the shell positions were shown to account for the London dispersion interaction.

These methods should also be useful for including the effects of light particles on the motions of heavier atoms, when the heavy atoms are treated with classical molecular dynamics. This statistical approach, together with the suggested numerical techniques, provides a rigorous means to efficiently incorporate such rapid dynamical position fluctuations.

We described the synthesis, purification, and characterization of several endohedral metallofullerenes. This work followed recent advances in metallofullerene production and purification techniques. We described the first structural determination of a metallofullerene: we made Sc_2C_{84} crystals and determined their structure with electron diffraction and high-resolution imaging. Sc_2C_{84} metallofullerenes were found to form an orientationally disordered *hcp* structure with the scandium atoms inside the carbon cages. Purified Er metallofullerene samples were prepared for further structural and optical spectroscopic investigations. These materials, due to their interesting optical transitions, may prove useful in a variety of laser and optical devices.

We provided a description of the experiment by which we discovered single-layer carbon nanotubes simultaneously with Iijima in 1993. We detailed systematic experiments that varied experimental conditions, such as the chemical character and percentage of Co in the rod, the buffer gas pressure, composition, and flow rate. We also found that sulfur, bismuth, and lead promote nanotube production and extend the diameter distribution of single-layer carbon nanotubes out to 6 nm. We have studied these structures primarily with transmission electron microscopy. Additional studies were carried out with X-ray diffraction and energy dispersive spectroscopy. Detailed atomic structure of the single-layer nanotubes were obtained, despite the extremely weak electron diffraction intensity.

Nanotube structural transformations induced by electron beam heating were also discussed. Nanotubes could be either destroyed or repaired, depending on the conditions. The bundling of nanotubes was observed in real time. The time scale of the transformations was seconds, very long for usual molecular motions.

Diverse structures such as nanocompartments, multilayer nanotubes, and nanofibers were produced catalytically. They were found in the rubbery deposit around the cathode when both cobalt and sulfur were vaporized together with carbon. Filling of the nanotubes and nanocompartments with metals or metal compounds was also achieved when sulfur was incorporated as the source material. Metal crystal encapsulated graphitic polyhedra formed abundantly when sulfur, bismuth, or tungsten were present.

We proposed a growth model of the single-layer carbon nanotubes grown by Co catalyst, and provided supporting experimental results. The carbon nanotube was thought to build from a carbon ring, with small catalytic clusters rapidly constructing the honeycomb carbon network to form a tubule in the gas phase. Monocyclic carbon ring isomers were the precursors of the nanotubes. The catalyst promoters played a role in enhancing the nucleation process as well as in stabilizing the intermediates required for nanotube growth. This model explained several experimental observations that are unique to the nanotubes grown with the Co catalyst in the arc.

Experimental research on single-layer nanotubes is still in a very early stage. The discovery of catalyst promoters provides a key to mass production of single-layer carbon nanotubes and metal encapsulated graphitic polyhedra. Nanotube properties and applications that depend on the diameter, such as electric conductivity, hydrogen storage media, and super strong materials may now be investigated. Catalytic production allows high efficiency and selectivity. Additional study of nanomaterials formed with various catalysts and promoters will help elucidate the growth dynamics. Such studies may provide fundamental information that will further aid the develop-

ment of potential applications.

Proving our detailed growth mechanism for nanotubes remains a challenge. The next step to the work presented here is to identify experimentally the active catalyst species. This will require developing well controlled experimental systems to study the reactions. Such control is necessary to allow the various experimental parameters to be investigated systematically.

Ab initio calculations suggest that these nanotubes could be one-dimensional electric conductors or semiconductors depending on their diameter and helicity. Other applications of carbon nanotubes have been proposed in areas which range widely from physics and chemistry to materials and biology. Examples include hydrogen storage media, nanowire templates, scanning tunneling microscope tips, catalyst supports, seeds for growing carbon fibers, batteries materials, and reinforcing fillings in concrete. Such applications provide ample motivation for further research on this pseudo-one-dimensional form of carbon.

The self-assembly of carbon and metal in the vapor phase has produced diverse nanomaterials such as nanotubes, metal encapsulated graphitic polyhedra, and metallofullerenes. Many of these novel structures are stable and can be produced in macroscopic quantity, suggesting that they may be useful as building blocks for constructing advanced materials. Interests in exploring uncommon properties and potential applications will continue to inspire research on these novel materials.